Large Eddy Simulations of Spark Ignition Processes with the CMC method

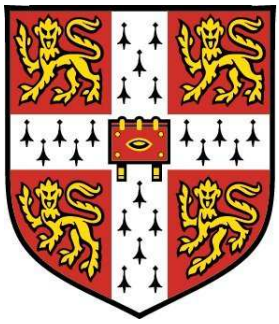

University of Cambridge

Department of Engineering

This dissertation is submitted for the degree of

Doctor of Philosophy

by:

Antonios Triantafyllidis

St Edmund's College

Thursday, 28^{th} of May, 2009

Declaration

This dissertation is the result of my own work and includes nothing which is the outcome of work done in collaboration except where specifically indicated in the text. The dissertation contains approximately **35,000** words, **93** figures and **eight** tables.

Antonios Triantafyllidis

Hopkinson Laboratory, Cambridge
Thursday, 28^{th} of May, 2009

Acknowledgements

The work presented in this thesis would not have been carried out without the help of many people, to whom I am profoundly grateful. First and foremost I would like to thank my supervisor, Dr E. Mastorakos, for his support and guidance, both on an academic and on a personal level. I thank him for pointing out the positives when there were none to see and for not permitting my natural pessimism to overwhelm me. I thank Dr N. Swaminathan for some really interesting discussions, but also for allowing me to make use of the computer cluster 'hercules'. For their technical input I thank R. Eggels (Rolls-Royce Deutschland) and S. Ahmed (Cambridge). I must thank P. Benie (Cambridge) without whose computing expertise, little of the work presented here would have been completed. Funding from Rolls-Royce plc, the Department of Engineering, EPSRC and the EU enabled me to complete this work without financial worry. I thank the Consortium On Computational Combustion For Engineering Applications (COCCFEA) for enabling me to use the facilities of HECToR, the UK's national high-performance computing service, which is provided by UoE HPCx Ltd at the University of Edinburgh, Cray Inc and NAG Ltd, and funded by the Office of Science and Technology through EPSRC's High End Computing Programme.

I am fortunate to have joined Dr Mastorakos's group and to have received help from its members. In particular, I thank E. S. Richardson, G. de Paola, C-W Lee, M. de la Cruz-Garcia and A. Neophytou. I have made good friends in the lab, A. Garmory, S. Bennett, A. Pastore, and I thank them for putting up with my

continuous moaning about the air-conditioning system that never seemed to work and the high levels of noise at the office. Special thanks to all the people who have now left the lab, but helped me while they were here, each in their own way, R. Kavanagh, R. C. Payne, P. Kumar and T. Marchione. I must thank my college friends, P. Tomlin and M. Zwart, for taking my mind off things with discussions about nothing in particular. I would like to thank S. Daultrey for reminding me what is important in life.

Last, but certainly not least, I would like to thank my parents and my brother for their support during these years and for always believing that I haven't been wasting my time.

Publications

Work from this thesis has been accepted for publication in the following articles:

1. Large eddy simulations of forced ignition of a non-premixed bluff-body methane flame with conditional moment closure [1].

2. Implementation issues of the conditional moment closure in large eddy simulations [2].

and in the following conference:

3. LES/CMC of forced ignition of a bluff-body stabilised non-premixed methane flame [3].

Other works related to the author include:

4. Analysis of non-premixed auto-ignition of heated hydrogen/air mixtures with different detailed mechanisms [4].

5. Simulations of hydrogen auto-ignition in a turbulent co-flow of heated air with LES and CMC approach [5].

6. Experiments and large-eddy simulations of acoustically-forced bluff-body flows [6].

In the conference presentations 4 and 5, the software package developed in the lab is being used by other laboratories with the author's assistance.

Abstract

This thesis describes the application of first-order Conditional Moment Closure (CMC) in Large Eddy Simulations (LES) of forced ignition in turbulent flows.

The first part of this thesis describes the numerical implementation of the CMC method in LES and investigates a number of implementation issues which arise due to the need to use meshes of different resolution to solve the LES and CMC equations. This is because of the high dimensionality of the CMC equations and the stiffness of the resulting system of differential equations which results in high computational cost. It was found that, in general, during the exchange of information from one mesh to the other, the modelling and volume-averaging procedures are inter-changeable in the order in which they can be performed. The models for the scalar dissipation rate and filtered density function are also validated against experimental data.

The second part of the thesis focuses on the application of the LES/CMC approach in forced ignition problems in laboratory-scale burners. Two burners of different complexity are investigated and different parameters related to the spark, the flow and the numerical setup are examined. The first burner involves a planar shearless mixing layer between fuel and air. A TVD scheme was considered for the discretisation of the convection term in the CMC equation and it was found to be less diffusive and hence more accurate than a first-order upwind scheme, but at a high computational cost. It was found that the resolution of the CMC mesh is critical in capturing the correct flame expansion pattern in the spanwise direction (across the flow) and that this expansion is dominated by the resolved velocity fluc-

tuations. Furthermore, although flame expansion is captured, propagation against the flow or flame extinction is not, which may be related to the first-order closure assumption. The second configuration examined was a bluff-body stabilised flame. The location and size of the spark determine the flame expansion pattern and success of the spark event. Comparison between two chemical mechanisms of different complexity (single-step and detailed) reveals that the correct trends could be captured by the single-step mechanism, but the expansion rate of the flame is predicted more accurately when the detailed mechanism is used.

This thesis is essentially a feasibility and sensitivity analysis of the CMC method in LES of forced ignition and is hopefully a step towards the predictive simulation of ignition in aviation gas turbines.

Contents

List of Figures

List of Tables

Chapter 1

Introduction

1.1 Motivation

Combustion of fossil fuels propelled the industrial revolution in the late 18th and early 19th century and has since been an integral part of industrial growth. The transformation of the chemical energy stored in fossil fuels to heat and subsequently mechanical or electrical energy is done in most cases through a flame. A flame can be initiated either by forced or auto- ignition. It is therefore of fundamental interest to investigate closely the processes during ignition and flame expansion. Ignition (both forced and auto-) is interesting also for practical engineering applications. Spark ignition engines and relight of an aviation jet engine are examples of forced ignition, while diesel engines and the scram-jet are examples of auto-ignition [13]. In most cases the ignited flow is turbulent. There is, therefore, the need to understand and possibly be able to predict ignition in turbulent flows.

This thesis investigates the feasibility of using a model that describes mathematically the processes involved in turbulent combustion in forced ignition problems. The mathematical model is applied in geometries of different complexity and it is tested in the context of revealing which of the characteristics already observed in similar experimental studies can be reproduced. The final goal, towards which

this thesis is hopefully a step, is to have a predictive tool that could be used even in complex gas turbine geometries, to assess the reliability and robustness of the combustor, in terms of ignition success.

1.2 Ignition of turbulent non-premixed flames

Ignition of a flammable mixture can be roughly divided into two categories: forced (or spark-) ignition occurs when an external source of heat (and/or species) induces the transition from an initially unreacting state to a fully burning state, while auto-ignition occurs when no external source is needed for this transition to take place. The fundamentals of ignition are reviewed in chapter 7 of Ref. [14], while a recent review of ignition can be found in Ref. [13]. This thesis focuses on forced ignition, and more specifically in non-premixed gaseous configurations.

There are many different ways to initiate combustion of a flammable gaseous mixture; the most common is an electric spark, but also laser [15], plasma jet [16] and ignition by a jet flame have also been suggested [17]. The way the spark has been created may be considered to be irrelevant for the subsequent flame expansion and stabilisation. What is of major importance for practical applications is the notion of a minimum ignition energy [14] for initiating a self-sustaining front. If the deposited energy is too low, then the flame kernel will decay rapidly due to the high diffusion rates of heat and radicals, compared to their production rates [13].

Ignition simulations of laminar non-premixed counterflow methane flames using detailed chemistry [18] have shown that the location of the spark and the local strain rate determine the success or failure of a spark event. A spark can fail even if placed around stoichiometric, due to the high strain rate at that location.

The introduction of turbulence in a flow adds to the complexity of the problem. In addition to what has been mentioned about laminar flame ignition, the higher strain rates associated with turbulent flows necessitate extra spark energy and a degree of stochasticity is expected due to the fluctuations of the velocity and the

strain rate [13]. Spark ignition experiments of turbulent jets using different fuels [19–21] revealed that the region where the probability of finding a kernel is greater than zero after the spark extends further than the lean and rich flammability limits, implying that the fluctuations of the mixture fraction play an important role in the kernel creation. Along the centreline, the probability to find a kernel was found to be almost equal to the probability of finding flammable mixture (flammability factor). Furthermore, the probability of having ignition (creation of kernel and successful flame propagation) is different from the probability of finding a kernel. It has also been observed experimentally that the ignition probability decreases with increasing jet velocity, because the flame would have to propagate 'against' a higher velocity [22]. Experiments in a counterflow configuration [23] have shown that ignition probability decreases with increasing bulk velocity due to the increase of the strain rate. An experimental study of a bluff-body methane flame [11] revealed clearly three modes of failed ignition: failure to create a kernel, creation of a kernel that is convected away and a more complicated but rarer mode where the flame grew, filling a significant part of the combustor, but not achieving overall stabilisation.

Few simulations of forced ignition of turbulent flames have been performed so far. The upstream propagation of jet flames and their lift-off height have been studied and reproduced well [24, 25]. Models from premixed combustion have been modified to be used in ignition problems (a review can be found in Ref. [13]). Recently there has been an effort to model ignition of a bluff-body stabilised flame [26], while a very impressive simulation of ignition sequence of a gas turbine combustor has also been performed [27]. These simulations give hope that further developments of the current combustion models may lead to good predictions of ignition. However, many ingredients of these models and their detailed behaviour remain untested. The present thesis discusses in depth one such model and offers some detailed validation against experimental data.

1.3 Large Eddy Simulations

1.3.1 General

Large Eddy Simulations (LES) are based on the energy-cascade hypothesis, according to which turbulence can be considered to be composed of eddies of different sizes and therefore different characteristic velocities and timescales. The larger of these eddies are unstable and break up, transferring their energy to smaller eddies [28]. This process, which is called energy cascade, continues until the eddies are small enough so that their kinetic energy can be dissipated by molecular viscosity.

In LES, the larger, three dimensional scales are directly resolved, while the effect of the smaller scales is modelled [28]. This is done by applying a spatial filtering operation to the instantaneous flow field, thus removing the motions of lengthscales smaller than the filter size Δ [29]. The effect of those scales needs then to be modelled. The fact that the smaller scales tend to be more homogeneous and universal implies that simpler models will be able to be used with relative success [30]. Despite all the advantages of LES, the fact that combustion takes place mostly on a sub-grid scale level underlines the need for a turbulent combustion model. Turbulence enhances mixing, but only molecular diffusion forms a mixture that enables chemical reactions to occur [29]. More information on LES can be found in textbooks [28, 31] and review papers [29, 30, 32].

1.3.2 Combustion LES

In non-premixed combustion, which is the focus of this thesis, fuel and oxidiser enter separately the combustion chamber where they mix and burn during continuous interdiffusion [33]. Using the so-called coupling functions, the rate of mixing of fuel and oxidiser can be described by a conserved scalar, the mixture fraction ξ [34]. It takes the value of unity in the fuel stream and zero in the oxidiser stream. The mixture fraction may be physically interpreted as the mass fraction of material that

originated in the fuel stream. The introduction of ξ leads to the conserved scalar methods that form the basis for most of the models used in non-premixed turbulent combustion. In the conserved scalar method, the species mass fractions and temperature (or enthalpy) are considered to be functions of the mixture fraction only. The aim of the different models is to calculate these functions. Most of the models were developed for and used in RANS (Reynolds Averaged Navier-Stokes) calculations and were then modified or further developed to be applicable in LES. Mixture fraction based approaches and the transported Probability Density Function, PDF, (or filtered density function, FDF, in an LES context) method are discussed below.

1.3.2.1 Chemical equilibrium

To calculate the functions mentioned above, the assumption of chemical equilibrium can be made. In the context of this assumption, the chemical reactions are infinitely fast, but reversible and therefore all the species are in equilibrium at each value of the mixture fraction [35]. This model has been used in LES of a hydrogen jet diffusion flame burning in a co-flowing stream of air [36]. The simplicity of the configuration, the low turbulence levels in the jet and the co-flow, as well as the choice of fuel (the authors note that the assumption of chemical equilibrium for hydrogen/air combustion provides acceptable state relationships between ξ and the thermo-chemical variables) resulted in reasonably good predictions of the temperature and species.

1.3.2.2 Laminar flamelets

Chemical equilibrium does not take into account effects of finite-rate chemistry and this motivates the development of more complicated models. In flamelet models [37], the basic assumption is that the chemical timescales are short enough so that reactions occur in a thin layer around stoichiometric mixture fraction on a scale smaller than the small scales of turbulence and thus the structure of the reaction zone remains laminar [29]. The species and temperature transport equations can

then be transformed to a system where the mixture fraction appears as an independent variable (flamelet equations). In the limit of the steady laminar flamelet, the chemical source term and the mixing term (where the scalar dissipation rate appears) are in balance. The solution is then only a function of the scalar dissipation rate and the boundary conditions and can be pre-computed and tabulated [38]. This model has been applied to LES of a turbulent hydrogen jet flame, close to the blow-off limit where a significant amount of non-equilibrium chemistry takes place [39]. The predictions were found to agree well with the experimental data, as well as with RANS simulations using a more complicated turbulent combustion model (the PDF model). It has also been applied to a bluff-body stabilised flame [40], where it was found that inaccuracies in the predictions of scalars were related to inaccuracies in the predictions of the mixture fraction.

An extension of the steady laminar flamelet model is the unsteady flamelet model. The introduction of time dependence makes the use of pre-computed tables impossible and transport equations must be solved for the flamelets. This method has been applied to LES of a piloted methane diffusion flame (Sandia flame D), which has a partially premixed fuel stream [41]. The agreement with the experimental data was found to be good, even for CO and NO. Some discrepancies between the LES predictions and the experimental data were found, especially in the rich branch of the flame, which may be attributed to the inability to account for experimental data points corresponding to an extinguished flame [41].

1.3.2.3 Progress variable approach

The progress variable approach is similar to the steady flamelet approach, especially in its implementation. In this approach, the profiles of the species and temperatures are pre-computed and tabulated in terms of the mixture fraction and a progress variable [42]. The progress variable must be a non-conserved scalar and is usually assumed to be independent of the mixture fraction. The problem that arises in this

approach is the evaluation of the FDF of the progress variable, which needs to be further researched [42]. This method has been applied to LES of a co-axial methane jet combustor [42]. The agreement with the experimental data was good, especially compared with that of a fast chemistry model and a steady flamelet model. A similar approach was used in LES of Sandia Flames D and E [43]. The agreement of the mean quantities was good, with some inaccuracies in the rich branch of the flame.

1.3.2.4 Conditional Moment Closure

In the Conditional Moment Closure (CMC), transport equations are solved for the conditional averages of the reacting scalars, the conditioning being on the mixture fraction. The equations and the implementation in LES are discussed in chapter 2. The CMC was developed independently by Klimenko and Bilger and a comprehensive review can be found in Ref. [44]. It has also been recently formulated for LES, where it was found that the CMC equation has the same form as in RANS [45]. The unconditional averages of the reacting scalars can be found by integrating the conditional averages over the filtered density function (FDF) (or PDF in a RANS context) of the mixture fraction. By nature, the CMC approach includes unsteady effects, which makes it an ideal candidate for the study of transient problems, such as ignition. The explicit presence of the scalar dissipation rate (see section 2.3.2) enables it to capture the effects of small scale mixing [13], while the fact that convection and turbulent diffusion terms appear in the CMC equation (see section 2.3.2, eq. (2.28)) suggests that the physical processes involved in the flame propagation phase are also included.

If the fluctuations of the conditional averages are considered to be small (and therefore neglected), first-order closure can be provided for the chemical source term in terms of conditional averages. The fluctuations of the conditional averages may be taken into account in what can be considered higher order closure, where equations are solved for the variances and co-variances (and in theory even higher

order moments) of the conditional reacting scalars.

CMC for RANS

In a RANS context, first-order CMC has been used in two-dimensional studies of spray auto-ignition [46, 47], but also in three-dimensional simulations of diesel engines [48]. The results were overall good, despite the fact that the conditional fluctuations were neglected. This may be attributed to the relatively low scalar conditional dissipation rate, compared to the extinction value, making the effect of the conditional fluctuations minor [13].

First-order CMC has also been applied to studies of Sandia Flame D (piloted methane flame) [49], where discrepancies in the predictions of species (especially on the rich side) were attributed to the chemical mechanism (it involved 19 species and 36 reactions) or to the first-order closure assumption. A study of a hydrogen jet flame [50] revealed that good predictions were produced using three different mechanisms and that the discrepancies may be attributed to the cross-stream averaging process. A comprehensive assessment of the ability of first-order CMC to predict a range of turbulent flames (Sandia flames A to F) [51] showed reliable predictions for flames that have little or no extinction, with the exception of NO levels, while when local extinction is present, the predictions deteriorate. The introduction of second-order CMC [52] improved the predictions, especially for the minor species. Simulations of a lifted hydrogen jet flame [53, 54] have shown good agreement with experimental data, in terms of lift-off height and it was demonstrated that the correct stabilisation mechanism was reproduced (heat release rate and axial diffusion balance axial convection and scalar dissipation rate).

Recirculating flows have also been investigated with first-order CMC [55], where reasonable agreement with experimental measurements was achieved, with some discrepancies in the concentration of OH, which was attributed to the over-prediction of the scalar dissipation from the CFD solver and discrepancies for CO and H_2, the sources of which are unclear. Furthermore, simulations of a counterflow flame

have also been performed [56]. The agreement with the experimental observations was good and it was found that the flame would extinguish if the bulk velocity was increased, albeit at a value higher than the experiment. Finally, soot formation in methane, propane and ethylene has been investigated with first-order CMC [57, 58] and it was found that reasonable agreement with experimental data was achieved, with some of the discrepancies attributed to the soot model.

CMC for LES

As mentioned before, the CMC equation has recently been formulated for LES [45] and an *a priori* analysis using results from Direct Numerical Simulations (DNS) of reacting mixing layers [59] has shown that first-order closure may be adequate for regions far away from extinction. Near extinction, the conditional fluctuations may be large and should not be neglected. The LES/CMC approach has been used to study Sandia Flame D [45], a bluff-body flame [60] and a lifted flame, sustained by auto-ignition [61]. Overall, the agreement with the experimental data is reasonably good, and indeed improved if compared to RANS/CMC calculations. This may be attributed to the capability of LES to account for temporal and azimuthal variations of the scalar dissipation rate.

So far, the CMC has been mostly applied in an integrated form, where simplifying hypotheses (based on the nature of the studied flame) reduce the dimensionality of the CMC equation, transforming it into a one- [60] or two-dimensional [61] equation in space, or a three-dimensional equation with reduced resolution in two of the directions [45].

The CMC model is very similar to the Eulerian flamelet model (EFM) [62] which has been applied to Sandia Flame D, where good agreement with the experimental data was achieved. The EFM model has also been applied to a bluff-body stabilised flame [63] where good agreement with the experimental measurements was achieved, with some discrepancies in the concentration of NO, CO and OH, which may be partly attributed to the cross averaging that was performed.

1.3.2.5 Transported FDF

The transported joint scalar and joint scalar/velocity PDF method [64] is applicable to all turbulent reacting flows. Its main attraction is the fact that the chemical source term appears in closed form. However, the molecular mixing term is unclosed and requires modelling. The PDF method has been applied to flame simulations using RANS [65–72] with great success. It has been extended to LES using the notion of the Filtered Density Function (FDF) [73]. The transported FDF has been further extended and applied to a mixing layer and a jet simulation [74, 75], where the predictions were compared to DNS results and good agreement was found, albeit at a high computational cost. The method has also been used in LES of a non-premixed turbulent bluff-body stabilised flame [76]. The predictions were found to agree with the experimental data, but they were also found to be sensitive to modelling parameters, related to the molecular mixing term. Recently, this method was applied to auto-ignition problems [77, 78], and it was found that good agreement with the experimental data could be achieved [77] and the complicated regimes observed in the experiment were reproduced [78].

1.3.2.6 Complex geometries

Current facilities of High Performance Computing (HPC) provide enough computational power to demonstrate the capacity of LES in addressing complex industrial configurations [79]. LES of a sector of an annular combustor burning gaseous n-decane [80], of a model can-type combustion chamber [81], of a realistic gas turbine combustor [82], of ignition of a rocket-like configuration [83] and of an ignition sequence in a gas turbine engine [27] demonstrate the capabilities of this method and the challenges, in terms of modelling, computational resources, management of data and post-processing, that need to be dealt with in such large simulations. Nevertheless, they show that this method can be applied to very complex problems and give insight into areas never researched before.

1.4 Objectives

The objective of this work is to investigate the feasibility of using first-order CMC in LES of forced ignition in laboratory-scale combustors. The sensitivity of the predictions to both numerical and modelling parameters is examined and the focus is on determining which of the characteristics already observed in experiments can be reproduced by the simulations.

There have been only a few forced ignition simulations (Ref. [27, 83]) and only in complicated geometries. Detailed validation of the different combustion models for ignition problems has not been done yet. There is hope that the CMC model will be suitable for ignition problems. The fact that it is by nature a transient model and that it includes all the physical processes involved in combustion makes it a good candidate for such problems.

The governing equations for LES and CMC, as well as some implementation issues concerning the coupling of the two methods are discussed in chapter 2, while the numerical methods and chemical mechanisms are presented in chapter 3. Ignition simulations of a turbulent shearless mixing layer are presented in chapter 4 and the sensitivity of the predictions to the CMC mesh resolution, the convection scheme, the flow bulk velocity, as well as the effect of turbulent diffusion in the flame expansion process are examined. In chapter 5, simulations of ignition of a bluff-body stabilised methane flame are discussed, with emphasis being given to the spark parameters (location, size), as well as to the chemical mechanism used. The overall pattern and speed of flame expansion is revealed and the compared in detail with experimental data. Finally, the main conclusions of this thesis are summarised in chapter 6 and recommendations for future work are made.

Chapter 2

Conservation Equations and the Implementation of the Conditional Moment Closure in Large Eddy Simulations

2.1 Introduction

The aim of this chapter is to present the governing equations for LES and CMC, as well as the models used for the unclosed terms. Some of the models are validated by comparison with experimental data. The derivation of the CMC equation is well documented (for example Ref. [44, 45]) and therefore not presented here. The implementation of the CMC method in LES is discussed and special attention is given to the issues that arise in practical LES/CMC applications, where a coarser CMC mesh is used alongside a finer LES mesh. This necessitates the transfer of information regarding the flow field (for example the filtered density function) from a fine mesh to a coarser mesh. Different methods of transferring this kind of information are presented and their accuracy is assessed by analysing detailed measurements of

the mixture fraction in a turbulent plume, in the context of filtering at different resolutions.

2.2 Large Eddy Simulations

The presentation of the governing equations for LES is based on [28, 31] and the reader is encouraged to consult these references for more details.

2.2.1 Filtering

The general filtering process is defined as:

$$\overline{f}(\boldsymbol{x}) = \int f(\boldsymbol{x}) G(\boldsymbol{x} - \boldsymbol{x}')\, d\boldsymbol{x}' \tag{2.1}$$

where $f(\boldsymbol{x})$ is the non-filtered quantity, $\overline{f}(\boldsymbol{x})$ is the filtered (resolved in the context of LES) quantity, $\boldsymbol{x}$ is the spatial coordinate and G is the specified filter that has to satisfy the normalisation condition:

$$\int G(\boldsymbol{x} - \boldsymbol{x}')\, d\boldsymbol{x}' = 1 \tag{2.2}$$

For variable density ρ, a mass weighted (Favre) filtering can be introduced:

$$\overline{\rho}\widetilde{f}(\boldsymbol{x}) = \int \rho f(\boldsymbol{x}') G(\boldsymbol{x} - \boldsymbol{x}')\, d\boldsymbol{x}' \tag{2.3}$$

where $\overline{\rho}$ is the filtered (resolved) density.

Applying the filtering operation to the instantaneous balance equations results in the filtered balance equations, presented in sections 2.2.2 to 2.2.5.

2.2.2 Continuity

The filtered continuity equation is:

$$\frac{\partial \overline{\rho}}{\partial t} + \frac{\partial (\overline{\rho}\widetilde{u}_i)}{\partial x_i} = 0 \tag{2.4}$$

where $\widetilde{u}_i$ is the resolved velocity in the i direction.

2.2.3 Momentum

The filtered momentum equation is:

$$\frac{\partial(\overline{\rho}\widetilde{u}_j)}{\partial t} + \frac{\partial(\overline{\rho}\widetilde{u}_i\widetilde{u}_j)}{\partial x_i} = -\frac{\partial \overline{p}}{\partial x_j} + \frac{\partial \widetilde{\tau}_{ij}}{\partial x_i} - \frac{\partial(\overline{\rho}\tau^r_{ij})}{\partial x_i} \tag{2.5}$$

where $\overline{p}$ is the resolved pressure and $\widetilde{\tau}_{ij}$ is the resolved anisotropic stress tensor:

$$\widetilde{\tau}_{ij} = 2\overline{\mu}\left[\widetilde{S}_{ij} - \frac{\delta_{ij}}{3}\frac{\partial \widetilde{u}_k}{\partial x_k}\right] \tag{2.6}$$

where $\widetilde{S}_{ij}$ is the filtered rate-of-strain tensor:

$$\widetilde{S}_{ij} = \frac{1}{2}\left(\frac{\partial \widetilde{u}_i}{\partial x_j} + \frac{\partial \widetilde{u}_j}{\partial x_i}\right) \tag{2.7}$$

The last term on the right-hand-side (r.h.s) of Eq. 2.5 is the residual stress tensor:

$$\tau^r_{ij} = \widetilde{u_i u_j} - \widetilde{u}_i\widetilde{u}_j \tag{2.8}$$

This term appears in unclosed form and needs to be modelled. The dynamic Smagorinsky model, which can be viewed in two parts, is used here. First, τ^r_{ij} is related to the filtered rate-of-strain tensor through a linear eddy viscosity model:

$$\tau^r_{ij} - \frac{\delta_{ij}}{3}\tau^r_{kk} = -2\nu_t\widetilde{S}_{ij} \tag{2.9}$$

where ν_t is the sub-grid scale viscosity. Next, ν_t is modelled as:

$$\nu_t = (C_S\Delta)^2\,\widetilde{\mathcal{S}} \tag{2.10}$$

where C_S is the Smagorinsky parameter, Δ is the filter width (equal to the size of the LES cell) and $\widetilde{\mathcal{S}}$ is the characteristic filtered rate of strain:

$$\widetilde{\mathcal{S}} = \left(2\widetilde{S}_{ij}\widetilde{S}_{ij}\right)^{1/2} \tag{2.11}$$

The Smagorinsky model implies that the small scales are in equilibrium, so that production and dissipation are in balance. The parameter C_S can either be constant in what is the standard Smagorinsky model, or can be calculated dynamically

(dynamic Smagorinsky model [84]) using a scale similarity approach between the smaller of the resolved and the larger of the sub-grid scales. The latter is used in this work.

Until now, the Smagorinsky model has been the only model used in combustion LES to close the momentum equation. Both the standard [27, 60, 81] and the dynamic model [85] have been used in flame simulations. A comparison of the two models has also been made [36] and it was found that the dynamic model predicted higher levels of fluctuations than the standard model, implying that the latter is too dissipative. Despite the fact than the mean values of C_S using the dynamic model were higher than when using the standard model, the intermittency in the nature of C_S left regions with low dissipation for considerable lengths of time.

2.2.4 Mixture fraction

A transport equation for an additional, conserved scalar (the mixture fraction ξ) is also solved:

$$\frac{\partial(\overline{\rho}\widetilde{\xi})}{\partial t} + \frac{(\overline{\rho}\widetilde{\xi}\widetilde{u}_i)}{\partial x_i} = \frac{\partial}{\partial x_i}\left(\overline{\rho}D\frac{\partial\widetilde{\xi}}{\partial x_i}\right) - \frac{\partial(\overline{\rho}J_i^r)}{\partial x_i} \tag{2.12}$$

where $\widetilde{\xi}$ is the resolved mixture fraction and J_i^r represents scalar transport due to sub-grid scale fluctuations:

$$J_i^r = \widetilde{u_i\xi} - \widetilde{u}_i\widetilde{\xi} \tag{2.13}$$

Fick's diffusion law has been considered and the diffusivity is $D = \nu/\mathrm{Sc}$, where a constant Schmidt number $\mathrm{Sc} = 0.7$ has been considered. The term J_i^r is unclosed. It is modelled similarly to the term τ_{ij}^r in the momentum equation, i.e. by assuming that the sub-grid scale flux is proportional to the resolved gradient:

$$\widetilde{u_i\xi} - \widetilde{u}_i\widetilde{\xi} = -D_t\frac{\partial\widetilde{\xi}}{\partial x_i} \tag{2.14}$$

where $D_t = \nu_t/\mathrm{Sc_t}$ is the turbulent diffusivity, and $\mathrm{Sc_t} = 0.7$ is the turbulent Schmidt number. Different values have been used for $\mathrm{Sc_t}$, ranging from $\mathrm{Sc_t} = 0.4$ in the case of a piloted methane/air diffusion flame [41] to $\mathrm{Sc_t} = 0.7$, used in LES of a turbulent

hydrogen diffusion flame [36], in the case of an opposed-flame methane/air burner [86], as well as in LES of a model gas turbine [81]. It is also possible to use a dynamic procedure, similar to that for C_S for the calculation of $\mathrm{Sc_t}$. However, it has been found that such an approach would have little effect on the predictions of the mixture fraction [36]. Following [36, 81], a constant value of $\mathrm{Sc_t} = 0.7$ has been used throughout this work.

2.2.5 Variance of mixture fraction

Apart from the resolved mixture fraction, it is also important to obtain its sub-grid scale variance $\widetilde{\xi''^2}$. One model that has been used in the past is a gradient type model [87]:

$$\widetilde{\xi''^2} = C_V \Delta^2 \frac{\partial \widetilde{\xi}}{\partial x_i} \frac{\partial \widetilde{\xi}}{\partial x_i} \tag{2.15}$$

where C_V is a coefficient which may have a constant value [88] or may be calculated dynamically using a scale similarity approach [89]. The constant C_V is calculated from experimental data later in this chapter.

In the LES presented in this work, a transport equation for the square of the mixture fraction is solved and then the variance is calculated as

$$\widetilde{\xi''^2} = \widetilde{\xi^2} - \widetilde{\xi}^2 \tag{2.16}$$

The equation for $\widetilde{\xi^2}$ is [90]:

$$\frac{\partial(\overline{\rho}\widetilde{\xi^2})}{\partial t} + \frac{\partial(\overline{\rho}\widetilde{u}_i\widetilde{\xi^2})}{\partial x_i} = \frac{\partial}{\partial x_i}\left(\overline{\rho}(D + D_t)\frac{\partial \widetilde{\xi^2}}{\partial x_i}\right) - 2\overline{\rho}\widetilde{N} \tag{2.17}$$

where $\widetilde{N}$ is the scalar dissipation rate:

$$\widetilde{N} = D\widetilde{\left(\frac{\partial \xi}{\partial x_i}\right)^2} \tag{2.18}$$

A gradient model has been used for the sub-grid scale flux of $\widetilde{\xi^2}$:

$$\widetilde{u_i\xi^2} - \widetilde{u}_i\widetilde{\xi^2} = -D_t \frac{\partial \widetilde{\xi^2}}{\partial x_i} \tag{2.19}$$

For completeness, the filtered transport equation for $\widetilde{\xi''^2}$ is also presented (the derivation can be found in Appendix C):

$$\frac{\partial(\overline{\rho}\widetilde{\xi''^2})}{\partial t}+\frac{\partial(\overline{\rho}\widetilde{u}_i\widetilde{\xi''^2})}{\partial x_i}=\frac{\partial}{\partial x_i}\left(\overline{\rho}(D+D_t)\frac{\partial\widetilde{\xi''^2}}{\partial x_i}\right)-2\overline{\rho}\widetilde{N}+2\overline{\rho}(D+D_t)\frac{\partial\widetilde{\xi}}{\partial x_i}\frac{\partial\widetilde{\xi}}{\partial x_i} \quad (2.20)$$

The scalar dissipation rate $\widetilde{N}$ is the sum of a resolved and a sub-grid scale part [90]:

$$\widetilde{N}=\widetilde{N}_{res}+\widetilde{N}_{sgs} \quad (2.21)$$

where $\widetilde{N}_{res}$ is the resolved scalar dissipation rate:

$$\widetilde{N}_{res}=D\frac{\partial\widetilde{\xi}}{\partial x_i}\frac{\partial\widetilde{\xi}}{\partial x_i} \quad (2.22)$$

and $\widetilde{N}_{sgs}$ the sub-grid scale part. A gradient model has been suggested to model this term [87, 91]:

$$\widetilde{N}_{sgs}=D_t\frac{\partial\widetilde{\xi}}{\partial x_i}\frac{\partial\widetilde{\xi}}{\partial x_i} \quad (2.23)$$

This model is based on the assumption that the large and the sub-grid scales are in equilibrium and therefore the dissipation rate and the production rate of the variance will be in balance. It cannot be used when a transport equation is solved for the variance of the mixture fraction, because if the dissipation and production rates in Eq. (2.20) are equal, then the variance equation will become a convection-diffusion equation which would imply that it is a conserved scalar, which does not correspond to the real behaviour of this quantity. In this case, modelling in terms of a characteristic time-scale is made [90, 92]:

$$\widetilde{N}_{sgs}=\frac{\nu_t}{\Delta^2}\widetilde{\xi''^2} \quad . \quad (2.24)$$

This is the model that is used in all the simulations presented in this thesis.

2.3 Conditional Moment Closure

2.3.1 Conditional filtering

In the context of LES, the density-weighted conditionally filtered average of a random variable f is defined as [74]:

$$\widetilde{f|\eta}(\eta, \boldsymbol{x}, t) = \frac{\int_{-\infty}^{+\infty} \rho(\boldsymbol{x'}, t) f(\boldsymbol{x'}, t) \delta[\xi(\boldsymbol{x'}, t) - \eta] G(\boldsymbol{x} - \boldsymbol{x'})\, d\boldsymbol{x'}}{\int_{-\infty}^{+\infty} \rho(\boldsymbol{x'}, t) \delta[\xi(\boldsymbol{x'}, t) - \eta] G(\boldsymbol{x} - \boldsymbol{x'})\, d\boldsymbol{x'}} \tag{2.25}$$

where $G(\boldsymbol{x} - \boldsymbol{x'})$ is a filtering function of specified width Δ and η is the sample space variable for ξ. The function $\mathscr{P} = \delta[\xi(\boldsymbol{x'}, t) - \eta]$ is the fine-grained density [93], which is defined so that $\mathscr{P} d\eta$ is the probability that at $\boldsymbol{x}$ and t, ξ will be in the range $\eta < \xi(\boldsymbol{x}, t) < \eta + d\eta$. The density-weighted Filtered probability Density Function (FDF) can be defined as [74]:

$$\widetilde{\mathcal{P}}(\eta; \boldsymbol{x}, t) = \frac{1}{\overline{\rho}(\boldsymbol{x}, t)} \int_{-\infty}^{+\infty} \rho(\boldsymbol{x'}, t) \delta[\xi(\boldsymbol{x'}, t) - \eta] G(\boldsymbol{x} - \boldsymbol{x'})\, d\boldsymbol{x'} \tag{2.26}$$

The filtered value of the variable f can then be obtained by integration over η-space:

$$\widetilde{f} = \int_0^1 \widetilde{f|\eta}\, \widetilde{\mathcal{P}}(\eta)\, d\eta \tag{2.27}$$

2.3.2 Conditionally filtered equation (CMC equation)

The CMC equation can be derived by filtering the transport equations for the mass fractions of species Y_α, $\alpha = 1, n$, where n is the number of species [45]. Using the primary closure hypothesis [44, 45], the CMC equation can be written as:

$$\underbrace{\frac{\partial Q_\alpha}{\partial t}}_{\substack{Unst. \\ term}} + \underbrace{\widetilde{u_i|\eta} \frac{\partial Q_\alpha}{\partial x_i}}_{T1} = \underbrace{\widetilde{N|\eta} \frac{\partial^2 Q_\alpha}{\partial \eta^2}}_{T2} + \underbrace{\widetilde{\omega_\alpha|\eta}}_{T3} + \underbrace{e_f}_{T4} \tag{2.28}$$

where $Q_\alpha = \widetilde{Y_\alpha|\eta}$ is the conditionally filtered mass fraction, $\widetilde{u_i|\eta}$ is the conditionally filtered velocity, $\widetilde{N|\eta}$ is the conditionally filtered scalar dissipation rate, $\widetilde{\omega_\alpha|\eta}$ is the

conditionally filtered reaction rate, while the term

$$e_f = -\frac{1}{\overline{\rho}\,\widetilde{\mathcal{P}}(\eta)}\frac{\partial}{\partial x_i}\left[\overline{\rho}\widetilde{\mathcal{P}}(\eta)\,\left(\widetilde{u_i Y_\alpha|\eta} - \widetilde{u_i|\eta}Q_\alpha\right)\right] \tag{2.29}$$

is the sub-grid scale conditional flux and accounts for conditional transport in physical space. Equal diffusivities for all the species have been considered.

An equation can also be derived for the conditional enthalpy $Q_h = \widetilde{h|\eta}$:

$$\frac{\partial Q_h}{\partial t} + \widetilde{u_i|\eta}\frac{\partial Q_h}{\partial x_i} = \widetilde{N|\eta}\frac{\partial^2 Q_h}{\partial \eta^2} - \widetilde{w_R|\eta} + e_{fh} \tag{2.30}$$

where $\widetilde{w_R|\eta}$ is the heat loss due to radiation and e_{fh} is the sub-grid scale conditional flux of enthalpy:

$$e_f = -\frac{1}{\overline{\rho}\,\widetilde{\mathcal{P}}(\eta)}\frac{\partial}{\partial x_i}\left[\overline{\rho}\widetilde{\mathcal{P}}(\eta)\,\left(\widetilde{u_i h|\eta} - \widetilde{u_i|\eta}Q_h\right)\right] \tag{2.31}$$

In this thesis, the radiation term $\widetilde{w_R|\eta}$ will not be taken into account.

2.3.3 First order closure

The CMC is based on the concept that the fluctuations of the scalars of interest can be correlated with the fluctuations of only one scalar [44]. This appears to be the case in the case of non-premixed flames where it has been observed that the fluctuations of the reacting scalars are correlated with the fluctuations of the mixture fraction [94]. This leads to the notion of first-order closure for the chemical source term in terms of conditional averages; since the fluctuations of the conditional reacting scalars are small, they may be neglected and the conditional chemical source term may be calculated based on the conditional averages of the scalars:

$$\widetilde{\omega_\alpha|\eta} = \omega_\alpha\left(Q_1, Q_2, ..., Q_n, Q_h\right) \tag{2.32}$$

where n is the number of species. This may not be accurate in the case of localised extinction/re-ignition, where the conditional variances and co-variances may play an important role and therefore may have to be taken into account [59]. This would lead to second-order closure [95–97]. Second-order closure has not yet been applied to LES. First-order closure will be used throughout this thesis.

2.3.4 Other unclosed terms

2.3.4.1 Filtered Density Function

The usual practice in mixture fraction based approaches for non-premixed combustion is to presume a shape for the FDF of the mixture fraction. The presumed shape is normally a beta function [89], which necessitates knowledge of the mean and the variance of the mixture fraction. The filtered probability density function is thus assumed to be:

$$\widetilde{\mathcal{P}}(\eta) = \frac{\eta^{\alpha-1}(1-\eta)^{\beta-1}}{B(\alpha,\beta)} \tag{2.33}$$

where

$$B(\alpha,\beta) = \frac{\Gamma(\alpha)\Gamma(\beta)}{\Gamma(\alpha+\beta)} \tag{2.34}$$

is the beta-function and $\Gamma(x)$ is the Gamma function. The parameters

$$\alpha = \widetilde{\xi}\left(\frac{\widetilde{\xi}(1-\widetilde{\xi})}{\widetilde{\xi''^2}} - 1\right) \tag{2.35}$$

and

$$\beta = \frac{\alpha(1-\widetilde{\xi})}{\widetilde{\xi}} \tag{2.36}$$

depend only on the resolved mixture fraction $\widetilde{\xi}$ and its sub-grid variance $\widetilde{\xi''^2}$, for which transport equations are solved (see sections 2.2.4 and 2.2.5). Further validation of the use of a beta function is given in this chapter.

2.3.4.2 Conditionally filtered velocity

In Reynolds-Averaged Navier Stokes models, the usual approach for the conditional velocity is to use the linear model [44]:

$$\langle u_i|\eta\rangle = u_i + \frac{\langle u_i'\xi'\rangle}{\langle\xi''^2\rangle}(\eta - \langle\xi\rangle) \tag{2.37}$$

where the brackets $\langle\rangle$ denote ensemble averaging and $\langle u_i'\xi'\rangle$ is the turbulent flux in the i direction. This model has not yet been validated for LES and the use of a

constant value has been proposed instead [45, 63]:

$$\widetilde{u_i|\eta} = \widetilde{u_i} \tag{2.38}$$

where u_i is the resolved velocity. This model will be used throughout this work.

2.3.4.3 Conditionally filtered scalar dissipation rate

The Amplitude Mapping Closure (AMC) [98] is used here to model the conditionally filtered scalar dissipation rate [63]:

$$\widetilde{N|\eta} = N_0 G(\eta) \tag{2.39}$$

where

$$G(\eta) = exp(-2[erf^{-1}(2\eta - 1)]^2) \tag{2.40}$$

and

$$N_0 = \frac{\widetilde{N}}{\int_0^1 \widetilde{\mathcal{P}}(\eta) G(\eta)\, d\eta} \tag{2.41}$$

where $\widetilde{N}$ is the filtered scalar dissipation rate (resolved and sub-grid scale). In the AMC model, the conditional scalar dissipation rate is considered to have a given shape (function $G(\eta)$) and it is scaled according to the value of the local unconditional scalar dissipation rate $\widetilde{N}$. It has also been proposed that a constant value is used for the conditionally filtered scalar dissipation rate [45], but this is not used here.

2.3.4.4 Conditional flux

The sub-grid scale conditional flux (terms e_f in Eq. (2.28) and e_{fh} in Eq. (2.30)) accounts for the conditional transport in physical space. A gradient model is mostly used to model it [44, 45, 63]:

$$\widetilde{u_i Y_\alpha|\eta} - \widetilde{u_i|\eta} Q_\alpha = -D_t \frac{\partial Q_\alpha}{\partial x_i} \tag{2.42}$$

$$\widetilde{u_i h|\eta} - \widetilde{u_i|\eta} Q_h = -D_t \frac{\partial Q_h}{\partial x_i} \tag{2.43}$$

Note the presence of the turbulent diffusivity D_t, considered to be equal for all the species. In RANS, this is usually taken as the eddy diffusivity associated with the gradient transport model commonly used in the mean mixture fraction equation. In LES, this diffusivity must be equivalent to the sub-grid scale diffusivity used in the filtered equation for the mixture fraction.

2.4 Implementation of the CMC model

The release of heat and the change in composition related with the combustion phenomena investigated in this work may greatly affect the flow. This necessitates the coupling of the flow solver (momentum, mass, mixture fraction and square of mixture fraction) with the CMC solver (conditional species and enthalpy). The two solvers are presented in detail in chapter 3. Here, the focus is on some special issues concerning the communication between the two codes.

2.4.1 Coupling of the CMC and CFD codes

The equations of mass, momentum, mixture fraction and square of mixture fraction are solved by the Rolls Royce Group plc. corporate code PRECISE, analysed in more detail in chapter 3. The CMC equations are solved in an independently defined structured cartesian grid. A schematic of the way the two solvers are coupled is shown in Fig. 2.1.

The information about the velocity field, the mixture fraction field, the turbulent diffusivity and the resolved and sub-grid scale scalar dissipation rate are passed on from the CFD solver to the CMC code. Volume averaging is then performed (detailed in section 2.4.3) which results in the flow field in the CMC resolution. The system of CMC equations is then solved resulting in the conditionally filtered species mass fractions and enthalpy, based on which the conditional temperature and density are calculated. Integration with the FDF over η-space (Eq. (2.27))

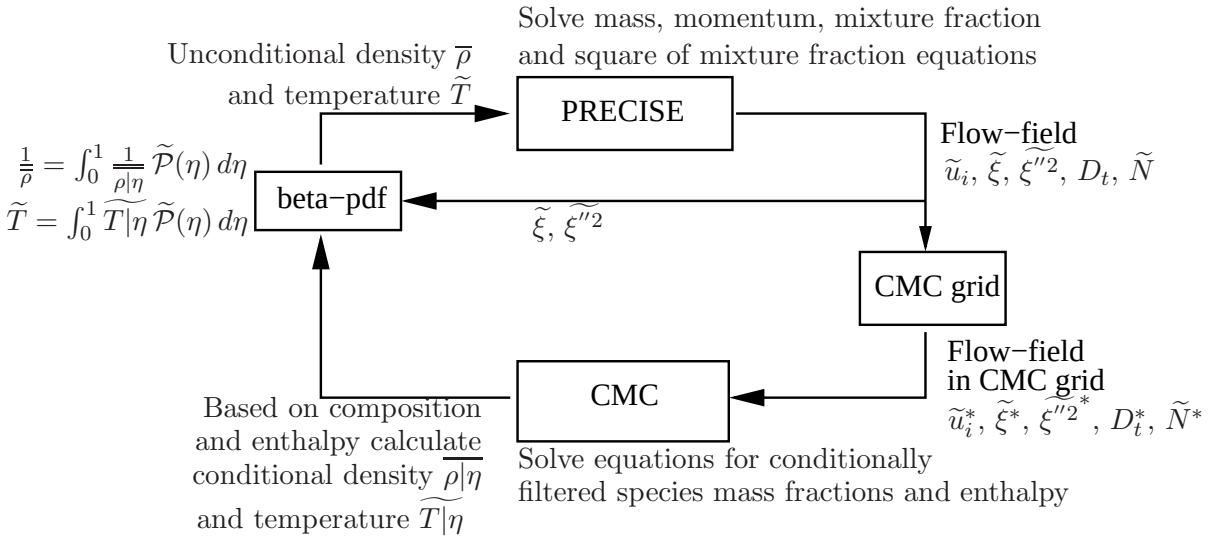

Figure 2.1: Schematic showing the coupling of the CFD and CMC solvers.

yields the unconditional density and temperature which are returned to the CFD solver. This sequence takes place at every timestep of the simulation.

2.4.2 Modelling of the chemical source term

Estimating the chemical source term accurately is essential for any combustion simulation. Chemical mechanisms of varying complexity have been developed for many hydrocarbon fuels. These mechanisms consist of a system of Arrhenius-type reactions between the fuel, oxygen and potentially a number of intermediate species. In principle, the CMC model can operate with chemical mechanisms of any level of detail. The CPU time, however, in the case of very large mechanisms reduces the efficiency of the simulation. The CPU time required does not increase linearly with the number of species of a mechanism, since it depends greatly on the numerical stiffness of the reaction set. The presence of a wide range of characteristic chemical time-scales will have a negative effect on the CPU time. The chemical mechanism that will be chosen for a specific simulation must be the result of a compromise between the necessary accuracy and the speed of the simulation. The mechanisms

used in this thesis are presented in chapter 3.

2.4.3 Numerical aspects

The dimensionality of the CMC domain and the resolution of the mesh depends on the problem considered. Simplifying hypotheses can be made for turbulent shear flows for which the gradients of the conditional scalars in space are not as steep as the gradients of the unconditional scalars [99]. The conditional averages have a different dependence in space than the unconditional ones because the micro-mixing effect is resolved in mixture fraction space and not in physical space. Such hypotheses may lead to the reduction of the dimensionality of the CMC domain (1D or 2D formulation) and/or to coarser CMC grids. Assuming that the CMC equation (Eq. 2.28) will be solved on a grid of resolution Δ_{CMC}, coarser than the grid of resolution Δ_{LES} where the LES is performed, it is evident that information concerning the flow must be transferred from a mesh of resolution Δ_{LES} to one of resolution Δ_{CMC}: the conditional velocity, the conditional turbulent flux, the conditional scalar dissipation and the mixture fraction FDF have to be provided.

These quantities are affected by two separate modelling levels. First, they depend on the model used to transform the unconditional quantities, as supplied from the LES solver, to conditional ones; such models were discussed in section 2.3.4. Second, the quantities appearing in the CMC equation depend on how the LES information, which is available at the resolution Δ_{LES}, is supplied to the CMC solver at resolution Δ_{CMC}. This is discussed in this section.

The different options for transferring the necessary information from the fine LES mesh to the coarser CMC mesh is still an unexplored territory. At the moment, apart from this work, there have been very few LES/CMC calculations [45, 60, 61] and the implementation issues of CMC in LES have not been dealt with in the way they have been in RANS/CMC calculations. The objective of this section is to shed more light into some of these issues themselves, as well as into methods of resolving them.

2.4.3.1 Integrated conditionally filtered equations

Integrating the conditionally filtered average of the random variable f over the volume V_{CMC} of a CMC cell yields:

$$\widetilde{f|\eta}^{*} = \frac{\int_{V_{CMC}} \overline{\rho} \widetilde{f|\eta} \widetilde{\mathcal{P}}(\eta)\, dV'}{\int_{V_{CMC}} \overline{\rho} \widetilde{\mathcal{P}}(\eta)\, dV'} \tag{2.44}$$

which may then be integrated over η-space to obtain the filtered value of f:

$$\widetilde{f} = \int_0^1 \widetilde{f|\eta}^{*}\, \widetilde{\mathcal{P}}(\eta)\, d\eta \tag{2.45}$$

All the volume integrals are integrals over a CMC cell. Note that $\widetilde{f|\eta}^{*}$ is to be calculated by the CMC code at the CMC resolution, while $\widetilde{f}$ and $\widetilde{\mathcal{P}}(\eta)$ are available at the LES resolution. Volume averaging of an unconditional quantity $\widetilde{f}$ will be:

$$\widetilde{f}^{*} = \frac{\int_{V_{CMC}} \overline{\rho} \widetilde{f}\, dV'}{\int_{V_{CMC}} \overline{\rho}\, dV'} \tag{2.46}$$

The CMC equation for the integrated conditionally filtered species mass fractions Q^*_α will be:

$$\frac{\partial Q^*_\alpha}{\partial t} + \widetilde{u_i|\eta}^{*} \frac{\partial Q^*_\alpha}{\partial x_i} = \widetilde{N|\eta}^{*} \frac{\partial^2 Q^*_\alpha}{\partial \eta^2} + \widetilde{\omega_\alpha|\eta}^{*} + e^*_f \tag{2.47}$$

where e^*_f can be modelled as [44]:

$$e^*_f = \frac{1}{\overline{\rho}^*\, \widetilde{\mathcal{P}}^*(\eta)} \frac{\partial}{\partial x_i} \left(\overline{\rho}^* \widetilde{\mathcal{P}}^*(\eta)\, D^*_t \frac{\partial Q^*_\alpha}{\partial x_i} \right) \tag{2.48}$$

in symmetry to the model used in RANS-CMC implementations. The corresponding equations for the integrated conditional enthalpy Q^*_h will be:

$$\frac{\partial Q^*_h}{\partial t} + \widetilde{u_i|\eta}^{*} \frac{\partial Q^*_h}{\partial x_i} = \widetilde{N|\eta}^{*} \frac{\partial^2 Q^*_h}{\partial \eta^2} + e^*_{fh} \tag{2.49}$$

where the radiation term has been omitted for brevity and the term e^*_{fh} can be modelled as:

$$e^*_{fh} = \frac{1}{\overline{\rho}^*\, \widetilde{\mathcal{P}}^*(\eta)} \frac{\partial}{\partial x_i} \left(\overline{\rho}^* \widetilde{\mathcal{P}}^*(\eta)\, D^*_t \frac{\partial Q^*_h}{\partial x_i} \right) \tag{2.50}$$

2.4.3.2 Integrated mixture fraction and its variance

The resolved mixture fraction can be integrated over the volume of each CMC cell to yield the integrated resolved mixture fraction:

$$\widetilde{\xi}^{*} = \frac{\int_{V_{CMC}} \overline{\rho}\widetilde{\xi}\, dV'}{\int_{V_{CMC}} \overline{\rho}\, dV'} \tag{2.51}$$

where $\widetilde{\xi}$ is the resolved mixture fraction.

The evaluation of the integrated sub-grid scale mixture fraction variance is less trivial. The same volume averaging procedure could be used:

$$\widetilde{\xi''^2}^{*} = \frac{\int_{V_{CMC}} \overline{\rho}\widetilde{\xi''^2}\, dV'}{\int_{V_{CMC}} \overline{\rho}\, dV'} \tag{2.52}$$

This variance will be referred to later on as 'variance-1'. In this case the variations of the resolved mixture fraction inside every CMC cell are ignored. These variations may be important, especially in the case of a large $\Delta_{CMC}/\Delta_{LES}$ ratio. They can be included in the calculation of the integrated sub-grid scale mixture fraction by using the following equation, the derivation of which is included in Appendix A:

$$\widetilde{\xi''^2}_2^{*} = \widetilde{\xi}^{\,2*} + \widetilde{\xi''^2}^{\,*} - \widetilde{\xi}^{*2} \tag{2.53}$$

where

$$\widetilde{\xi}^{2*} = \frac{\int_V \overline{\rho}\widetilde{\xi}^{\,2}\, dV'}{\int_V \overline{\rho}\, dV'} \tag{2.54}$$

This variance will be referred to as 'variance-2'.

2.4.3.3 Integrated FDF

The volume averaging that has been used to calculate the integrated resolved mixture fraction could be used to calculate the integrated FDF:

$$\widetilde{\mathcal{P}}^{*}(\eta) = \frac{\int_{V_{CMC}} \overline{\rho}\widetilde{\mathcal{P}}(\eta)\, dV'}{\int_{V_{CMC}} \overline{\rho}\, dV'} \tag{2.55}$$

This FDF will be referred to as $\mathcal{P}_{av-CMC}$.

An alternative to averaging the sub-grid scale FDFs is to use a presumed shape for the integrated FDF in the CMC resolution. $\widetilde{\mathcal{P}}^*(\eta)$ may be assumed to have the shape of a beta function (Eq. (2.33) to (2.36)). In this case, an integrated resolved mixture fraction and an integrated sub-grid scale variance have to be provided. Eq. (2.51) can be used to provide the integrated mixture fraction, while 'variance-1' or 'variance 2' can be used to provide the integrated sub-grid scale variance, which will result in $\mathcal{P}_{1-CMC}$ and $\mathcal{P}_{2-CMC}$ respectively.

2.4.3.4 Integrated conditionally filtered velocity

The conditionally filtered velocity may be integrated over each CMC cell to provide the integrated conditionally filtered velocity:

$$\widetilde{\widetilde{u_i|\eta}}^* = \frac{\int_{V_{CMC}} \overline{\rho}\widetilde{\mathcal{P}}(\eta)\, \widetilde{u_i|\eta}\, dV'}{\int_{V_{CMC}} \overline{\rho}\widetilde{\mathcal{P}}(\eta)\, dV'} \tag{2.56}$$

If the velocity is considered to be constant in η-space, the integrated velocity will be [63]:

$$\widetilde{\widetilde{u_i|\eta}}^* = \frac{\int_{V_{CMC}} \overline{\rho}\widetilde{\mathcal{P}}(\eta)\, \widetilde{u}_i\, dV'}{\int_{V_{CMC}} \overline{\rho}\widetilde{\mathcal{P}}(\eta)\, dV'} \tag{2.57}$$

It has also been suggested that the resolved velocity is conditionally averaged over each CMC cell [45]. This will produce instantaneous profiles of the conditional velocity, which can then be smoothed to provide the final conditional velocity. This is tantamount to neglecting sub-grid velocity fluctuations, which is equivalent to neglecting the sub-grid scalar flux of the mixture fraction, if the linear model of Eq. 2.37 is used as an LES sub-grid model.

2.4.3.5 Integrated conditionally filtered scalar dissipation rate

Conditional averaging over a CMC cell has been suggested for the conditional scalar dissipation rate [45]. This model is very similar to the one applied by the same authors for the conditional velocity.

Alternatively, the conditionally filtered scalar dissipation rate can be integrated over each CMC cell to yield the integrated conditionally filtered scalar dissipation rate:

$$\widetilde{N|\eta}^{*} = \frac{\int_{V_{CMC}} \overline{\rho}\widetilde{\mathcal{P}}(\eta)\, \widetilde{N|\eta}\, dV'}{\int_{V_{CMC}} \overline{\rho}\widetilde{\mathcal{P}}(\eta)\, dV'} \tag{2.58}$$

where $\widetilde{N|\eta}$ can, for example, be provided by the AMC model (Eq. (2.39)-(2.41)). This scalar dissipation rate will be referred to as N_{av}.

Alternatively, the AMC model can be applied directly to the CMC cells:

$$\widetilde{N|\eta}^{*} = N_0^* G(\eta) \tag{2.59}$$

and

$$N_0^* = \frac{\widetilde{N}^*}{\int_0^1 \widetilde{\mathcal{P}}^*(\eta) G(\eta)\, d\eta} \tag{2.60}$$

where $\widetilde{N}^*$ is the integrated filtered scalar dissipation rate:

$$\widetilde{N}^* = \frac{\int_{V_{CMC}} \overline{\rho}\widetilde{N}\, dV'}{\int_{V_{CMC}} \overline{\rho}\, dV'} \tag{2.61}$$

The function $G(\eta)$ is given by Eq. (2.40). In this case, either $\mathcal{P}_{av-CMC}$ or $\mathcal{P}_{2-CMC}$ will be used for $\widetilde{\mathcal{P}}^*(\eta)$, which will result in N_1 and N_2 respectively.

2.4.3.6 Integrated turbulent diffusivity

The integrated turbulent diffusivity appears in the CMC equation when a gradient model is used for the sub-grid scale conditional flux (Eq. (2.48) and (2.50)). This term represents transport via diffusion in space and may therefore be important in cases where there are strong gradients of conditional reacting scalars.

FDF-weighted averaging of the diffusivity has been used in a simulation of a non-premixed bluff-body stabilised jet diffusion flame, thus introducing a dependence on the mixture fraction [63]:

$$D_t^*(\eta) = \frac{\int_{V_{CMC}} \overline{\rho}\widetilde{\mathcal{P}}(\eta)\, D_t\, dV'}{\int_{V_{CMC}} \overline{\rho}\widetilde{\mathcal{P}}(\eta)\, dV'} \tag{2.62}$$

In this case the volume averaging was performed over planes of constant axial distance. This type of averaging procedure implies that information about the turbulence on a small scale (LES resolution) can be extrapolated directly to a larger scale (CMC resolution). For simplicity, in this work, the diffusivity is assumed to be constant in η-space and therefore $\widetilde{\mathcal{P}}(\eta)$ is omitted:

$$D_t^* = \frac{\int_{V_{CMC}} \overline{\rho}\, D_t \, dV'}{\int_{V_{CMC}} \overline{\rho}\, dV'} \tag{2.63}$$

This diffusivity will be referred to as D_{t_1}. An alternative approach to averaging the diffusivity is also proposed here. It is suggested that the integrated turbulent diffusivity is

$$D_t^* = \nu_{t,CMC}^* / \mathrm{Sc_t} \tag{2.64}$$

where $\nu_{t,CMC}^*$ is the 'CMC level' viscosity, calculated using the Smagorinsky model in the CMC resolution:

$$\nu_{t,CMC}^* = (C_S \Delta_{CMC})^2 \, \overline{\mathcal{S}}^* \tag{2.65}$$

where C_S is the Smagorinsky constant and Δ_{CMC} is the filter width of the CMC grid. The integrated characteristic strain rate is

$$\overline{\mathcal{S}}^* = \left(2 \widetilde{S}_{ij}^* \widetilde{S}_{ij}^* \right)^{1/2} \tag{2.66}$$

where

$$\widetilde{S}_{ij}^* = \frac{1}{2} \left(\frac{\partial \widetilde{u}_i^*}{\partial x_j} + \frac{\partial \widetilde{u}_j^*}{\partial x_i} \right) \tag{2.67}$$

is the integrated filtered rate-of-strain tensor, calculated at the CMC resolution using the integrated velocity field:

$$\widetilde{u}_i^* = \frac{\int_{V_{CMC}} \overline{\rho} \widetilde{u}_i \, dV'}{\int_{V_{CMC}} \overline{\rho}\, dV'} \tag{2.68}$$

This diffusivity will be referred to as D_{t_2} and takes account of the fact that the subgrid diffusivity depends on the scale of the diffusion process that is to be modelled.

2.4.3.7 Summary of options

The different options for the integrated quantities used in the CMC equation, and how these are extracted from the LES, are summarised in Table 2.1. Some of these options are tested against experimental data in Sect. 2.4.4, while some are tested through examining the sensitivity of LES-CMC predictions of statistically-steady non-premixed flames in chapter 5.

In more detail, experimental measurements of mixture fraction will be filtered at different levels to assess how well the gradient model of Eq. (2.15) can predict the sub-grid scale variance and to investigate the relative importance of the sub-grid scalar dissipation. Filtering at another level (using a coarser filter grid) will also be performed to examine the different ways of passing information from one resolution to the other and their sensitivity to the different resolutions. More specifically, for the integrated sub-grid scale variance, 'variance-1' and 'variance-2' will be assessed. For the integrated FDF, the suitability of $\mathcal{P}_{av-CMC}$, $\mathcal{P}_{1-CMC}$ and $\mathcal{P}_{2-CMC}$ will be examined. Moreover, it will be investigated whether N_{av}, N_1 and N_2 can be used to provide the integrated conditionally filtered scalar dissipation rate.

2.4.4 Experimental Data Processing

In order to investigate further the different methods of extracting information from a fine grid to a coarser grid, experimental measurements of mixture fraction in an inert mixing flow are analysed in the context of filtering at various resolutions. This provides a guidance on the accuracy expected for the information transfer between LES and CMC grids. The objective of this analysis is to perform filtering of measurements of mixture fraction in a non-reacting flow at various levels in the context of the Filtered Density Function (FDF) and the conditionally filtered scalar dissipation rate, which are quantities that appear explicitly in the CMC equation.

Table 2.1: Summary of different options for integrated quantities

Quantity	**Name**	**Options**
Mixture fraction	$\widetilde{\xi}^*$	$\widetilde{\xi}^* = \frac{\int_{V_{CMC}} \overline{\rho}\widetilde{\xi}\, dV'}{\int_{V_{CMC}} \overline{\rho}\, dV'}$
Mixture fraction variance	Variance-1	$\widetilde{\xi''^2}^* = \frac{\int_{V_{CMC}} \overline{\rho}\widetilde{\xi''^2}\, dV'}{\int_{V_{CMC}} \overline{\rho}\, dV'}$
	Variance-2	$\widetilde{\xi''^2}_2^* = \widetilde{\xi}^{2*} + \widetilde{\xi''^2}^* - \widetilde{\xi}^{*2}$
Filtered Density Function	P_{av-CMC}	$\widetilde{\mathcal{P}}^*(\eta) = \frac{\int_{V_{CMC}} \overline{\rho}\widetilde{\mathcal{P}}(\eta)\, dV'}{\int_{V_{CMC}} \overline{\rho}\, dV'}$
	P_{1-CMC}	Presumed beta-shape using $\widetilde{\xi}^*$ and variance-1
	P_{2-CMC}	Presumed beta-shape using $\widetilde{\xi}^*$ and variance-2
Scalar dissipation rate	$\widetilde{N}^*$	$\widetilde{N}^* = \frac{\int_{V_{CMC}} \overline{\rho}\widetilde{N}\, dV'}{\int_{V_{CMC}} \overline{\rho}\, dV'}$
Conditional scalar dissipation rate	N_{av}	$\widetilde{N\|\eta}^* = \frac{\int_{V_{CMC}} \overline{\rho}\widetilde{\mathcal{P}}(\eta)\, \widetilde{N\|\eta}\, dV'}{\int_{V_{CMC}} \overline{\rho}\widetilde{\mathcal{P}}(\eta)\, dV'}$
	N_1	AMC model using $\widetilde{N}^*$ and P_{av-CMC}
	N_2	AMC model using $\widetilde{N}^*$ and P_{2-CMC}
Diffusivity	D_{t_1}	$D_t^* = \frac{\int_{V_{CMC}} \overline{\rho}\, D_t\, dV'}{\int_{V_{CMC}} \overline{\rho}\, dV'}$
	D_{t_2}	$D_t^* = \nu_t^*/Sc_t, \quad \nu_t^* = (C_S\Delta_{CMC})^2\, \overline{\mathcal{S}}^*$

2.4.4.1 Experimental setup and filtering parameters

The experimental results from a previous study of a turbulent axisymmetric plume [100, 101] are analysed. The experimental apparatus (Fig. 2.2) consists of an optically polished quartz tube of $D = 34.0\,\text{mm}$ inner diameter confining the co-flow of air. Turbulence in the co-flow was generated by a grid with $M = 3.0\,\text{mm}$ diameter holes and 44% solidity, positioned 63 mm upstream of the nozzle to allow the turbulence to develop. The injected stream consisted of a mixture of nitrogen (N_2) and acetylene (C_2H_2), with the mass fraction of acetylene being $Y_{C_2H_2} = 0.73$. The acetylene was injected through a tube of inner diameter $d = 2.24\,\text{mm}$ and outer diameter $d_o = 2.96\,\text{mm}$. The co-flow velocity was equal to 3.09 m/s, while the acetylene velocity was equal to 2.91 m/s. The air stream was pre-heated to 473 K, while the acetylene stream was pre-heated to 438 K. This experimental set-up had previously been used also for autoignition investigations [102].

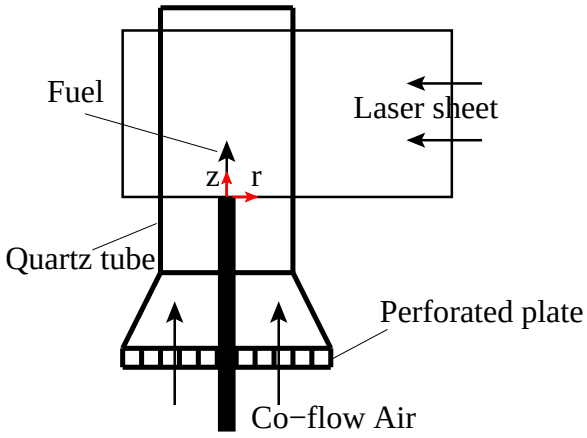

Figure 2.2: Experimental set-up showing the fuel injection point, the co-flow of air and the laser sheet.

PLIF images were used for measuring concentrations. The volume fraction-based mixture fraction was then calculated according to the following definition:

$$\xi_n(r,z) = \frac{n_{fuel}(r,z)}{n_{fuel}(r=0,z=0)} \tag{2.69}$$

where r and z are the radial and axial direction respectively and $n_{fuel}(r,z)$ are molar concentrations, which can be converted into a mass fraction-based mixture fraction by $\xi = [1-(1-\xi_n^{-1})\delta_{inj}^{-1}]^{-1}$ where δ_{inj} is the injection to co-flow density ratio. The acetylene was injected at $(r=0, z=0)$. The two-dimensional scalar dissipation rate was also evaluated from the measurements of ξ:

$$N = D\left[\left(\frac{\partial\xi}{\partial r}\right)^2 + \left(\frac{\partial\xi}{\partial z}\right)^2\right] \tag{2.70}$$

where D is the molecular diffusivity. Extensive description of the experimental set-up and the measuring techniques can be found in Ref. [100]. The signal-to-noise ratio, the filtering procedure and the effects of the latter on the estimation of the mixture fraction gradients, are discussed at length in Ref. [100]. In short, the scalar dissipation is considered to be adequately resolved, as found by performing an independent overall balance of the scalar energy, following the suggestion by Bilger [103].

This study focuses on the investigation of individual images from the experiment in a 'LES/CMC context'. The domain for which data is available is 17.75 mm × 59.23 mm and the original resolution is 301 × 1002 pixels, in the radial and axial direction respectively, resulting in a spatial pixel resolution of $p = 0.06$ mm/pixel. Considering the combined effect of the collection optics pixel resolution and the sheet-making optics effectiveness, the overall spatial resolution was estimated to be equal to $D_{exp} = 0.09$ mm [100]. The Kolmogorov lengthscale has been evaluated to be equal to $\eta_K = 0.25$ mm [100]. The integral lengthscale $\mathcal{L}$ at the exit of the jet is approximately 3.5 mm increasing by about 1 mm in the first 42 mm downstream [101]. The ratio of the fluctuation of the local axial velocity over the mean decreases from approximately 0.15 at the exit of the nozzle to 0.1 at 42 mm downstream, giving a turbulent Reynolds number $\mathrm{Re}_{\mathrm{turb}} = 48$ [101].

A schematic showing all the filtering processes that were performed is shown in Fig. 2.3. The grid that was used for the filtering is what will be called the 'LES grid' and its filter size ranges from $D_{LES}/D_{exp} = 4$ ($D_{LES}/\eta_K = 1.44$) to

$D_{LES}/D_{exp} = 16$ ($D_{LES}/\eta_K = 5.76$). This resolution would correspond to an LES, since the filter size is in the inertial range ($\eta_K < D_{LES} < \mathcal{L}$). However, due to the low Re_{turb}, D_{LES} is not much larger than η_K, as it would be in a flow with higher turbulence levels. Nevertheless, the investigation of these data gives insight into the information transferring process between the meshes.

The original experimental data were filtered to generate what will be referred to as the 'resolved' mixture fraction:

$$\widetilde{\xi} = \frac{\int_{V_{LES}} \xi \, dV'}{\int_{V_{LES}} dV'} \tag{2.71}$$

where ξ is the measured mixture fraction. A sub-grid scale variance was also calculated:

$$\widetilde{\xi''^2} = \frac{\int_{V_{LES}} (\xi - \widetilde{\xi})^2 \, dV'}{\int_{V_{LES}} dV'} \tag{2.72}$$

The scalar dissipation was averaged in the same way as the mixture fraction, resulting in the filtered scalar dissipation field:

$$\widetilde{N} = \frac{\int_{V_{LES}} N \, dV'}{\int_{V_{LES}} dV'} \tag{2.73}$$

where N is the experimental scalar dissipation rate. A resolved scalar dissipation was also calculated based on the gradients of the resolved mixture fraction:

$$\widetilde{N}_{res} = D \left[\left(\frac{\partial \widetilde{\xi}}{\partial z} \right)^2 + \left(\frac{\partial \widetilde{\xi}}{\partial r} \right)^2 \right] \tag{2.74}$$

Subtracting the resolved scalar dissipation rate from the filtered results in the sub-grid scale scalar dissipation rate:

$$\widetilde{N}_{sgs} = \widetilde{N} - \widetilde{N}_{res} \tag{2.75}$$

A second filtering grid ('CMC grid') was then applied to the experimental data to calculate the experimental FDF and conditional scalar dissipation rate. The size of this filter ranges from $D_{CMC}/D_{LES} = 1$ to $D_{CMC}/D_{LES} = 5$. The same grid was applied to the resolved flow field to represent what happens normally where a

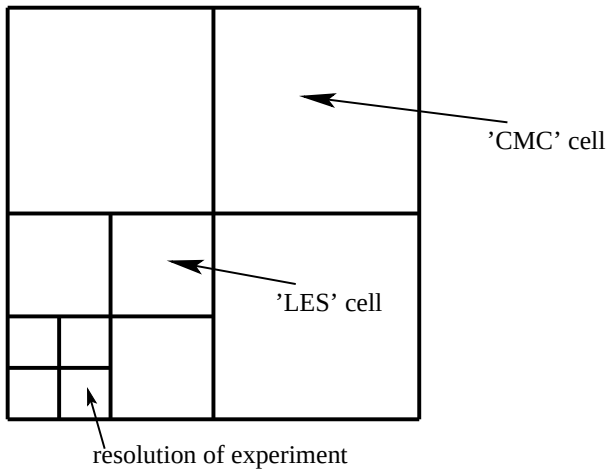

Figure 2.3: Schematic showing the different filtering grids that were used.

CMC grid is used together with an LES grid. The integrated mixture fraction, its sub-grid scale variance, FDF and conditionally filtered scalar dissipation rate were then calculated. To assess how consistent the results are, four different images were analysed.

It is noted that a top-hat filter is used, meaning that the values of all the filtered quantities are considered to remain constant in the cell.

2.4.4.2 Effect of the LES resolution

Resolved mixture fraction The contours of the mixture fraction and scalar dissipation rate fields from the original experimental data are shown in Fig. 2.4 and 2.5, respectively. The instantaneous image that will be examined most closely is image-1. By definition the mixture fraction is equal to unity at the exit of the fuel and zero at the co-flow. There seems to be a potential core in the jet which is about four jet diameters long, which then starts breaking up until complete mixing is achieved. The regions of high scalar dissipation are thin layer-like structures.

The axial decay of the mixture fraction, as well as the instantaneous radial profiles at different axial positions of the mixture fraction for the different 'LES resolutions',

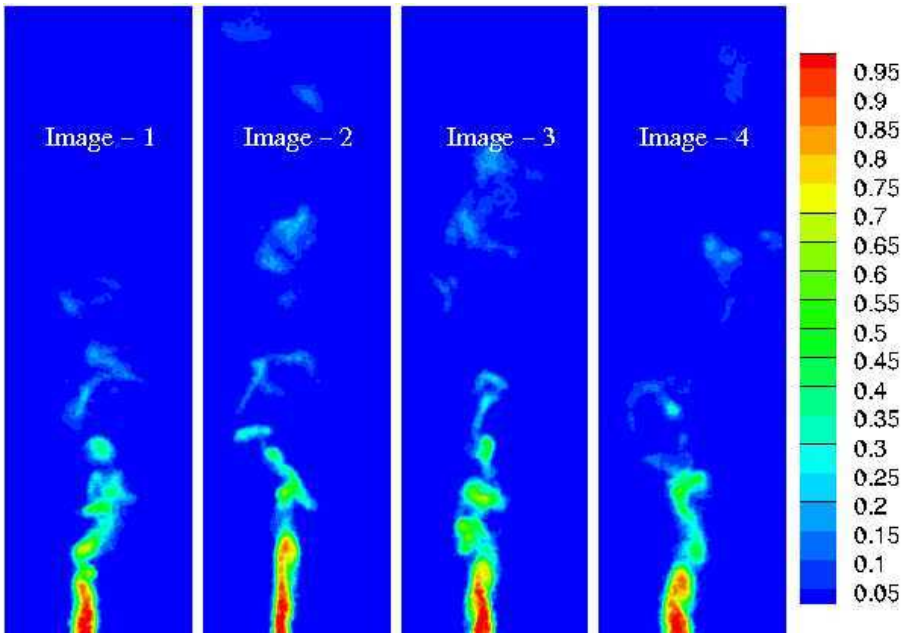

Figure 2.4: Experimental data, mixture fraction. Image shown is 18×60 mm. The flow comes from below.

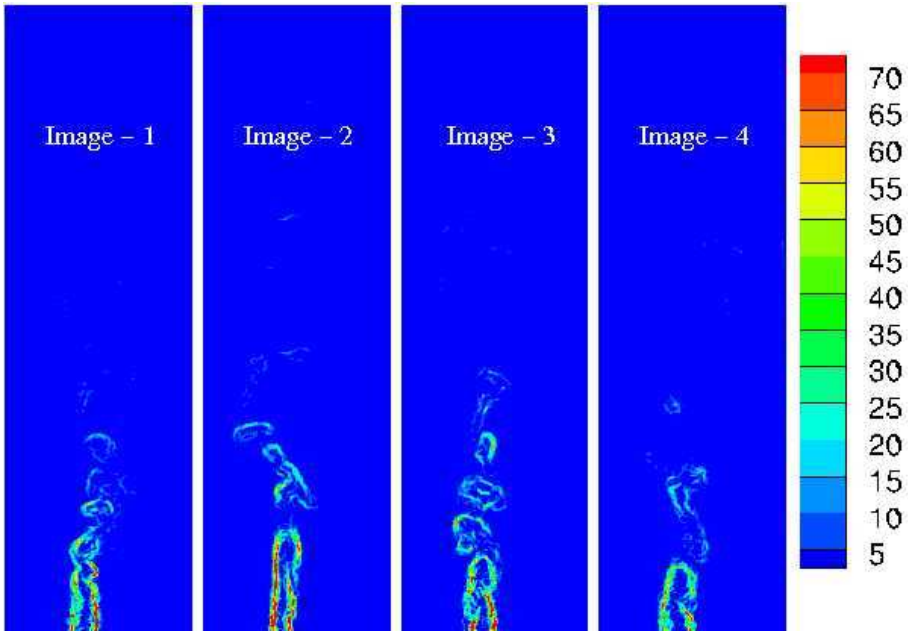

Figure 2.5: Experimental data, scalar dissipation rate $[s^{-1}]$. Image shown is 18×60 mm.

i.e. filtering using different filter sizes, can be found in Fig. 2.6. The results from the three different 'LES resolutions' seem to agree reasonably well with the experimental data. Only in the case where the 'LES grid' is coarse ($D_{LES}/D_{exp} = 16$) some discrepancy can be seen between the experimental value and the resolved mixture fraction. This is confirmed in Fig. 2.7 where the instantaneous radial profiles of the mixture fraction at a certain axial position ($z = 15\,\mathrm{mm}$) are plotted for the four different images.

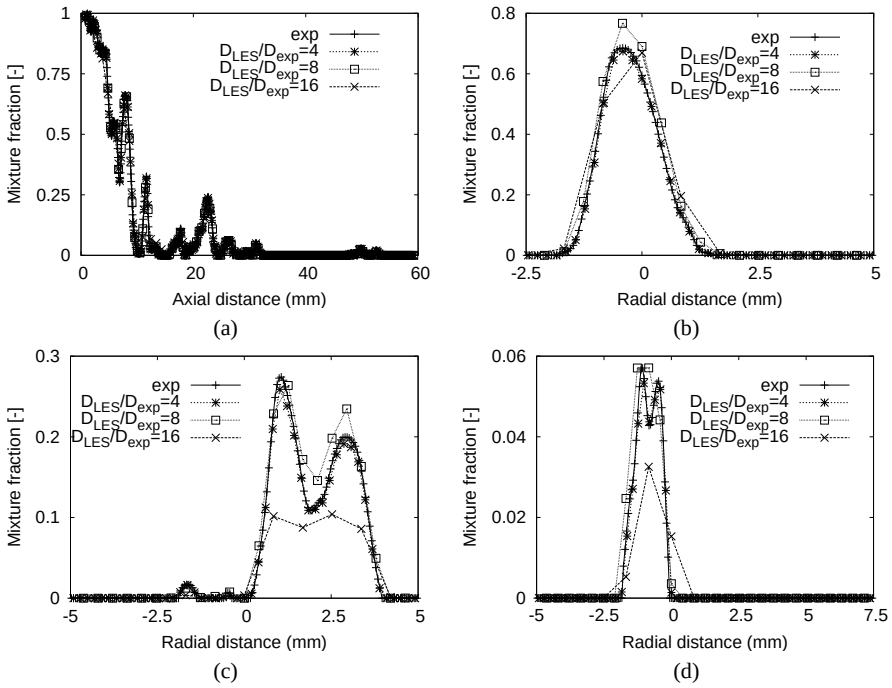

Figure 2.6: Resolved mixture fraction, image-1; (a) axial decay, (b) radial profile, $z = 5\,\mathrm{mm}$, (c) radial profile, $z = 15\,\mathrm{mm}$, (d) radial profile, $z = 30\,\mathrm{mm}$.

Sub-grid scale variance The instantaneous radial profiles of the sub-grid scale variance of the mixture fraction are plotted in Fig. 2.8 for three different axial positions, for the three 'LES resolutions'. As is expected, the sub-grid scale variance decreases along the axis as mixing takes place and the mixture fraction field becomes more homogeneous. The value of the sub-grid scale variance increases as the 'LES

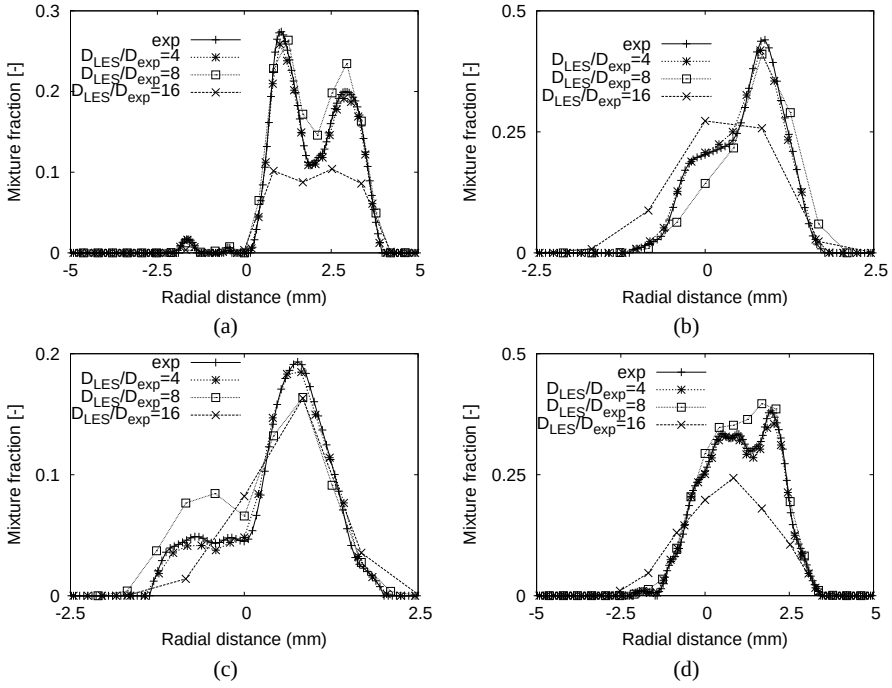

Figure 2.7: Radial profiles of resolved mixture fraction at $z = 15\,\mathrm{mm}$; (a) image-1, (b) image-2, (c) image-3, (d) image-4.

grid' becomes coarser. The sub-grid scale variance when $D_{LES}/D_{exp} = 16$ is almost one order of magnitude higher than when $D_{LES}/D_{exp} = 4$. As the resolution becomes poorer, more scales become sub-grid and there is more mixing taking place in a sub-grid scale level, which is quantified by an increase of the sub-grid scale variance. The shape of the profile remains the same for the different resolutions, but some of the details are lost in the coarser grid.

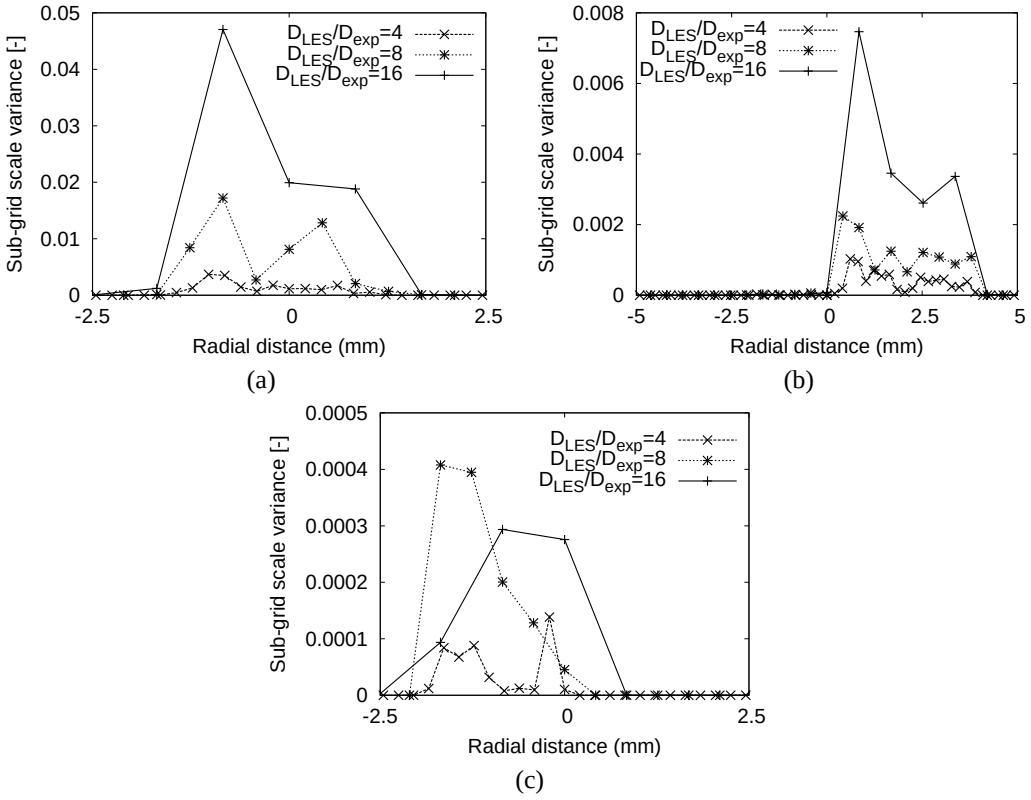

Figure 2.8: Radial profiles of the sub-grid scale variance, image-1; (a) $z = 5\,\mathrm{mm}$, (b) $z = 15\,\mathrm{mm}$, (c) $z = 30\,\mathrm{mm}$.

The parameter C_V from Eq. (2.15) is plotted in Fig. 2.9 in three different axial positions for the three 'LES resolutions'. Most of the points are clustered around a constant value of $C_V = 0.1$, but there seems to be a certain level of scattering, especially in the position which is furthest downstream ($z = 30\,\mathrm{mm}$). The fact

that all the points are clustered around a value is confirmed in Fig. 2.10 where the parameter C_V is plotted in a certain axial position for the four instantaneous images. In every case, the points are clustered around the value of about $C_V = 0.1$. This value for C_V has been used in LES of non-reacting [88] and reacting [36] turbulent jets. Our data further validate the choice of this value.

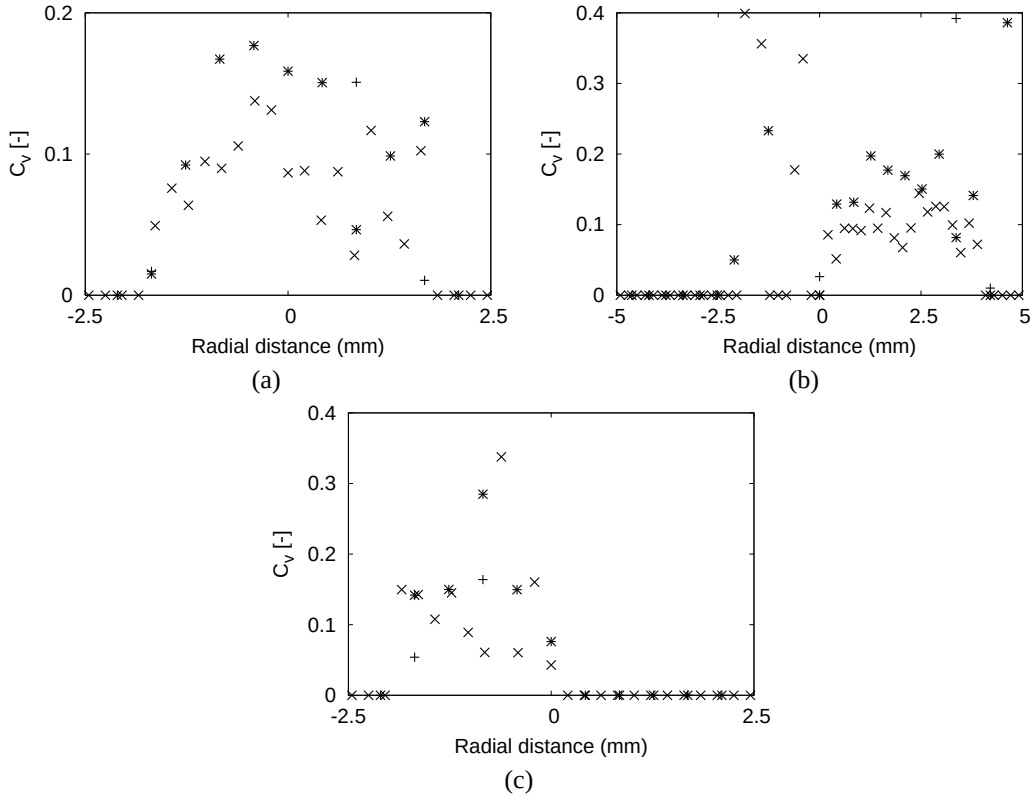

Figure 2.9: Radial profiles of parameter C_V from Eq. (2.15), image-1; (a) $z = 5\,\text{mm}$, (b) $z = 15\,\text{mm}$, (c) $z = 30\,\text{mm}$; $\times : D_{LES}/D_{exp} = 4$, $* : D_{LES}/D_{exp} = 8$, $+ : D_{LES}/D_{exp} = 16$.

Sub-grid scale scalar dissipation rate The contribution of the sub-grid scales to the total scalar dissipation rate for different values of D_{LES}/D_{exp} is plotted in Fig. 2.11. In the initial stage of the jet break-up ($z = 5\,\text{mm}$), the contribution of the sub-grid scales seems to be around 25% of the total scalar dissipation rate,

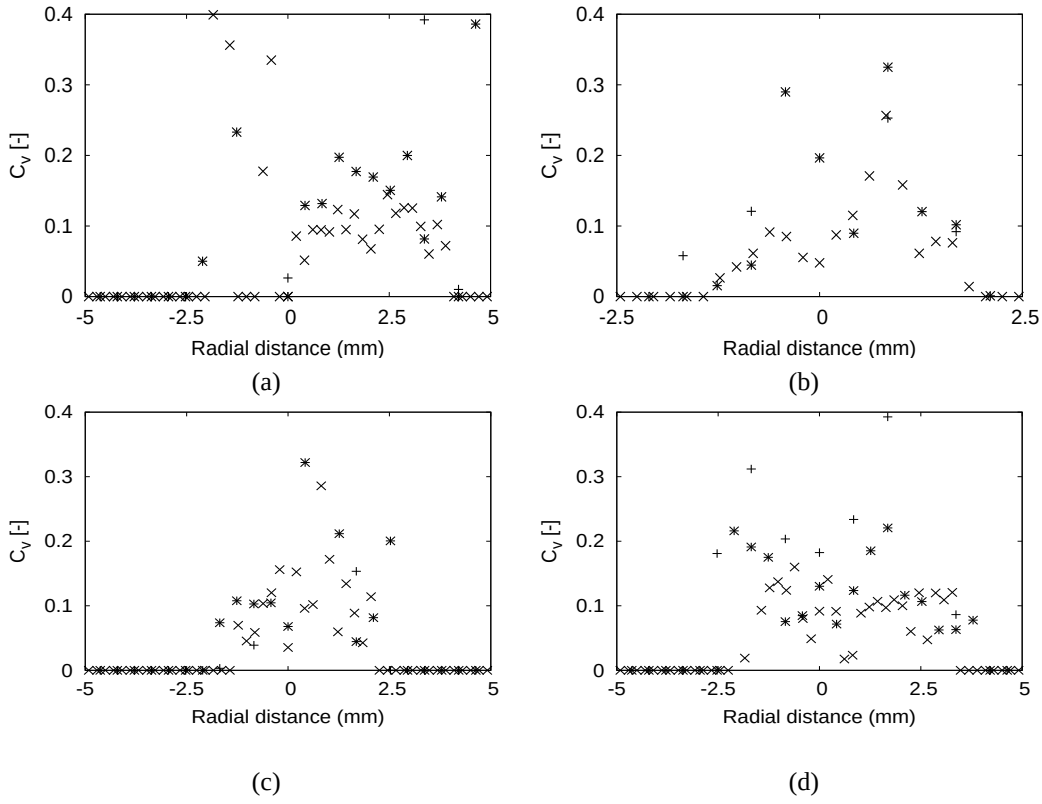

Figure 2.10: Radial profiles of parameter C_V from Eq. (2.15) at $z = 15\,\mathrm{mm}$; (a) image-1, (b) image-2, (c) image-3, (d) image-4; $\times$: $D_{LES}/D_{exp} = 4$, $*$: $D_{LES}/D_{exp} = 8$, $+$: $D_{LES}/D_{exp} = 16$.

reaching around 50% when the grid is coarser. Further downstream ($z = 15\,\text{mm}$), the contribution of the sub-grid scales ranges from 10% up to almost 100% for the coarser grid. In the last axial position, the contribution of the sub-grid scales seems to be somewhat independent of the grid and ranges from 10% to approximately 75%. Similar conclusions may be drawn by Fig. 2.12 where the contribution of the sub-grid scales to the total scalar dissipation rate in a certain axial position is plotted for four different images. It is evident that, depending on the location in the flow and the LES resolution relative to the Batchelor scale, the sub-grid scale scalar dissipation cannot be neglected.

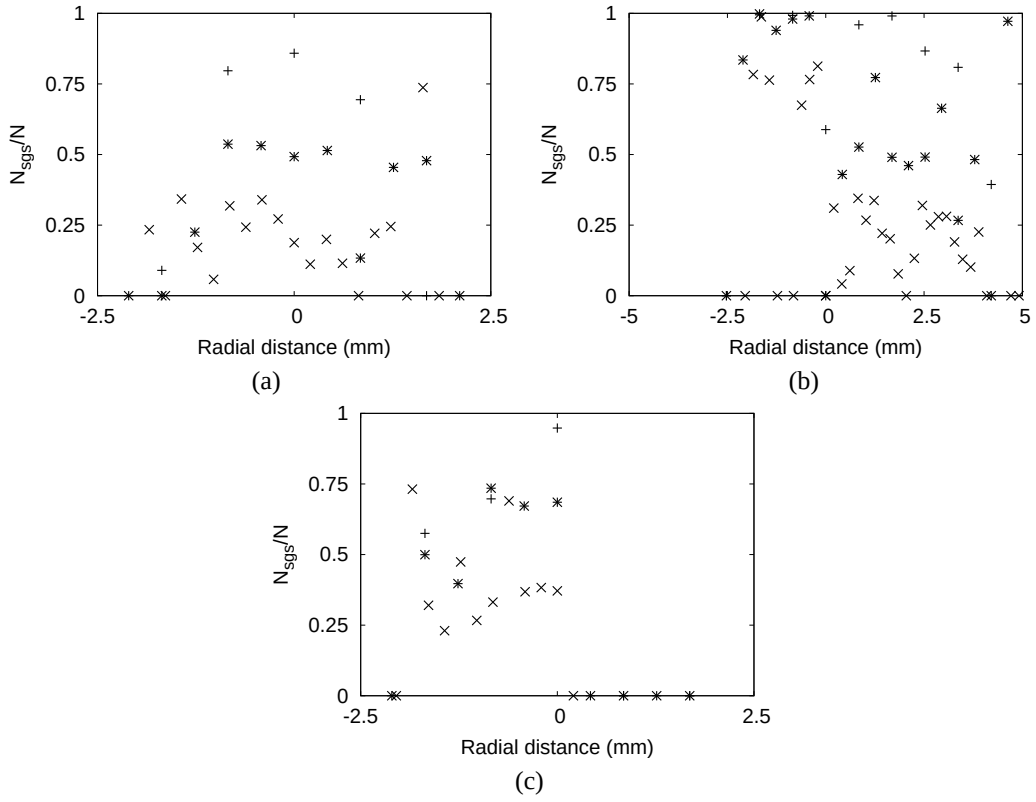

Figure 2.11: Radial profiles of the contribution of the sub-grid scale scalar dissipation rate to the total, image-1; (a) $z = 5\,\text{mm}$, (b) $z = 15\,\text{mm}$, (c) $z = 30\,\text{mm}$; $\times$: $D_{LES}/D_{exp} = 4$, $*$: $D_{LES}/D_{exp} = 8$, $+$: $D_{LES}/D_{exp} = 16$.

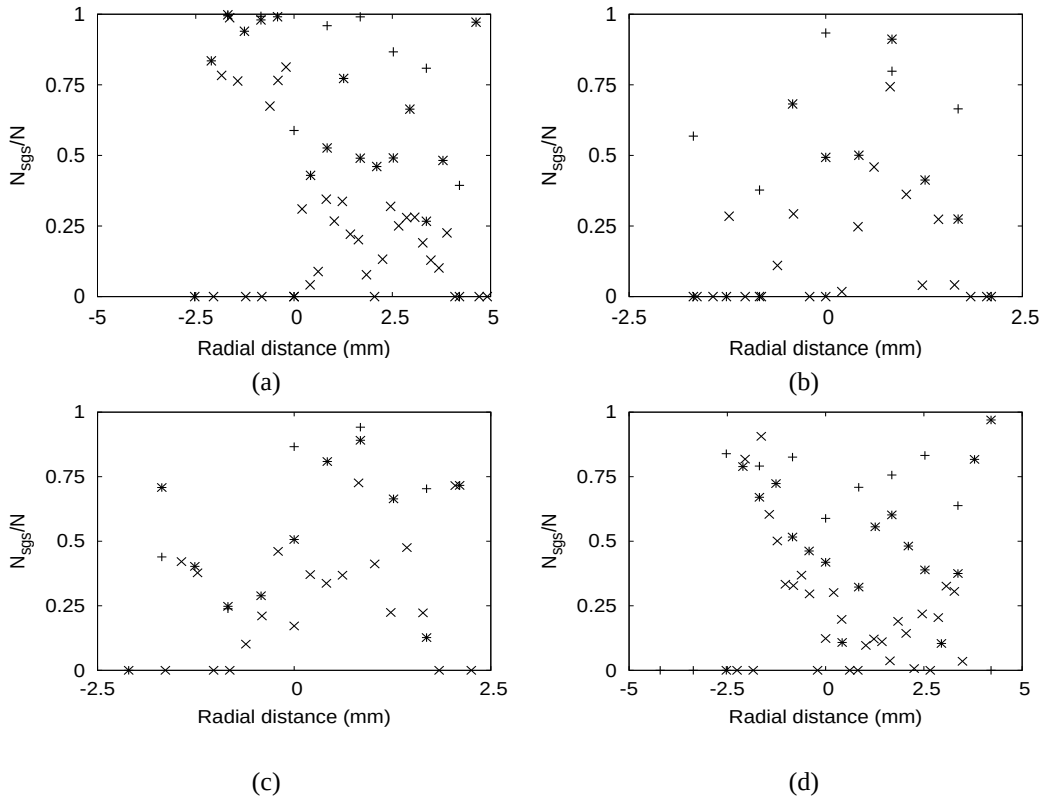

Figure 2.12: Radial profiles of the contribution of sub-grid scale scalar dissipation rate to the total at $z = 15\,\mathrm{mm}$; (a) image-1, (b) image-2, (c) image-3, (d) image-4; $\times : D_{LES}/D_{exp} = 4$, $* : D_{LES}/D_{exp} = 8$, $+ : D_{LES}/D_{exp} = 16$.

2.4.4.3 Effect of the CMC resolution

Integrated mixture fraction In Fig. 2.13, the axial decay and the instantaneous radial profiles of the integrated mixture fraction for the three 'CMC resolutions' are compared with the experimental data. Due to the two filtering procedures ('LES' and 'CMC' filters) some of the initial information regarding the gradients of the mixture fraction has been lost and the profiles are smoother than in the experimental data.

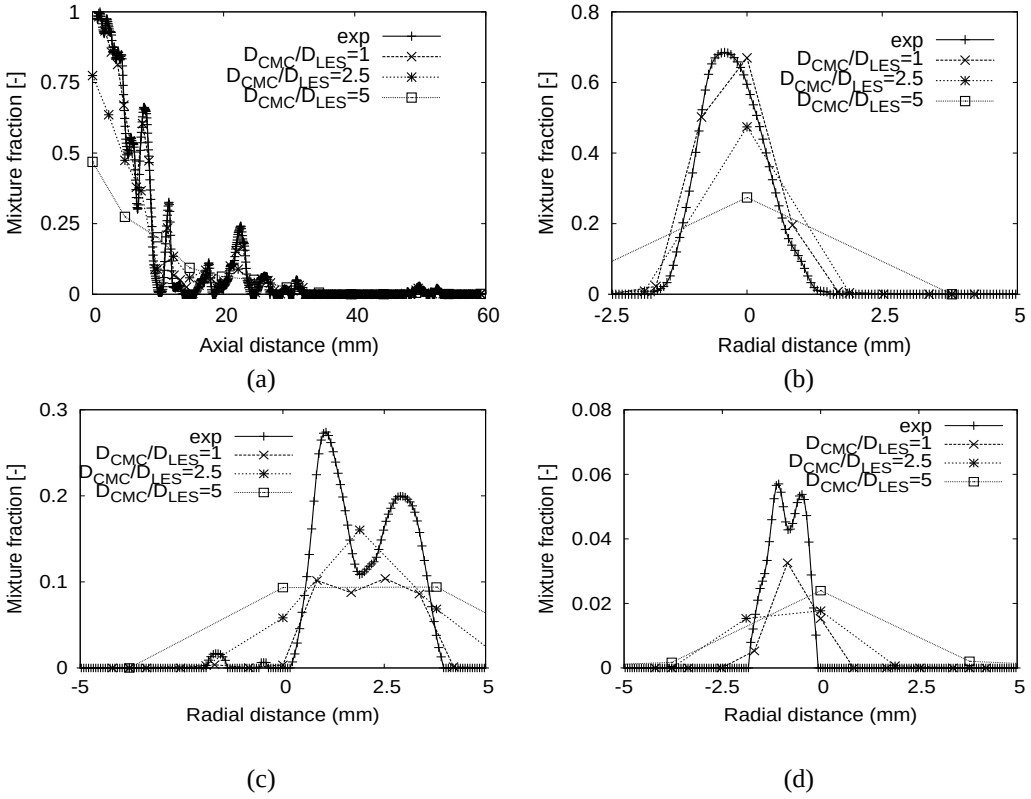

Figure 2.13: Integrated mixture fraction for $D_{LES}/D_{exp} = 4$, image-1; (a) axial decay, (b) radial profile, $z = 5\,\mathrm{mm}$, (c) radial profile, $z = 15\,\mathrm{mm}$, (d) radial profile, $z = 30\,\mathrm{mm}$.

Integrated sub-grid scale variance In Fig. 2.14, 2.15 and 2.16 the instantaneous radial profiles of the sub-grid scale variance of the mixture fraction are shown, for one 'LES resolution' ($D_{LES}/D_{exp} = 16$) and for all the 'CMC resolutions'. When $D_{CMC}/D_{LES} = 1$ the three different sub-grid scale variances give identical results, which is expected since the CMC grid and the LES grid are identical. When the 'CMC grid' is coarser than the 'LES grid', it can be seen that variance-1 is almost one order of magnitude smaller than the filtered sub-grid scale variance, whereas variance-2 gives results which are much closer to the real value. This shows that when calculating a sub-grid scale variance on a coarser grid based on information on a finer grid, the major contribution comes from the variation of the resolved field within a cell of the coarser grid and not from the individual sub-grid scale variances of the cells of the finer grid.

Integrated FDF In Fig. 2.17, the FDF in a point which is located along the axis, 5 mm after the injector is shown, evaluated in four different ways (directly from the experimental data and three methods mentioned in Table 2.1), for the three 'CMC resolutions' respectively. In the case when the LES and CMC grids are identical, the three methods collapse onto the same line and the comparison with the experimental FDF gives an estimate of how well it can be represented by a beta-FDF. The suitability of this model has been confirmed in the past by comparison with results from DNS [104]. Fig. 2.17 confirms these results, as the presumed-shape FDF is close to the experimental FDF.

The other two cases lead to the conclusion that the best representation of the FDF (experimental FDF) comes from the volume average of the individual FDFs in a CMC cell ($\mathcal{P}_{av-CMC}$). It seems, however, that a presumed shape in the 'CMC resolution' can also be used, if the correct variance is used. Using variance-1 results in a very narrow FDF ($\mathcal{P}_{1-CMC}$), while using variance-2 results in a FDF ($\mathcal{P}_{2-CMC}$) which approximates the experimental FDF reasonably well. Due to the nature of the beta-function, $\mathcal{P}_{2-CMC}$ always predicts a wider and smoother FDF, losing the

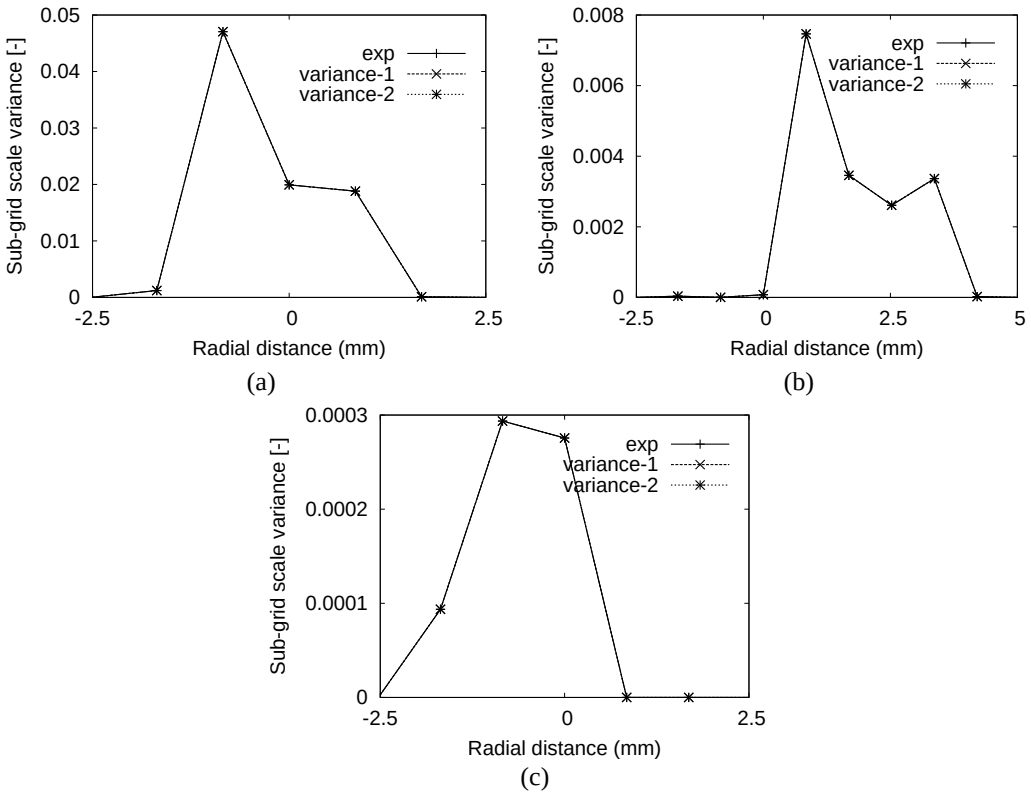

Figure 2.14: Radial profiles of integrated sub-grid scale mixture fraction variance for $D_{LES}/D_{exp} = 16$, $D_{CMC}/D_{LES} = 1$, image-1; (a) $z = 5\,\mathrm{mm}$ (b) $z = 15\,\mathrm{mm}$, (c) $z = 30\,\mathrm{mm}$.

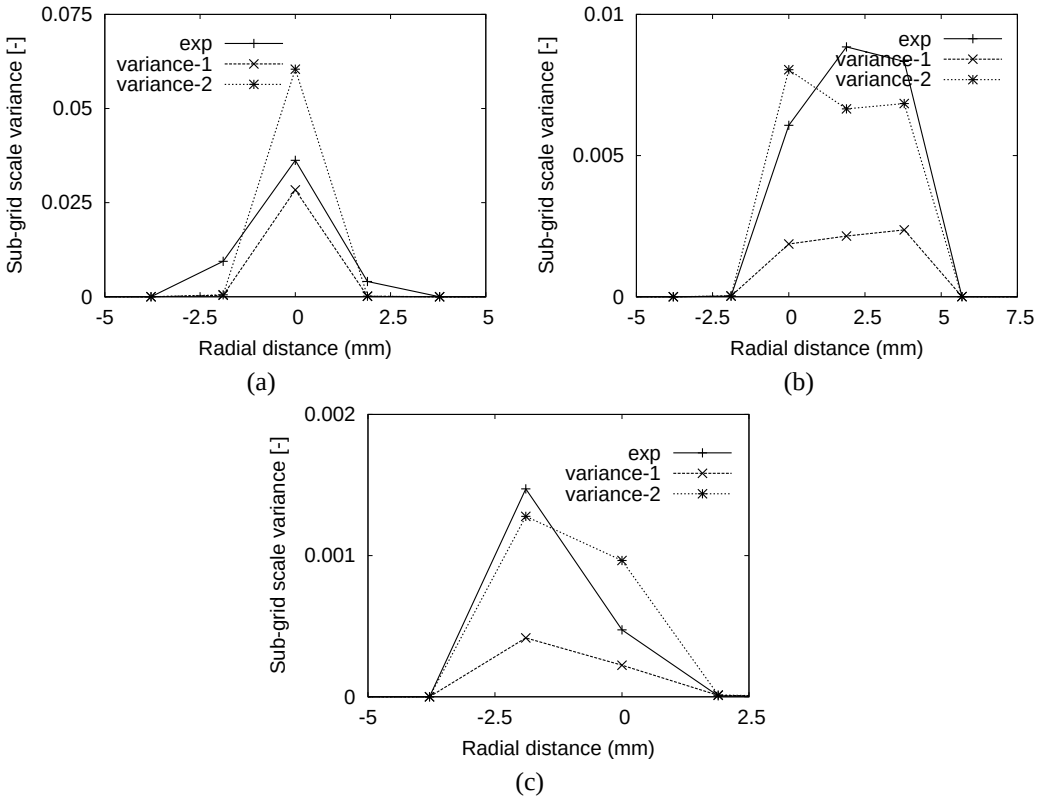

Figure 2.15: Radial profiles of integrated sub-grid scale mixture fraction variance for$D_{LES}/D_{exp} = 16$, $D_{CMC}/D_{LES} = 2.5$, image-1; (a) $z = 5\,\mathrm{mm}$ (b) $z = 15\,\mathrm{mm}$, (c) $z = 30\,\mathrm{mm}$.

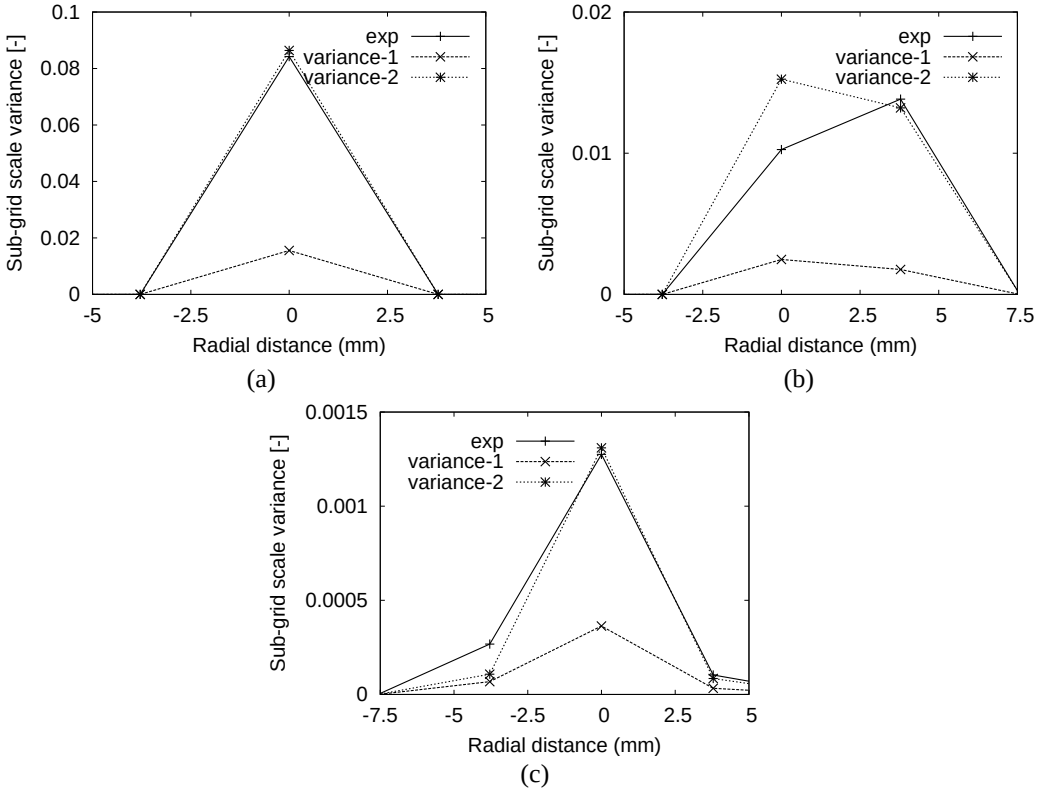

Figure 2.16: Radial profiles of integrated sub-grid scale mixture fraction variance for $D_{LES}/D_{exp} = 16$, $D_{CMC}/D_{LES} = 5$, image-1; (a) $z = 5\,\mathrm{mm}$ (b) $z = 15\,\mathrm{mm}$, (c) $z = 30\,\mathrm{mm}$.

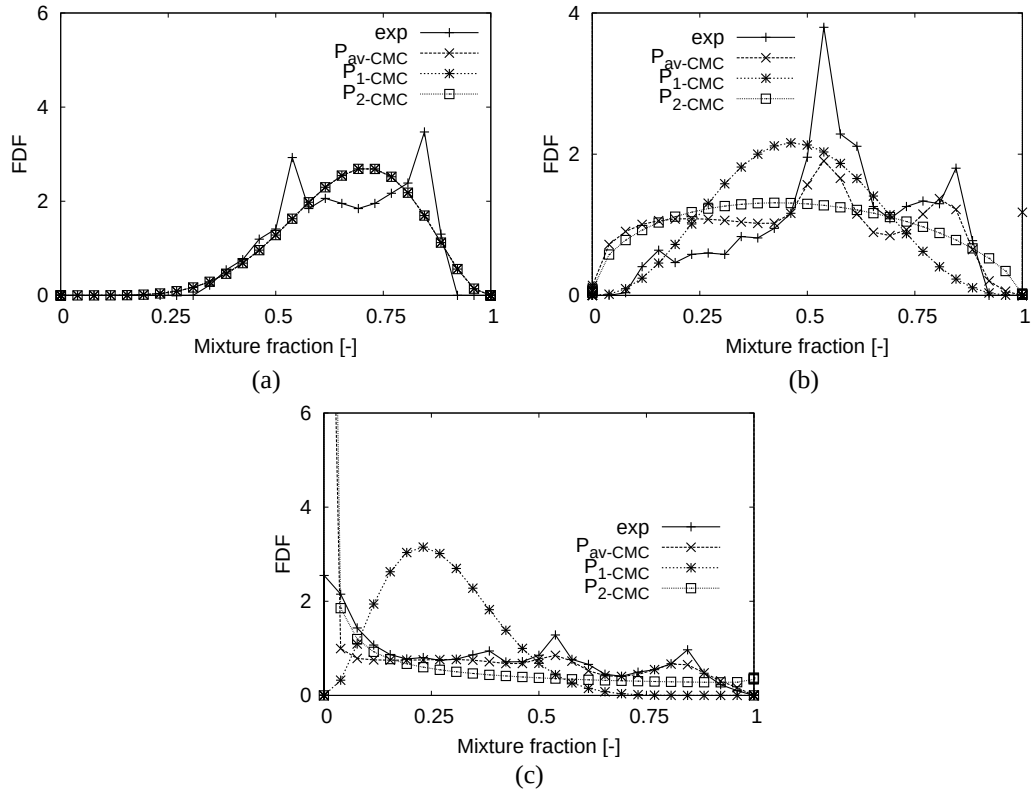

Figure 2.17: Integrated FDF at $z = 5\,\mathrm{mm}$ for $D_{LES}/D_{exp} = 16$, image-1; (a) $D_{CMC}/D_{LES} = 1$, (b) $D_{CMC}/D_{LES} = 2.5$, (c) $D_{CMC}/D_{LES} = 5$.

details of multiple peaks and steep gradients in mixture fraction space. This may result to a FDF very different to the experimental one (e.g. Fig. 2.17b) or not (e.g. Fig. 2.17c) depending on the variation of the mixture fraction inside a CMC cell.

In order to assess how consistent these results are, the FDF was evaluated for one 'CMC resolution' ($D_{CMC}/D_{LES} = 2.5$) for five locations along the axis (Fig. 2.18) and for one location ($z = 5\,\mathrm{mm}$), but for four instantaneous images (Fig. 2.19). These figures confirm the conclusion that while the most accurate FDF is the averaged FDF from all the individual FDFs in the CMC cell, a presumed shape can also be used, as long as a realistic variance, such as 'variance 2', is used.

Integrated conditionally filtered scalar dissipation rate In Fig. 2.20, the different options for the integrated conditionally filtered scalar dissipation rate are plotted, for the three 'CMC resolutions', for one location along the axis ($z = 5\,\mathrm{mm}$), compared with the experimental data. N_1 and N_2 predict the trend and the magnitude reasonably well in all cases, while N_{av} seems to over-predict the scalar dissipation rate in some cases (Fig. 2.20c and 2.21d and 2.21e). The AMC model is unable to capture multiple peaks, always predicting a bell-shaped curve, which covers all mixture fractions, but overall it seems to capture the correct trend.

The consistency of these results was tested by examining five locations along the axis of the jet (Fig. 2.21) and four images for one 'CMC resolution' ($D_{CMC}/D_{LES} = 2.5$) (Fig. 2.22). These figures can confirm the conclusion that N_1 and N_2 give very similar results and that either of them may be used. Some differences between the results of the models is noticed in some graphs, but the trend is always the same and the magnitude is very similar, especially where the FDF is finite and therefore the notion of a conditional scalar dissipation rate is valid.

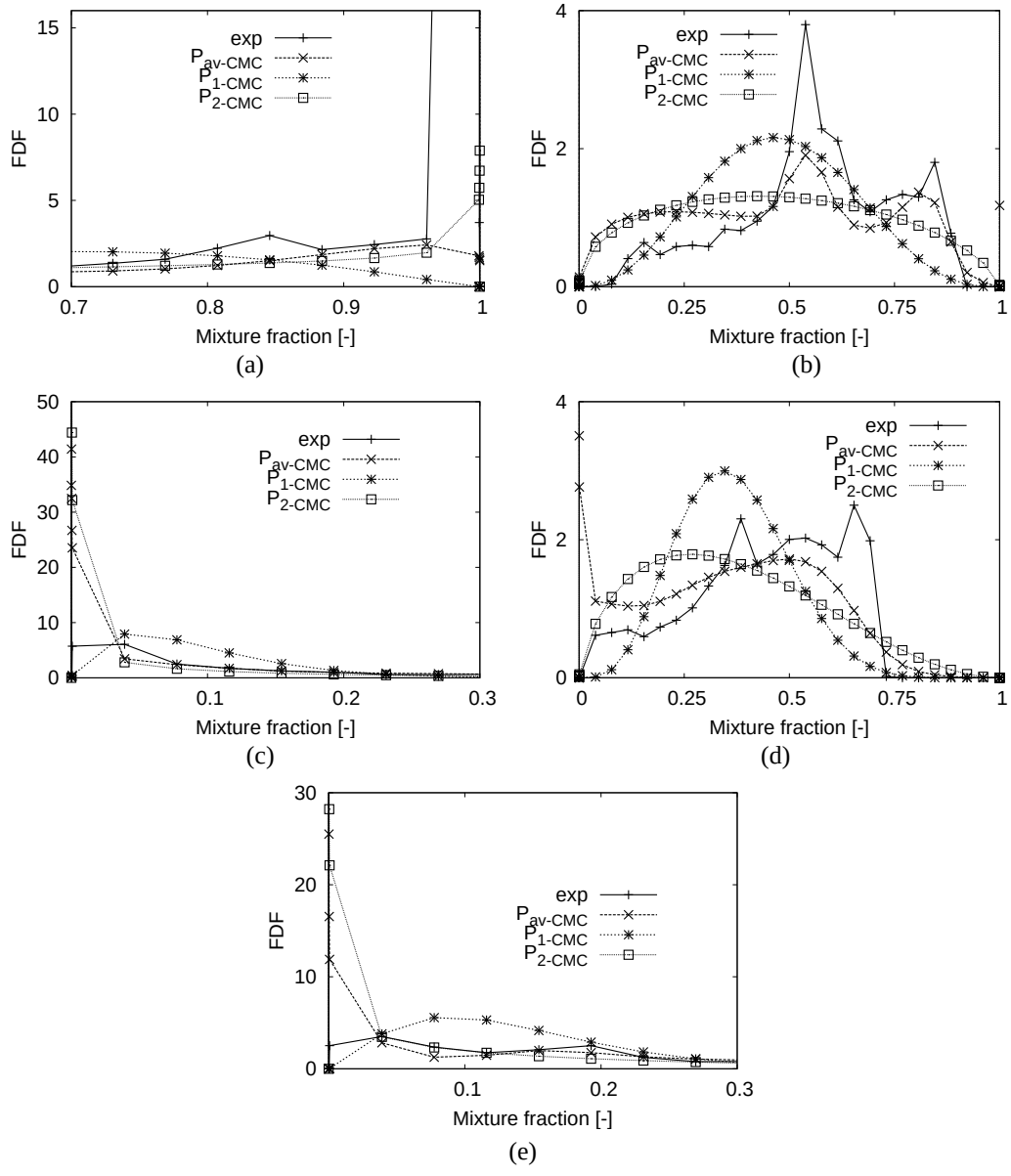

Figure 2.18: Integrated FDF for $D_{LES}/D_{exp} = 16$, $D_{CMC}/D_{LES} = 2.5$; (a) $z = 2.5\,\mathrm{mm}$, (b) $z = 5\,\mathrm{mm}$, (c) $z = 7.5\,\mathrm{mm}$, (d) $z = 10\,\mathrm{mm}$, (e) $z = 12.5\,\mathrm{mm}$.

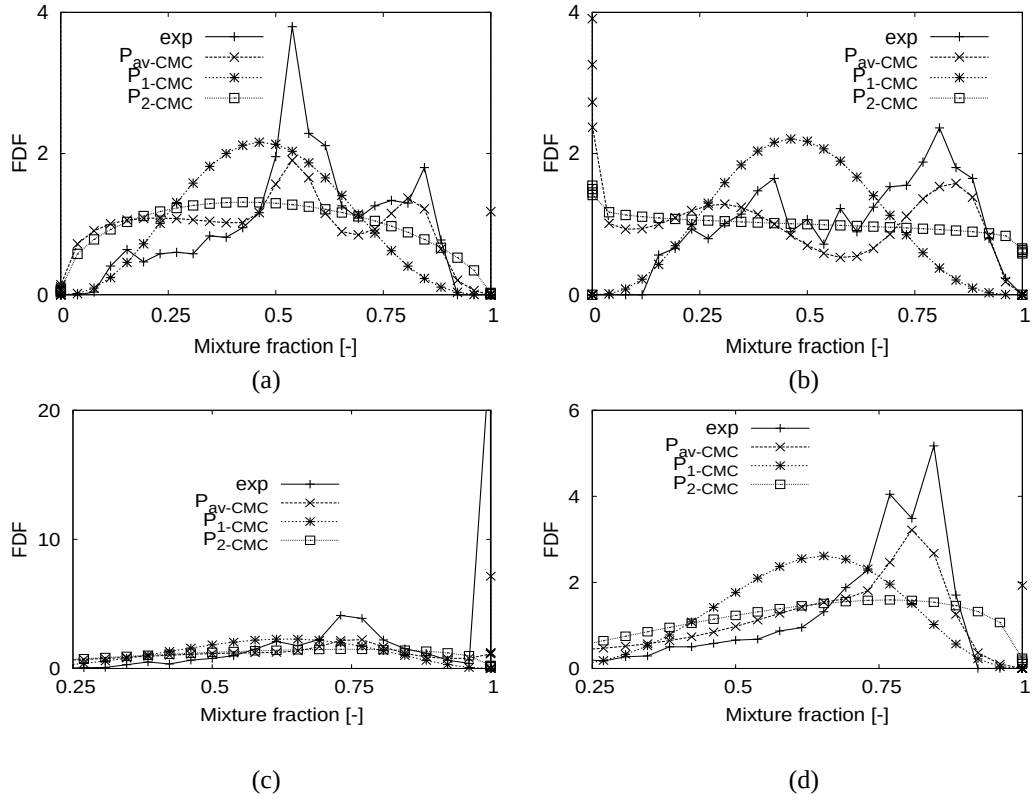

Figure 2.19: Integrated FDF at $z = 5\,\mathrm{mm}$ for $D_{LES}/D_{exp} = 16$ and $D_{CMC}/D_{LES} = 2.5$; (a) image-1, (b) image-2, (c) image-3, (d) image-4.

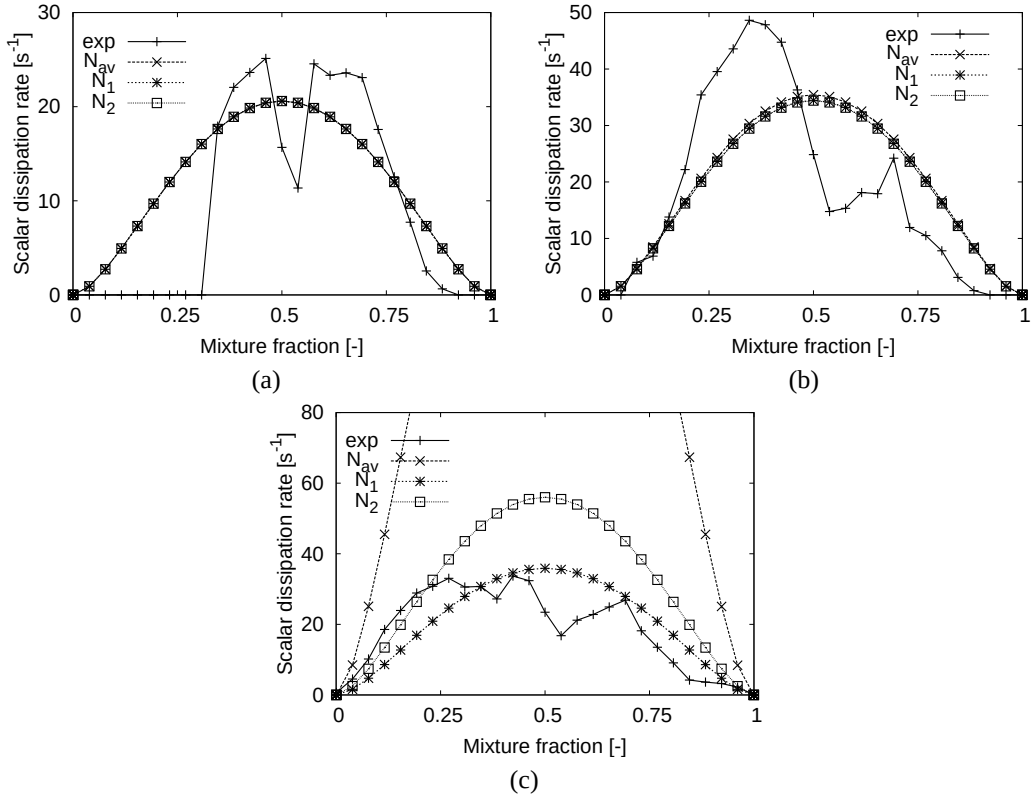

Figure 2.20: Integrated conditionally filtered scalar dissipation rate at $z = 5\,\mathrm{mm}$ for $D_{LES}/D_{exp} = 16$, image-1; (a) $D_{CMC}/D_{LES} = 1$, (b) $D_{CMC}/D_{LES} = 2.5$, (c) $D_{CMC}/D_{LES} = 5$.

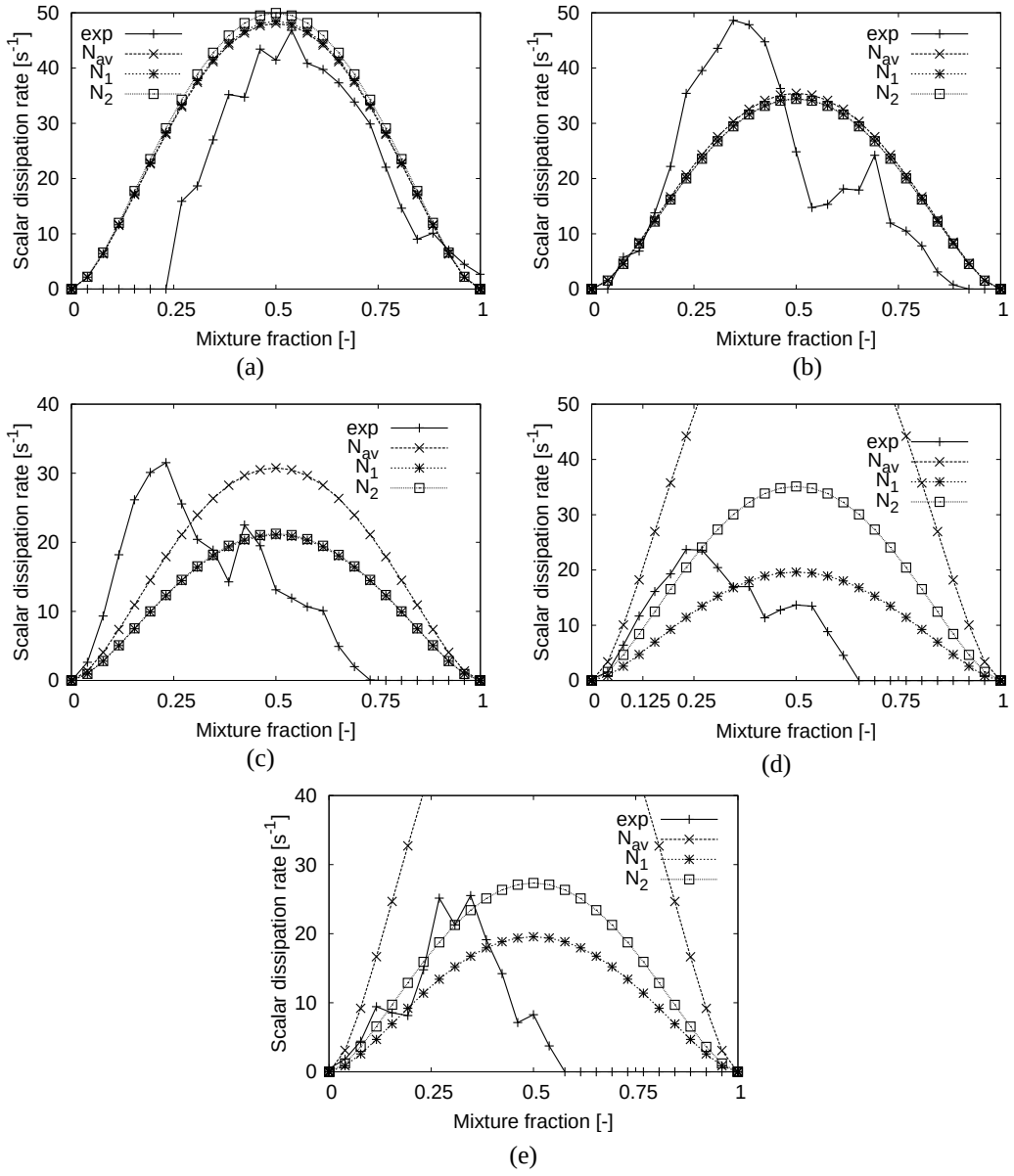

Figure 2.21: Integrated conditionally filtered scalar dissipation rate for $D_{LES}/D_{exp} = 16$ and $D_{CMC}/D_{LES} = 2.5$; (a) $z = 2.5\,\mathrm{mm}$, (b) $z = 5\,\mathrm{mm}$, (c) $z = 7.5\,\mathrm{mm}$, (d) $z = 10\,\mathrm{mm}$, (e) $z = 12.5\,\mathrm{mm}$.

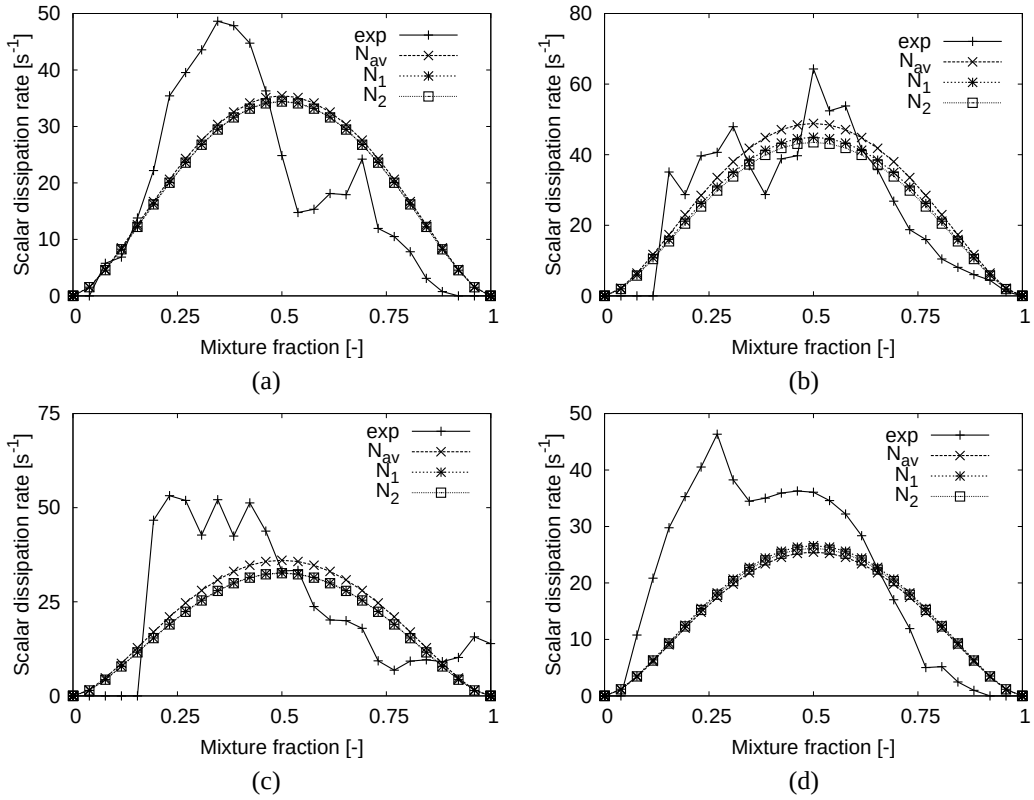

Figure 2.22: Integrated conditionally filtered scalar dissipation rate at $z = 5\,\mathrm{mm}$ for $D_{LES}/D_{exp} = 16$ and $D_{CMC}/D_{LES} = 2.5$; (a) image-1, (b) image-2, (c) image-3, (d) image-4.

2.5 Models and sub-models used

All the LES and CMC models that are used in the simulations presented in this thesis (unless stated otherwise) are summarised in table 2.2.

2.6 Conclusions

The governing equations for LES and CMC have been presented in this chapter. The different sub-models were discussed and the implementation of the CMC method in LES was also presented. The two methods are fully coupled to allow for the simulations of transient phenomena (more details about the computational codes are included in chapter 3). Special attention was given to the fact that in practical applications of the CMC in LES, a coarser mesh than the LES is used to solve the CMC equations. Information concerning the flow must be transferred from the LES to the CMC mesh.

In order to evaluate the accuracy of the different options of transferring data from one mesh to the other, high resolution experimental data of mixture fraction were filtered. In particular, they were used to assess a model for the sub-grid scale variance of the mixture fraction, the contribution of the sub-grid scale scalar dissipation rate and different ways of transferring the sub-grid scale mixture fraction variance, the FDF and the scalar dissipation rate from a fine 'LES grid' to a coarser 'CMC grid'.

The gradient model may be used for the sub-grid scale mixture fraction variance using a constant parameter, as long as the LES grid is not very coarse, in which case the parameter might have to be dynamically calculated. The contribution of the sub-grid scales to the total scalar dissipation rate seems to be small at the initial stage of the break-up of the jet where the mixing is controlled by the larger scales, but becomes more significant further downstream.

When transferring data from a fine LES grid to a coarser CMC grid, the variation of the resolved mixture fraction inside a CMC cell must be included in the calculation

Table 2.2: Models used in this thesis (unless stated otherwise).

Quantity	Model
LES models	
Residual stress tensor $\tau_{ij}^r = \widetilde{u_i u_j} - \widetilde{u}_i \widetilde{u}_j$	Dynamic Smagorinsky model, Eq. (2.9)-(2.11), [84].
Sub-grid scale mixture fraction flux $J_i^r = \widetilde{u_i \xi} - \widetilde{u}_i \widetilde{\xi}$	Gradient model, Eq. (2.14), $\mathrm{Sc_t} = 0.7$.
Sub-grid scale mixture fraction variance $\widetilde{\xi''^2}$	Transport equation, Eq. (2.16), (2.17).
Sub-grid scale scalar dissipation rate $\widetilde{N}_{sgs}$	$\nu_t / \Delta^2 \, \widetilde{\xi''^2}$, [90, 92].
CMC models	
Filtered Density Function (FDF) $\widetilde{\mathcal{P}}(\eta)$	Beta-function, Eq. (2.33)-(2.36), [89].
Conditional velocity $\widetilde{u_i \vert \eta}$	$\widetilde{u_i \vert \eta} = \widetilde{u}_i$, [45, 63].
Conditional scalar dissipation rate $\widetilde{N \vert \eta}$	AMC model, Eq. (2.39)-(2.41), [98].
Conditional fluxes $\widetilde{u_i Y_\alpha \vert \eta} - \widetilde{u_i \vert \eta} Q_\alpha$, $\widetilde{u_i h \vert \eta} - \widetilde{u_i \vert \eta} Q_h$	Gradient model, Eq. (2.42), (2.43), [44, 45, 63].
Integrated quantities	
Integrated mixture fraction	Eq. (2.51).
Integrated mixture fraction variance	Eq. (2.53), (2.54).
Integrated FDF	$\mathcal{P}_{2-CMC}$.
Integrated conditional velocity	Eq. (2.57), [63].
Integrated conditional scalar dissipation rate	N_2, Eq. (2.59)-(2.61).
Integrated turbulent diffusivity	D_{t_2}, Eq. (2.64)-(2.68).

of the sub-grid scale variance. An averaged FDF may be used as the integrated FDF, although a presumed beta-FDF may also be used, as long as the integrated variance has the correct value. A model for the conditional scalar dissipation rate may be either calculated at the 'LES resolution' and then averaged to give the integrated conditionally filtered scalar dissipation rate, or it can be applied at the 'CMC resolution' directly using the integrated scalar dissipation rate.

Chapter 3

Numerical Methods and Chemical Mechanisms

3.1 Introduction

The purpose of this chapter is to present the solvers used in the simulations discussed in this thesis. The implementation of the CMC model in LES has already been described in chapter 2. Two solvers are essentially used; the CFD solver solves the mass, momentum, mixture fraction and variance equations, while the CMC solver solves the equations for the conditional species and enthalpy. Since changes in density may cause changes in the velocity and mixture fraction fields, the two solvers are fully coupled. First, the CFD solver PRECISE is introduced and further validated in an inert jet case. Second, the CMC solver is presented. The CMC equations are five-dimensional equations in space, time and mixture fraction space. In addition, the system of equations may be stiff, due to the large variety of different time-scales appearing in the chemical mechanism. In this chapter, the discretisation schemes are presented with special care being given to the convection scheme and to the time-integration method. Finally, the parallelisation of the CMC solver, the boundary and initial conditions, as well as the chemical mechanisms used throughout

this thesis are presented.

3.2 The CFD solver

3.2.1 General

All the simulations presented in this work were performed using the code PRECISE. PRECISE is the Rolls-Royce corporate combustion CFD code. It is a finite-volume code, which uses the low-Mach number formulation (there can be no density changes due to compression). The pressure-correction equation is solved using the SIMPLE algorithm [105].

Convective transport is discretised using a central differencing scheme. Due to the instability of this scheme for high Peclet numbers, it must be ensured that the timestep is small and that large changes in grid spacing are avoided. A central difference scheme is used to solve the pressure-correction equation, while time derivatives are discretized using a second order backward difference scheme and integration in time is done using the explicit Adams-Bashforth method. There is no implicit control of the timestep during the simulation. The user is informed of the maximum CFL number in the flow at every timestep and must explicitly adjust the timestep to ensure that CFL < 1. At the outlet of the domain, it is assumed that no changes occur in the direction of the flow and hence the gradients of all the variables are zero.

PRECISE has been used in LES to assess its suitability for simulations of combustion in gas turbines [106] and in LES of non-premixed flames (Sandia flame D and Sandia/Sydney swirl burners) using the filtered density function turbulent combustion model [107].

3.2.2 Further validation of the code

In order to further validate PRECISE, simulations of an inert jet were performed. This configuration has been used in the past to study forced ignition [22], but only the inert flow will be considered here. The diameter of the jet is $d_j = 5\,\text{mm}$ and the jet exit velocity is $V_j = 25.5\,\text{m/s}$, resulting to a jet Reynolds number of $\text{Re}_\text{j} = 8325$. A laminar co-flow of velocity $V_c = 0.1\,\text{m/s}$ surrounds the jet. The computational mesh was composed of approximately 1 million cells (Fig. 3.1). The computational domain extends to 300 mm ($60d_j$) in the axial direction y and 100 mm ($20d_j$) in the radial direction r. The timestep was chosen to be $dt = 5 \times 10^{-6}\,\text{s}$, resulting in a maximum CFL number in the flow less than 0.2. A top-hat profile was used at the inlet of the jet and white noise was superimposed. The lack of turbulent inlet conditions may lead to inaccuracies in the near-nozzle region [108].

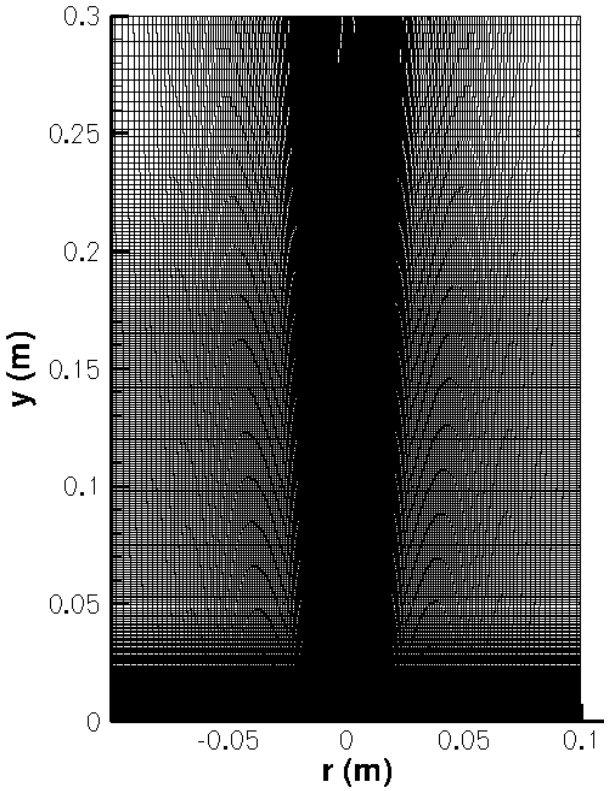

Figure 3.1: Computational mesh for LES of the jet.

An instantaneous snapshot and a time-averaged slice of the axial velocity field are shown in Fig. 3.2.

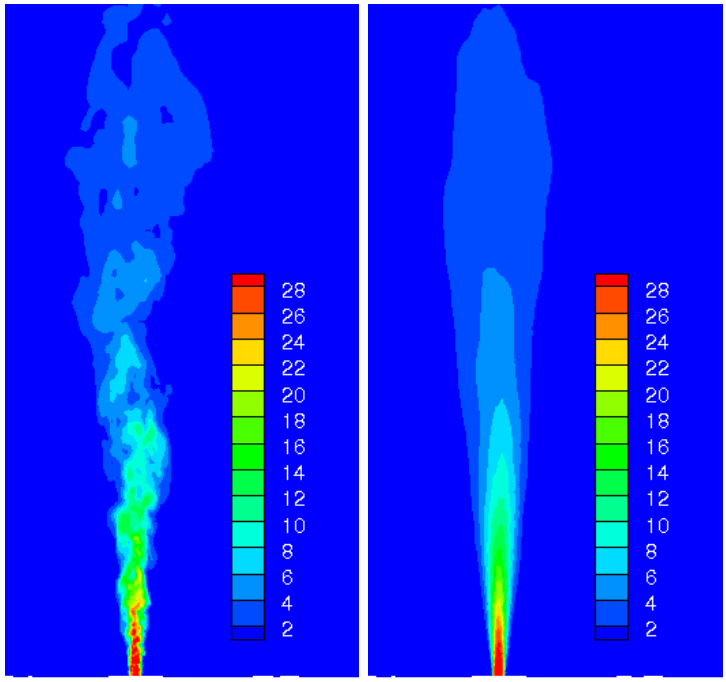

(a) (b)

Figure 3.2: Instantaneous snapshot and time-averaged axial velocity velocity field [m/s].

The velocity measurements were taken with air in the jet and were found to agree very well with the following empirical fit [109], which will be used to validate the LES results [22]:

$$\frac{\overline{V}}{V_j} = 11.8 \left(\frac{\rho_j}{\rho}\right)^{1/2} \left(\frac{d_j}{2y}\right) exp\left[-93.7 \left(\frac{r}{z}\right)^2\right] \tag{3.1}$$

where $\overline{V}$ is the mean axial velocity, ρ_j and ρ are the densities of the jet fluid and the ambient air respectively, y is the axial distance from the exit of the jet and r is the radial distance from the centreline.

The initial stage where the velocity remains almost constant (potential core) is not predicted very accurately (Fig. 3.3), which may be attributed to the lack of

realistic fluctuations at the inlet plane. After about $10d_j$, however, when the self-similarity region begins, the LES results agree very well with the empirical fit. This can also be seen in Fig. 3.4 where radial profiles of the mean and the Root Mean Square (RMS) of the axial velocity are plotted. The LES provides a self-similar solution, slightly over-predicting the magnitude of the velocity. The magnitude of the fluctuations is also predicted accurately. The comparison in the case of the fluctuations is made with the actual experimental data.

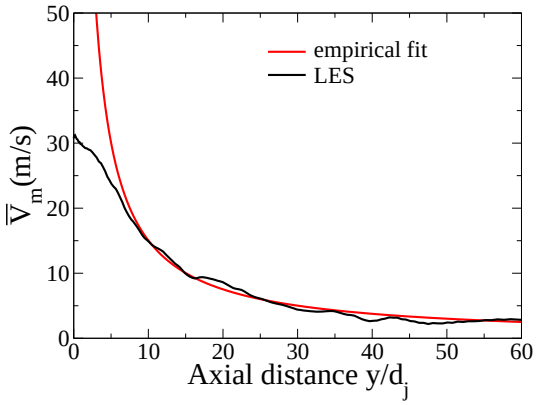

Figure 3.3: Mean axial velocity along the centreline.

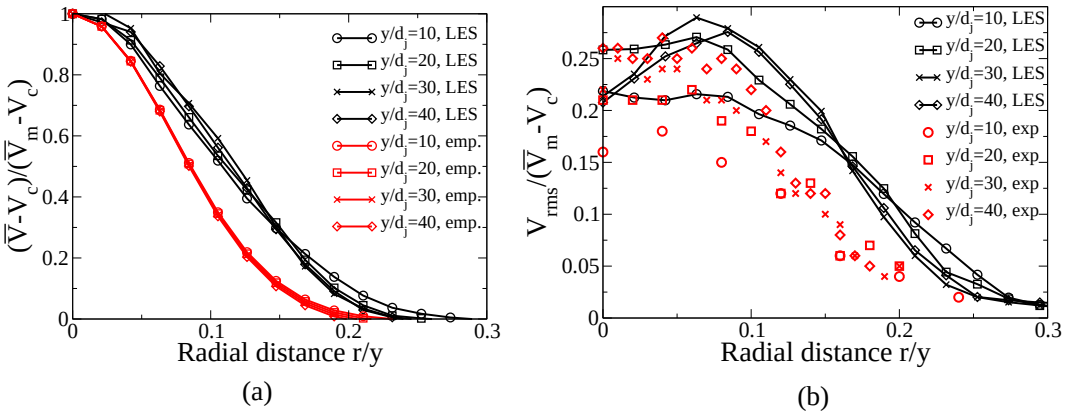

Figure 3.4: Radial profiles of a) mean and b) RMS of axial velocity.

The distribution of the mixture fraction was also considered. The fuel was diluted methane (70% methane, 30% air by volume). An instantaneous snapshot and a time-averaged slice of the mixture fraction field are shown in Fig. 3.5.

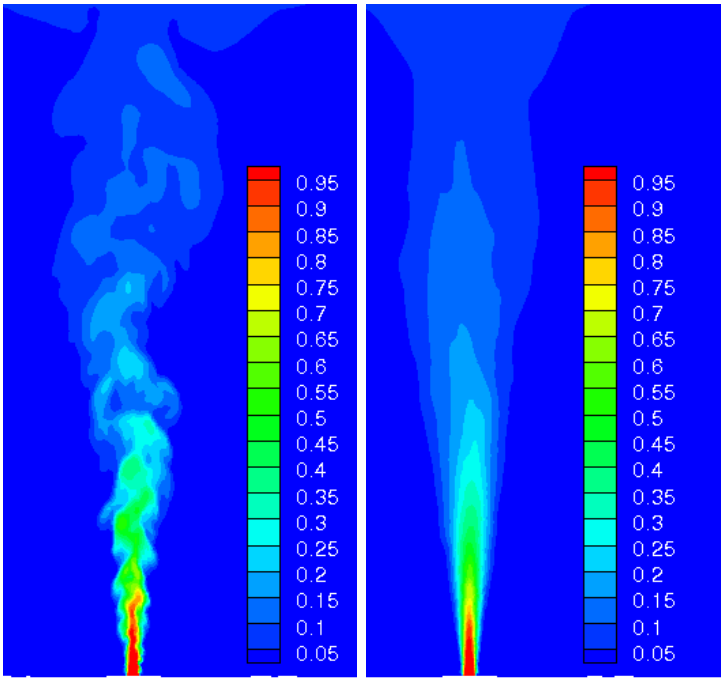

(a) (b)

Figure 3.5: Instantaneous snapshot and time-averaged mixture fraction field.

Due to the unavailability of measurements of the mixture fraction, an empirical fit for the mean and the RMS of the mixture fraction is used [110]:

$$\overline{\xi}(y,\eta) = \frac{9.52 r_\epsilon}{y - y_{0Y}} exp(-59\eta^2) \tag{3.2}$$

$$\xi_{rms}(y,\eta) = \frac{9.52 r_\epsilon}{y - y_{0Y}} [0.23 + 0.35\eta + 9.09\eta^2 - 116.48\eta^3 + 240.81\eta^4] \tag{3.3}$$

where $\overline{\xi}$ is the mean mixture fraction, y is the axial distance from the exit of the jet, $r_\epsilon = (\rho_j/\rho)^{1/2} d_j/2$, y_{OY} is the virtual origin taken to be equal to $3.6 d_j$, $\eta = r/(y - y_{OY})$, r is the radial distance from the centreline and ξ_{rms} is the rms of the fluctuations of the mixture fraction.

As was the case with the decay of the axial velocity at the centreline, the LES prediction is very good after about $10 d_j$ and throughout the self-similar region (Fig. 3.6). This is also shown in Fig. 3.7a where the radial profiles of the mixture fraction are shown for different distances from the exit of the jet. In all cases, the LES

predictions agree reasonably well with the empirical fit. In Fig. 3.7b radial profiles of the RMS of the fluctuations of the mixture fraction are shown, for different distances from the exit of the jet. For the first position ($y = 10d_j$) the LES seems to underpredict the level of the fluctuations. This may be attributed to the inlet boundary conditions. In all the other locations, however, the agreement with the empirical fit is good.

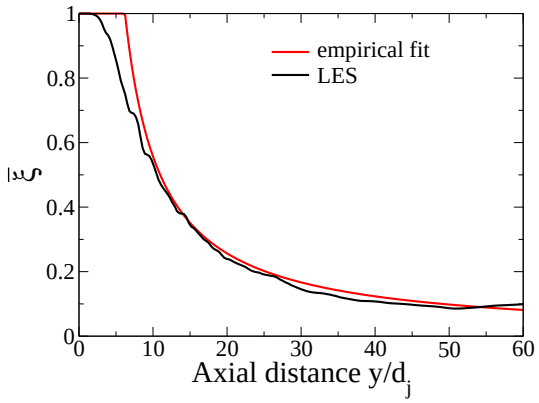

Figure 3.6: Mean mixture fraction along the centreline.

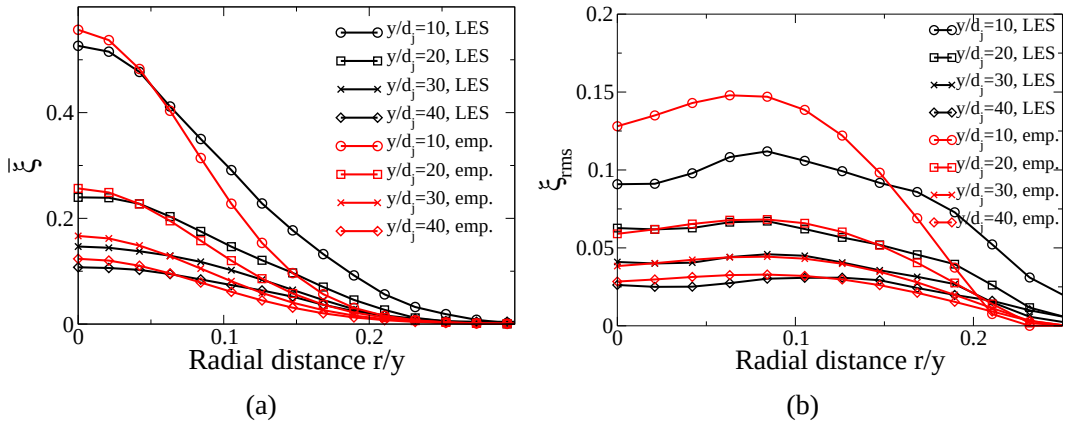

Figure 3.7: Radial profiles of a) mean and b) RMS of mixture fraction.

The comparison of the results from the LES of an inert jet with experimental and empirical data show that PRECISE can predict the velocity and mixing field in this simple jet with reasonable accuracy. The lack of realistic turbulent conditions in the

inlet plane causes some inaccuracies, but in the self-similar region the agreement of both the mean and the fluctuations of the velocity and mixing field with the available data is excellent. This simple validation exercise proves that for simple shear flows, PRECISE may be considered to be reliable.

3.3 The CMC solver

The code that solves the transport equations for the conditional averages of species and enthalpy has been developed in the Hopkinson Laboratory, Department of Engineering, University of Cambridge. It has been used in two-dimensional studies of a lifted [54] and an opposed flame [56], but also in auto-ignition problems [46, 111], as well as in diesel engine simulations [48]. Some improvements to the discretisation schemes are presented here, together with a description of operational parameters for the coupled LES/CMC code.

3.3.1 Discretisation schemes

The computational domain consists of a three-dimensional structured grid in physical space and a one-dimensional grid in η-space. It is noted that the CMC equation is a five-dimensional PDE in physical space, time and mixture fraction space (η-space). The CMC transport equations (Eq. (2.28) and (2.30)) have been discretised using a finite difference approach. The diffusion terms (both in physical and mixture fraction space) are discretised using a second-order accurate central difference scheme.

For the discretisation of the convection term, two different schemes are considered: a first-order upwind scheme and a second-order accurate total variation diminishing (TVD) scheme [112]. These schemes are well known and well documented (for example [113]) and therefore do not need to be reproduced here. They are, however, included in Appendix B for the reader's convenience.

In order to assess the accuracy and stability of these schemes, a numerical test was performed. A one-dimensional problem was considered where a hypothetical scalar y follows the distribution shown in figure 3.8. A pure convection process, without physical diffusion, was applied to this profile with a positive velocity $u = 5\,\mathrm{m/s}$. The x-direction is discretised using 1000 nodes and the spacing is kept constant and equal to $\delta x = 0.002\,\mathrm{m}$. The choice of timestep will specify the CFL number. Since there is no diffusion in this problem, the shape of the initial condition should not change and any smoothing of the profile will be the result of numerical diffusion.

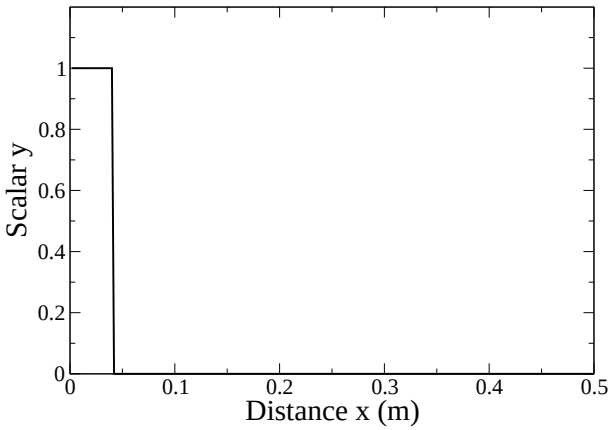

Figure 3.8: Initial condition for the numerical test.

The resulting profiles after 0.3 s using the two different schemes for three CFL numbers are shown in Fig. 3.9. The results do not appear to be sensitive to the CFL number. Due to its low order of accuracy, the first order upwind scheme always introduces relatively large amounts of numerical diffusion. This, however, makes it very stable. The TVD scheme considered here performs very well since it keeps the profile bounded at its original values and introduces only a small amount of numerical diffusion, compared to the first order upwind scheme. This accuracy, however, comes at a high computational cost. Due to its nature, an implicit implementation of the scheme leads to a set of non-linear equations which would have to solved at every timestep [114]. This is shown in Fig. 3.10, where the CPU time per timestep is shown for the two discretisation schemes. The time increases with

the CFL number because the timestep becomes larger. For small CFL numbers the TVD scheme is approximately 5 times more expensive than the first-order upwind scheme, while for higher CFL numbers (that are closer to the CFL numbers in the LES presented in this thesis) it is approximately 50 times more expensive. In the simulations presented in this thesis, the first-order upwind scheme has been used, unless stated otherwise, due to its low computational cost and lack of over-shoots and under-shoots. A comparison between simulations using this simple scheme and the TVD scheme will be presented in chapter 4.

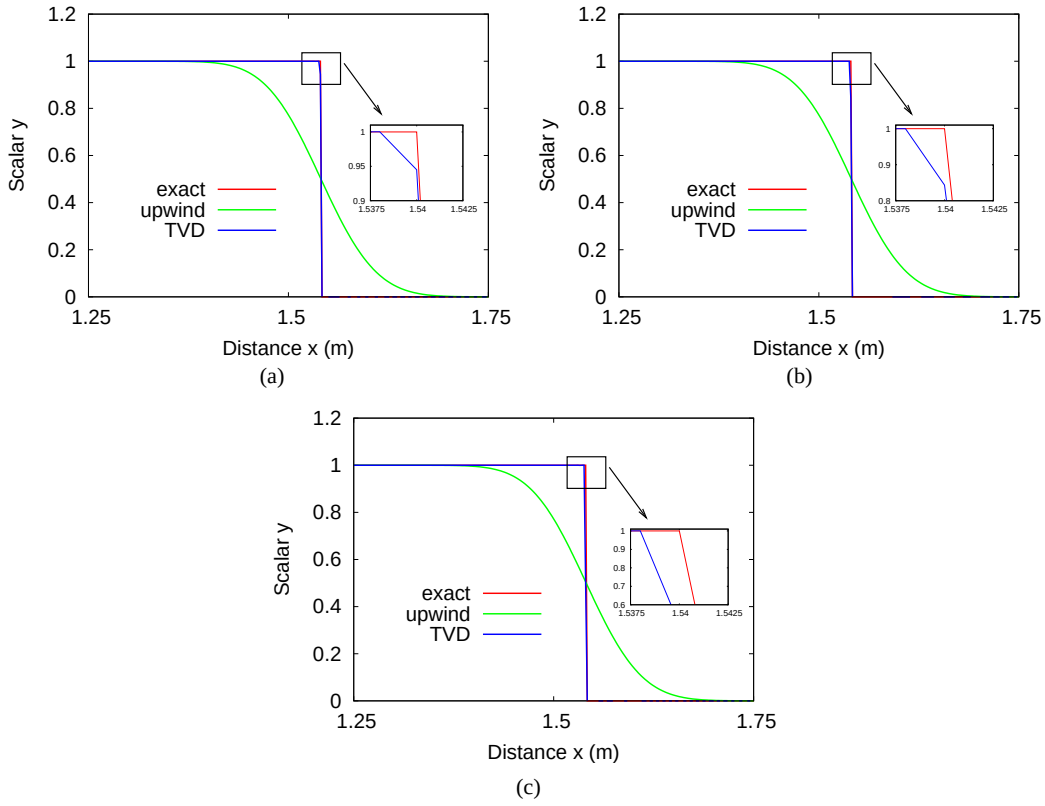

Figure 3.9: Comparison of the first-order upwind and TVD schemes, a) $CFL = 0.025$, b) $CFL = 0.05$, c) $CFL = 0.5$.

p

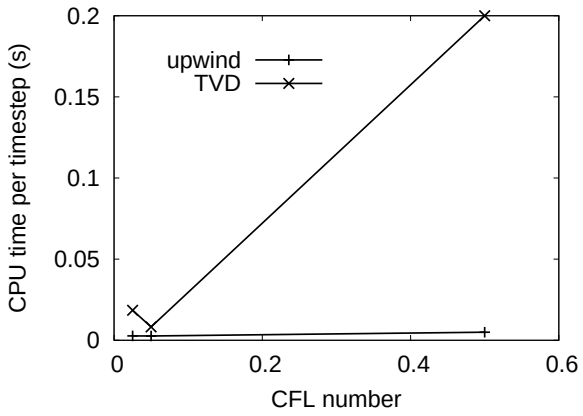

Figure 3.10: Required CPU time per timestep for the first-order upwind and TVD schemes.

3.3.2 Time integration

The possibility of using complex chemical mechanisms leads to the increase of the number of ODEs that have to be solved simultaneously, but it also introduces stiffness to the system. This is due to the fact that the time-scale associated with different species may span several orders of magnitude. Because of the stiffness, an ODE solver with adaptive timestep is used to perform the time-integration VODPK. VODPK [115–117] is based on a linear multi-step method using the backward differentiation formula. It is implicit with good stability properties and can be used for stiff and non-stiff problems with large numbers of ODEs [118].

The fact that the CMC equation is a five-dimensional equation, leads to very large number of ODEs that have to solved simultaneously. To reduce this number, and thus to reduce the computational load, an Operator Splitting (OS) method is used for the time integration of the CMC equation. In the OS method applied throughout this thesis, the CMC equation is solved in three steps:

- Step 1: Solve transport in physical space (terms T1 and T4 in Eq. (2.28)):

$$\frac{\partial Q_\alpha}{\partial t} = -\widetilde{u_i|\eta}\frac{\partial Q_\alpha}{\partial x_i} + \frac{1}{\overline{\rho}\,\widetilde{\mathcal{P}}(\eta)}\frac{\partial}{\partial x_i}\left[\overline{\rho}\widetilde{\mathcal{P}}(\eta)\, D_t \frac{\partial Q_\alpha}{\partial x_i}\right] \qquad t \in [t_0, t_0 + \Delta t_{CMC}] \tag{3.4}$$

  where t_0 is the time at the start of the CMC timestep and Δt_{CMC} is the CMC timestep. Eq. (3.4), after it has been discretised, is solved by the solver VODPK operated in non-stiff mode for every scalar α and for every node in mixture fraction space using the method of lines.

- Step 2: Solve transport in mixture fraction space (term T2 in Eq. (2.28)):

$$\frac{\partial Q_\alpha}{\partial t} = \widetilde{N|\eta}\frac{\partial^2 Q_\alpha}{\partial \eta^2} \qquad t \in [t_0, t_0 + \Delta t_{CMC}] \tag{3.5}$$

  Eq. (3.5) is solved for every scalar α and for every node in physical space by the solver VODPK operated in non-stiff mode.

- Step 3: Solve chemical source term (term T3 in Eq. (2.28)):

$$\frac{\partial Q_\alpha}{\partial t} = \widetilde{\omega_\alpha|\eta} \qquad t \in [t_0, t_0 + \Delta t_{CMC}] \tag{3.6}$$

  Eq. (3.6) is solved for every node in physical and mixture fraction space by the solver VODPK operated in stiff mode.

The estimated local error in Q_α is

$$ERR_\alpha = RTOL \times abs(Q_\alpha) + ATOL \tag{3.7}$$

where $RTOL$ is the relative tolerance and $ATOL$ is the absolute tolerance. These tolerances are parameters that are explicitly defined by the user before the computation begins (as an input to VODPK). Throughout this thesis the tolerances have

been kept constant (they remain the same for every fractional step):

$$RTOL = 10^{-6} \tag{3.8}$$

$$ATOL = 10^{-14} \qquad \text{(species)} \tag{3.9}$$

$$ATOL = 10^{-6} \qquad \text{(enthalpy)} \tag{3.10}$$

These values have proven to be sufficient both in terms of stability and accuracy [118].

In every step the Q_α used are the latest available. For example the Q_α used in step 2 are the ones after step 1 has been performed. The use of the OS method introduces an error because phenomena that are coupled in nature are solved sequentially. This error could be bigger for species with small time-scales [48] and it will decrease as the timestep becomes smaller. More details about the procedure of the splitting and the errors associated with it can be found in Ref. [48, 118]. A typical Δt_{CMC} used in this work is equal to 2×10^{-6} s.

3.3.3 Parallelisation

Because of the large number of ODEs that have to be resolved, the use of a single workstation is not possible. The CMC equation must be solved in parallel on several machines. The parallelisation method depends on the step in the OS method. In the first step (transport in space, terms T1 and T4 in Eq. (2.28)), the nodes in η-space are distributed among the processors. At the end of the step, all the information is collected and broadcasted, so that all the processors have access to the most updated solution. In the next two steps (micromixing and chemical reaction, terms T2 and T3, respectively), the cells in physical space are distributed among the processors. At the end of each step, the information is again collected and broadcasted to all the processors. This straightforward method of distributing the computational load has the benefit of being very simple to implement and does not require communication between the processors during the time-integration, which would be time-consuming.

3.3.4 Spark representation and boundary conditions

The spark is considered to be a region of hot combustion gases; at a time instant (considered to be $t = 0$ for the ignition simulations) it is assumed that in a location in the flow, the distribution of Q_α corresponds to a fully burning condition (see Figs 3.12 to 3.15). This location is considered to be the spark location. In all the other CMC cells, a 'frozen' Q_α distribution is imposed initially (room temperature, no combustion products and straight lines for fuel, O_2 and N_2). This spark representation will induce ignition by spatial convection and diffusion of heat and radicals from the CMC cells with a burning Q_α distribution to the neighbouring CMC cells that have a 'frozen' Q_α distribution. The size of the spark was similar to the size of the flame kernel observed experimentally ($3-4$ mm) at the end of the energy deposition process; this lasted 0.5 ms in the experiment, which is very short compared to the subsequent overall flame ignition process that lasted tens of milliseconds. Representations in terms of a source term in the energy equation [83] but also in terms of hot jets [27] have also been used in LES of ignition. In this work, however, emphasis is given to the flame expansion process and the deposition of energy and initial kernel growth are not considered.

Since the CMC equation is a five-dimensional equation, initial and boundary conditions must be provided. At the walls, adiabatic boundary conditions are used. This formulation does not allow quenching of the flame at the walls. At the inlet of the CMC domain, a 'frozen' Q_α distribution is imposed, while at the exit, a zero-gradient boundary condition is used. In η-space, a Dirichlet boundary condition is used at $\eta = 0$ and $\eta = 1$ and the values of Q_α and Q_h remain there unchanged.

3.4 Chemical mechanisms

In the simulations presented in this work, two mechanisms of different complexity for methane were used. The first is a global single-step mechanism, developed re-

cently for non-premixed and partially premixed methane combustion [7], where the activation temperature T_a and the heat release rate q are functions of the equivalence ratio ϕ. By expressing the heat release and the activation energy as functions of the equivalence ratio, the model is able to reproduce the correct premixed flame speeds for the entire range of flammable mixtures [7].

Secondly, a detailed chemical mechanism for methane consisting of 16 species and 25 reactions is used [8]. This mechanism has been used in simulations of turbulent non-premixed methane jet flames [119]. This mechanism is simpler than the full methane oxidation mechanism and it is expected to provide accurate results for lean to stoichiometric flames, in terms of adiabatic flame temperatures and laminar flame speeds [8]. However, the lack of C_2-hydrocarbons may lead to errors in regions of rich combustion.

To further validate the accuracy of the mechanisms, zero-dimensional CMC (0D-CMC) calculations of a non-premixed and a partially premixed flame are performed using the single step chemistry model and the afore-mentioned 16-species mechanism. The predictions are compared to results with the detailed GRI-Mech 3.0 chemistry mechanism, consisting of 53 species and 325 chemical reactions [9]. In the 0D-CMC calculations, only the micromixing and chemical reaction terms are considered:

$$\frac{\partial Q_\alpha}{\partial t} = N|\eta \frac{\partial^2 Q_\alpha}{\partial \eta^2} + \omega_\alpha|\eta \tag{3.11}$$

The AMC model is used for the conditional scalar dissipation rate (Eq. (2.39), where N_0 is kept at a prescribed value). At the limit where heat is diffused more quickly than it is produced, the flame is considered to have been extinguished. Eq. (3.11) is a one-dimensional equation in η-space. Dirichlet boundary conditions are used at $\eta = 0$ and $\eta = 1$. The grid consists of 51 nodes, clustered around stoichiometric mixture fraction. Eq. (3.11) is solved as an unsteady equation which eventually converges to a steady solution. The timestep used is kept constant at $\delta t = 10^{-5}$ s. Two flames are considered here. First, the purely non-premixed case (a

Table 3.1: Flames used in this thesis. Pressure $p = 1$ bar throughout.

		Flame A (used in chapter 5)	Flame B (used in chapter 4)
$\xi = 0$	Y_{CH_4}	0	0
(Air	Y_{O_2}	0.233	0.233
Stream)	Y_{N_2}	0.767	0.767
	T	300 K	300 K
$\xi = 1$	Y_{CH_4}	1	0.1218
(Fuel	Y_{O_2}	0	0.2046
Stream)	Y_{N_2}	0	0.6736
	T	300 K	300 K

non-premixed flame will be discussed in chapter 5) and secondly a partially premixed flame with 80% by volume air (one such flame will be discussed in chapter 4). The details about these flames are summarised in Table 3.1.

The maximum temperature of the flame for different values of N_0 for both the non-premixed and the partially premixed case is shown in Fig. 3.11, while the values of the extinction scalar dissipation rate are shown in Table 3.2. The results from the 16-species mechanism are similar to the results using the GRI mechanism for both cases. The difference in maximum temperature of the flame does not exceed 20 K and the difference in the extinction scalar dissipation rate is very small (less than 2% for flame A and approximately 3% in flame B). The global single-step mechanism over-predicts the maximum temperature of the non-premixed flame by approximately 100 K and the extinction scalar dissipation rate by about 25%. In the case of the partially premixed flame, it over-predicts the temperature by approximately 250 K and the extinction scalar dissipation rate by approximately a factor of two. The single-step chemistry model does not take into account the effect of dissociation, which may reduce the temperature, and therefore requires higher rates of dissipation for extinction.

Profiles of the temperature for the three mechanisms for both flames for a value

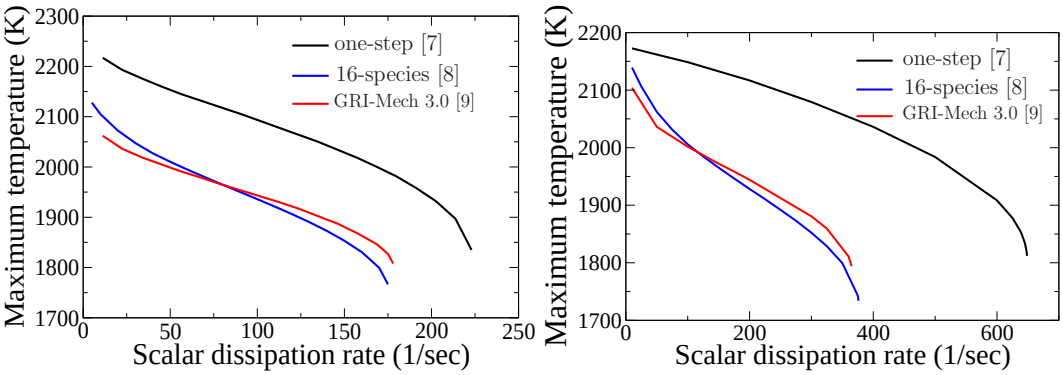

(a) Flame A (b) Flame B

Figure 3.11: Maximum temperature of the steady flame for different values of N_0 (see Eq. (2.39)), using three different chemical mechanisms.

Table 3.2: Extinction scalar dissipation rate (N_0 in Eq. (2.39)) [1/s] for the three chemical mechanisms for flames A and B.

	Flame A	Flame B
GRI-Mech 3.0 [9]	178	365
16-species [8]	175	376
One-step [7]	223	648.5

of N_0 equal to half the extinction value are shown in Fig. 3.12. For flame A, the 16-species mechanism and GRI-Mech 3.0 give almost identical results, while the single-step mechanism over-predicts the temperature by about 50 K. For flame B, both the single-step and the 16-species mechanisms over-predict the temperature by about 100K.

In order to gain more insight into the structure of the flames, the profiles of several species are plotted for all the mechanisms, again for half the extinction scalar dissipation rate. The mass fractions of CH_4 and O_2 are shown in Fig. 3.13, of H_2O and CO_2 are shown in Fig. 3.14 and of OH and CH_2O are shown in Fig. 3.15. For flame A, the single-step chemistry over-predicts the consumption of fuel, resulting to higher levels of CO_2 and H_2O. This is consistent with Fig. 3.12 where

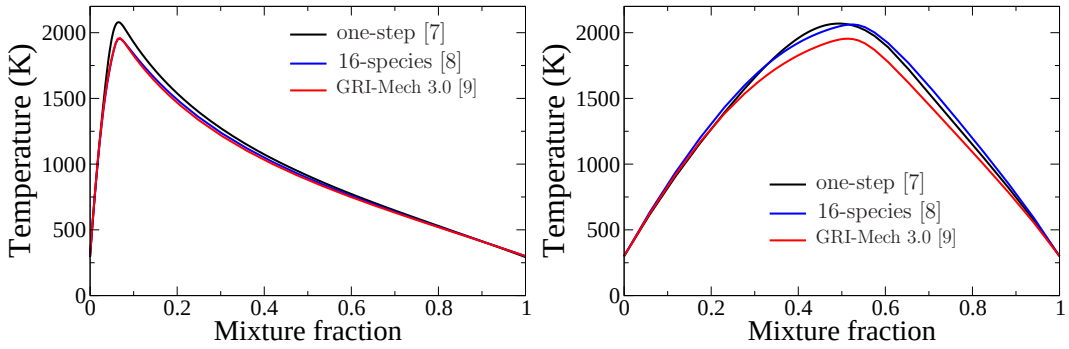

Figure 3.12: Profiles of conditional temperature for N_0 equal to one half of the corresponding extinction value. a) Non-premixed flame; b) partially premixed flame (80% volume air).

the temperature is over-predicted (due to the over-prediction of the fuel consumption and hence the release of heat, the temperature is over-predicted). The 16-species mechanism is in very good agreement with GRI-Mech 3.0 for all major species (Figs 3.13a and 3.14a). There is also very good agreement in the levels of OH, but there is significant discrepancy in the levels of CH_2O. For flame B, the predictions from the single-step chemistry become poorer, but the trends are the same as in the non-premixed flame. The predictions from the 16-species mechanism are not as good as in flame A. There are significant differences compared with the GRI mechanism in the levels of H_2O and CO_2 and despite the fact that OH is predicted accurately, the inaccuracy in the levels of CH_2O remains. This may be attributed to the lack of C_2-hydrocarbons in the 16-species mechanism, which would appear in the regions of rich combustion.

The conclusion from this investigation is that the 16-species mechanism can predict with reasonable accuracy the extinction scalar dissipation rate and the profiles in η-space of temperature and the main reactants and products, especially in the case of the purely non-premixed flame. The lack of C_2-hydrocarbons, however, causes some inaccuracies in regions of rich combustion. The single-step mechanism predicts

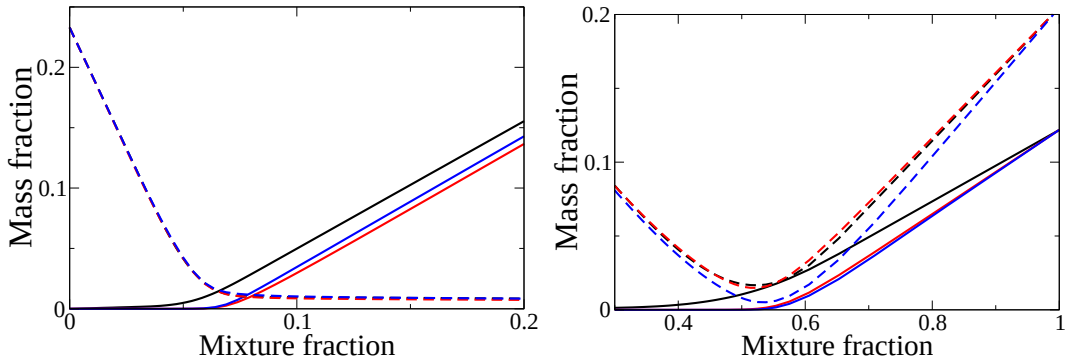

(a) Flame A (b) Flame B

Figure 3.13: Profiles of Y_{CH_4} (solid lines) and Y_{O_2} (dashed lines) for N_0 equal to one half of the corresponding extinction value. Black lines: single step chemistry [7], blue lines: 16-species chemistry [8], red lines: GRI-Mech 3.0 [9].

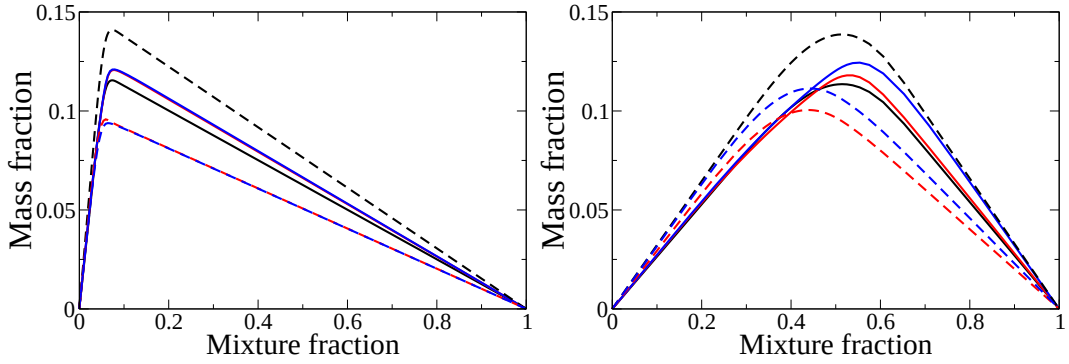

(a) Flame A (b) Flame B

Figure 3.14: Profiles of Y_{H_2O} (solid lines) and Y_{CO_2} (dashed lines) for N_0 equal to one half of the corresponding extinction value. Black lines: single step chemistry [7], blue lines: 16-species chemistry [8], red lines: GRI-Mech 3.0 [9].

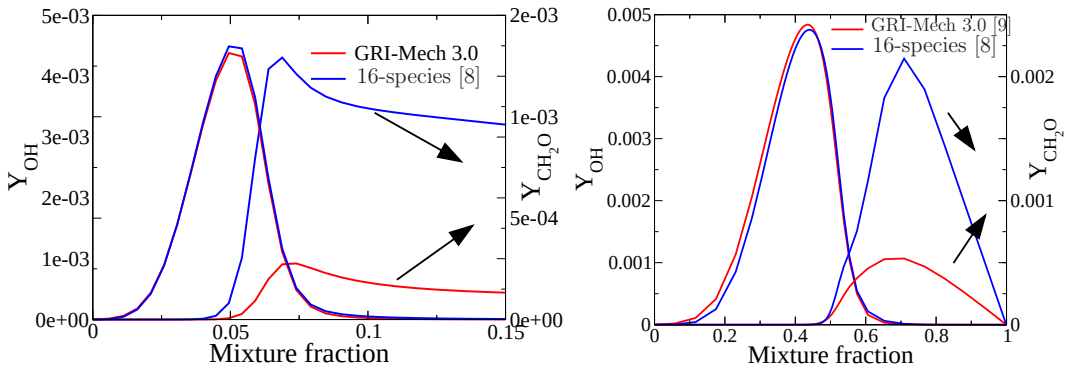

(a) Flame A (b) Flame B

Figure 3.15: Profiles of Y_{OH} and Y_{CH_2O} for N_0 equal to one half of the corresponding extinction value. Blue lines: 16-species chemistry [8], red lines: GRI-Mech 3.0 [9].

the trends reasonably well, but it overpredicts both the flame temperature and the extinction scalar dissipation rate. This over-prediction is more pronounced in the case of the partially premixed flame.

3.5 Conclusions

The numerical codes used in this thesis have been presented in this chapter. The CFD solver PRECISE has been validated for a simple free shear flow (a turbulent jet) and it was found that good agreement with empirical laws and experimental data was achieved.

The numerical code that solves the CMC equation has also been presented. Due to the size and the stiffness of the system of ODEs that needs to be solved, an Operator Splitting (OS) procedure was used. The OS consists of the sequential integration of the different terms of the equation. First transport in physical space is integrated, then transport in mixture fraction space and finally the chemical source term. This reduces the requirement in memory usage, thus reducing computational time. It does, however, introduce a numerical error as phenomena that are coupled in nature are solved sequentially. This error depends on the timestep of the simulation. The

splitting method allows for very simple and straightforward parallelisation of the code. In the first step (transport in space) the nodes in mixture fraction space are distributed among the processors, while in the second and third step (transport in mixture fraction space and chemistry, respectively), the cells in physical space are divided among the processors. At the end of every step the information for all the processors are gathered and broadcasted so that each processor 'sees' the most up to date arrays. Results using this code are presented in chapters 4 and 5.

Both codes are fully parallelised for higher efficiency in terms of computational time. The spark is represented as a region of hot combustion gases and ignition will be induced by transport of heat and species to the initially inert neighbouring locations. Comparison of a single step chemical mechanism and a detailed 16-species/25 reactions mechanism with a detailed 53 species/325 reactions showed that the flame temperature, extinction scalar dissipation rate and major species mass fractions were predicted accurately by the 16-species mechanism. The lack of C_2-hydrocarbons, however, caused some discrepancies in some minor species mass fractions, especially in regions of rich combustion. With the single step mechanism, the temperature of the flame was overpredicted by approximately 100 K and the extinction scalar dissipation rate by almost a factor of two.

Chapter 4

Ignition of a Shearless Mixing Layer

4.1 Introduction

The purpose of this chapter is to investigate numerically the ignition process in a simple geometry by performing LES/CMC calculations. The geometry consists of two turbulent streams (one carrying fuel and one carrying air) which form a mixing layer. The two streams enter the burner at the same velocity and hence there is no shear. The mixture fraction will take values from zero to one moving through the mixing layer. The simplicity of this configuration makes it a good platform to test and evaluate the importance of different parameters in the solution. Such parameters are the resolution of the CMC mesh, the discretisation of the convective scheme and the effect of turbulent diffusion. There is availability of experimental data which will help to assess the accuracy of both the inert flow simulations and the flame expansion process.

4.2 Configuration

A schematic of the burner is shown in Fig. 4.1. It consists of two rectangular channels of width $W = 46\,\text{mm}$ and height $H = 20.5\,\text{mm}$. The two channels are attached and their common wall has a slope of 2.5 degrees, resulting in what is essentially a splitter plate separating them. At the exit of the channels the plate has a thickness of 0.3 mm. The length of the burner is $L = 112\,\text{mm}$. To generate turbulence, perforated plates were placed 50 mm upstream of the exit of the channels. One stream carries air, while the other carries methane mixed with 80% by volume air. Both streams enter the burner at room temperature and pressure. For this air premixedness, the stoichiometric mixture fraction is $\xi_{st} = 0.452$, while the lean and rich flammability limits are $\xi_{lean} = 0.233$ and $\xi_{rich} = 0.732$, respectively [10].

In the experiments [10], an electric spark was placed at $(x, y, z) = (40, 0, 0)$ (see Fig. 4.1 for definition of x, y, z). Due to the high streamwise velocity, the flame did not anchor at the splitter plate, but was convected away. By fast cinematography, the flame edge in the streamwise (x) and spanwise (z) directions was measured as a function of time. This can serve as a validation test case for LES/CMC, in the context of examining if flame growth in mixing layers can be captured.

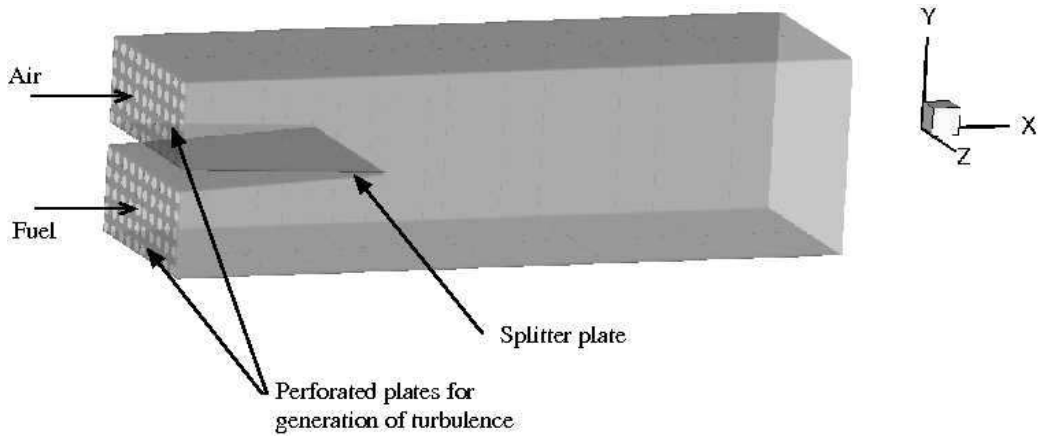

Figure 4.1: Schematic of the mixing layer burner, showing the inlet of air and fuel, the splitter plate between them and the turbulence-generating perforated plates.

4.3 Computational mesh and boundary conditions

The computational domain extends 50 mm upstream of the end of the splitter plate. It covers the entire length of the burner and extends 25 mm downstream of the end of the channels. In the y and z directions, it covers the whole width and height of the burner. All the distances in the streamwise direction are measured from the end of the splitter plate ($x = 0$ at this location). The $y = 0$ plane is located at the splitter plate, while the $z = 0$ plane is located at the centre of the channel. In the main condition investigated here, the bulk streamwise velocity is equal to $u_b = 3\,\mathrm{m/s}$. Another condition was also investigated where $u_b = 8\,\mathrm{m/s}$. During the analysis of the data, it will be assumed that $u_b = 3\,\mathrm{m/s}$, unless stated otherwise. A characteristic 'flow-through' time can be defined as $\tau_f = L/u_b = 37.3\,\mathrm{ms}$.

The computational mesh, shown in Fig. 4.2, consists of approximately 680k cells, with 60 cells along the y and z directions and approximately 180 cells in the x direction, 70 of which are between the grid-generating plates and the end of the splitter plate. The distribution in the y and z directions is uniform, while in the x direction it has been refined at the end of the splitter plate to capture the initial mixing of the two streams.

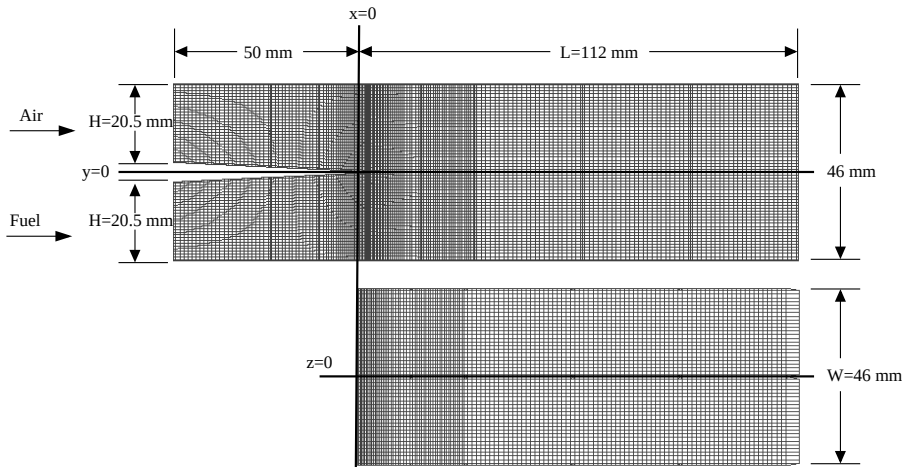

Figure 4.2: Computational mesh on $z = 0$ (top) and $y = 0$ (bottom) planes.

In order to generate turbulence in the two channel flows, the flow through a perforated plate was simulated. This is identical to the turbulence-generating method in the experiment. This method has been used in LES in the past, predicting reasonably accurate velocity fields [86]. The time series of the streamwise velocity for a window in time ($t = 0$ here corresponds to an arbitrary time) at $x = 0$, $y = 12.5\,\mathrm{mm}$, $z = 0$, which is located at the exit plane of one of the channels (in the air stream) is shown in Fig. 4.3a.

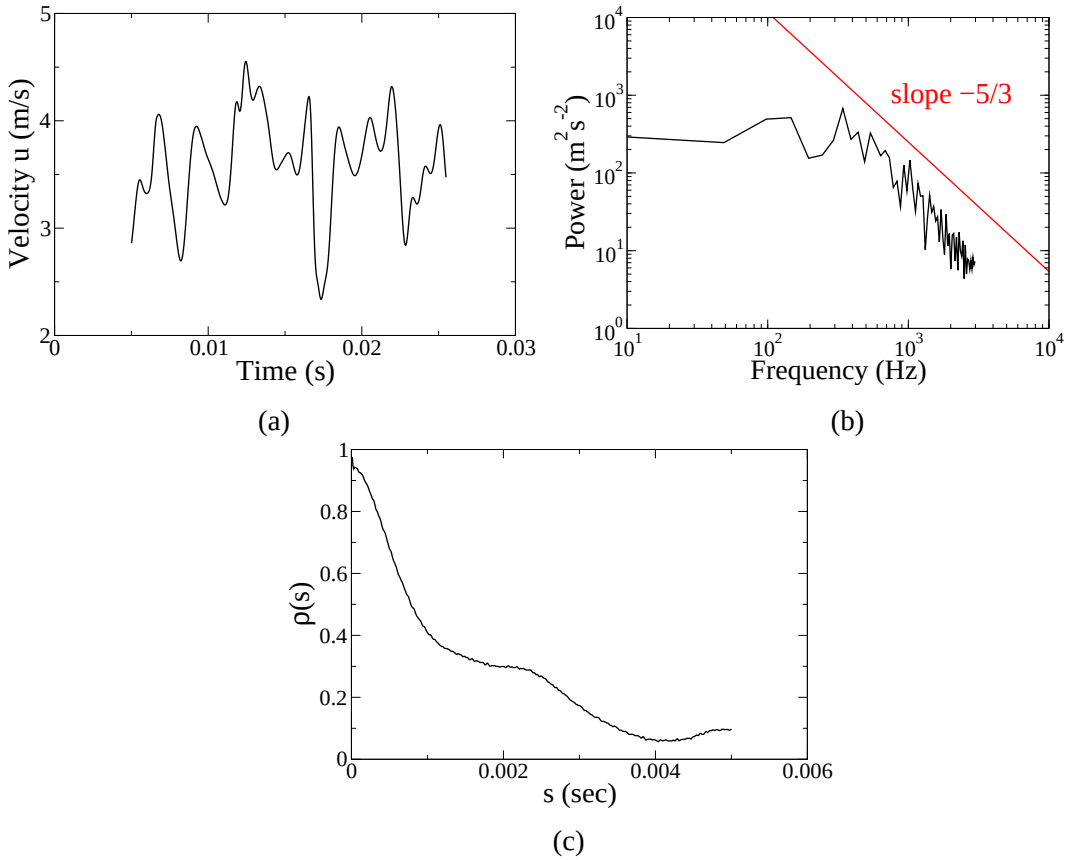

Figure 4.3: a) Time series of the streamwise velocity u ($t = 0$ here corresponds to an arbitrary time), b) the corresponding energy spectrum of the fluctuations and c) the corresponding autocorrelation function.

The presence of fluctuations around the time-averaged velocity is evident from Fig. 4.3a. In order to establish whether the u velocity field resembles a turbulent

field, its power spectrum was calculated and the slope was compared to the well-known value of $-5/3$ which corresponds to the inertial subrange, Fig. 4.3b. Taking into account that the sample used here is small (there are 2048 data points in a 2 ms time interval) and that the Reynolds number is small ($\mathrm{Re} = \mathrm{u_b} \times \mathrm{W}/\nu = 4070$ and $\mathrm{Re_t} \approx 153$ from the experiment), the agreement with the $-5/3$ slope can be considered to be reasonable, which suggests that the velocity field predicted from the LES does indeed resemble a turbulent flow field. The autocorrelation function $\rho(s)$ is shown in Fig. 4.3c, where $\rho(s)$ is:

$$\rho(s) = \frac{\langle u'(t)u'(t+s)\rangle}{\langle u'(t)^2\rangle} \tag{4.1}$$

where $\langle u\rangle$ is the time-averaged streamwise velocity and $u'(t) = u(t) - \langle u\rangle$ is the fluctuation. The brackets $\langle\rangle$ denote time-averaging. As it is expected, for small values of s, $\rho(s) \approx 1$, while for larger values of s, $\rho(s) \approx 0$. The fact that $\rho(s)$ does not decrease smoothly from 1 to 0 may be attributed to the small sample of the time series which is used for its calculation. The integral

$$\tau = \int_0^\infty \rho(s)\, ds \tag{4.2}$$

returns the integral time-scale [28], which in this case is $\tau = 1.45$ ms. Making the Taylor assumption, an integral lengthscale may be calculated as

$$\mathcal{L} = \tau\langle u\rangle \tag{4.3}$$

which returns a value of $\mathcal{L} = 4.35$ mm. In the experimental study, it was reported that at $x = 3$ mm, the integral lengthscale was approximately 3 mm, which means that $\mathcal{L}$ is slightly over-predicted by the LES. Nevertheless, the presence of autocorrelation and its shape (Fig. 4.3c) and the accurate prediction of the $-5/3$ slope confirms that the turbulence generation method is reasonably accurate.

The mesh in η-space consists of 51 cells, clustered around the stoichiometric mixture fraction ($\xi_{st} = 0.452$). Details about the spark representation and the boundary conditions for the CMC equations can be found in section 3.3.4. The

spark size was in all cases $1.5 \times 3 \times 3\,\text{mm}$ and it was located at $x = 40\,\text{mm}$, $y = 0$, $z = 0$.

4.4 Inert flow

4.4.1 Velocity

Instantaneous and time averaged contours of the streamwise velocity u across the $z = 0$ plane are shown in Fig. 4.4. The high velocity jets in the grid-generating perforated plate break up and mix before the end of the splitter plate causing the velocity in the burner to be relatively uniform. This is more clearly shown in the instantaneous contour.

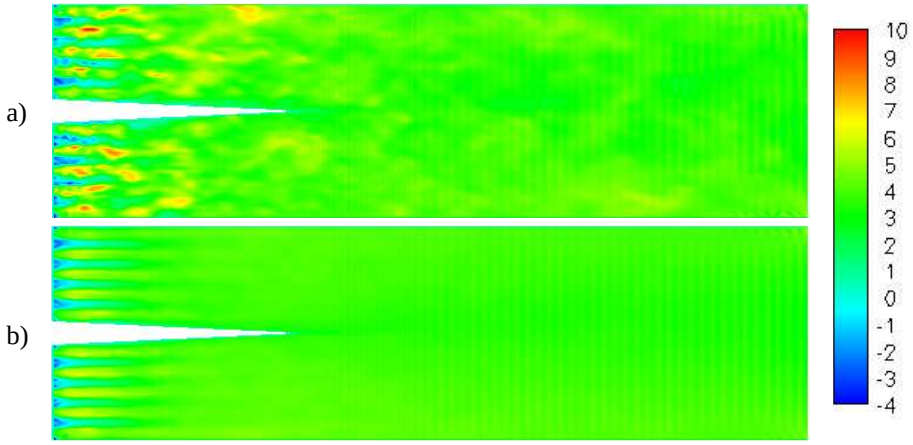

Figure 4.4: a) Instantaneous and b) time averaged contours of the streamwise velocity u [m/s].

Profiles of the time-averaged streamwise velocity u and the RMS of its fluctuations along the transverse direction for different spanwise and streamwise positions, compared with hot-wire measurements [10] are shown in Fig. 4.5. The averages were composed over a simulated time of 160 ms which corresponds to 4.3 flow-through times and 110 integral timescales ($\tau = 1.45\,\text{ms}$), which allows for sufficient statistical

convergence.

In the location nearest to the splitter plate ($x = 3\,\text{mm}$), a thin wake appears (dip in the mean velocity profile). Further along the x direction, the profiles becomes more uniform both in the y and in the z direction. The velocity field predicted by the LES exhibits a small non-uniformity in the y direction, which does not appear in the experimental data. This may be due to the fact that there is not enough resolution near the walls to resolve the boundary layer and this may have an effect in the velocity field towards the centre of the flow. Moreover, the LES predicts a 'shorter' wake; for $x = 43\,\text{mm}$ the wake seems to have disappeared in the LES but it still exists in the experimental measurements. The RMS of the streamwise velocity u_{RMS} is predicted reasonably well. The decay of the fluctuations ($u_{RMS} \approx 0.6\,\text{m/s}$ at $x = 3\,\text{mm}$ decays to $u_{RMS} \approx 0.2\,\text{m/s}$ at $x = 83\,\text{mm}$) and the uniformity in the y and z directions are captured with reasonable accuracy.

4.4.2 Mixture fraction

Instantaneous and time averaged contours of the mixture fraction across the $z = 0$ plane are shown in Fig. 4.6. The mixing of the two streams (fuel at the bottom and air on the top) begins just after the splitter plate and is enhanced by turbulence. Large and small eddies that contribute to the mixing of the streams are clearly shown in Fig. 4.6a. The mixing layer grows sharply after the splitter plate for the first 60 mm, after which it grows at a more moderate rate.

Profiles of the time-averaged mixture fraction and the RMS of its fluctuations along the transverse direction for different spanwise and streamwise positions are shown in Fig. 4.7. These averages were composed over a simulated time of 440 ms which corresponds to 11.8 flow-through times and 303 integral timescales. The experimental data are plotted for $z = 0$. No experimental data are shown for $x < 43\,\text{mm}$ because the fact that the mixing layer is thin and that the spatial resolution of the sampling probe was approximately 2 mm [10] leads to large uncertainties

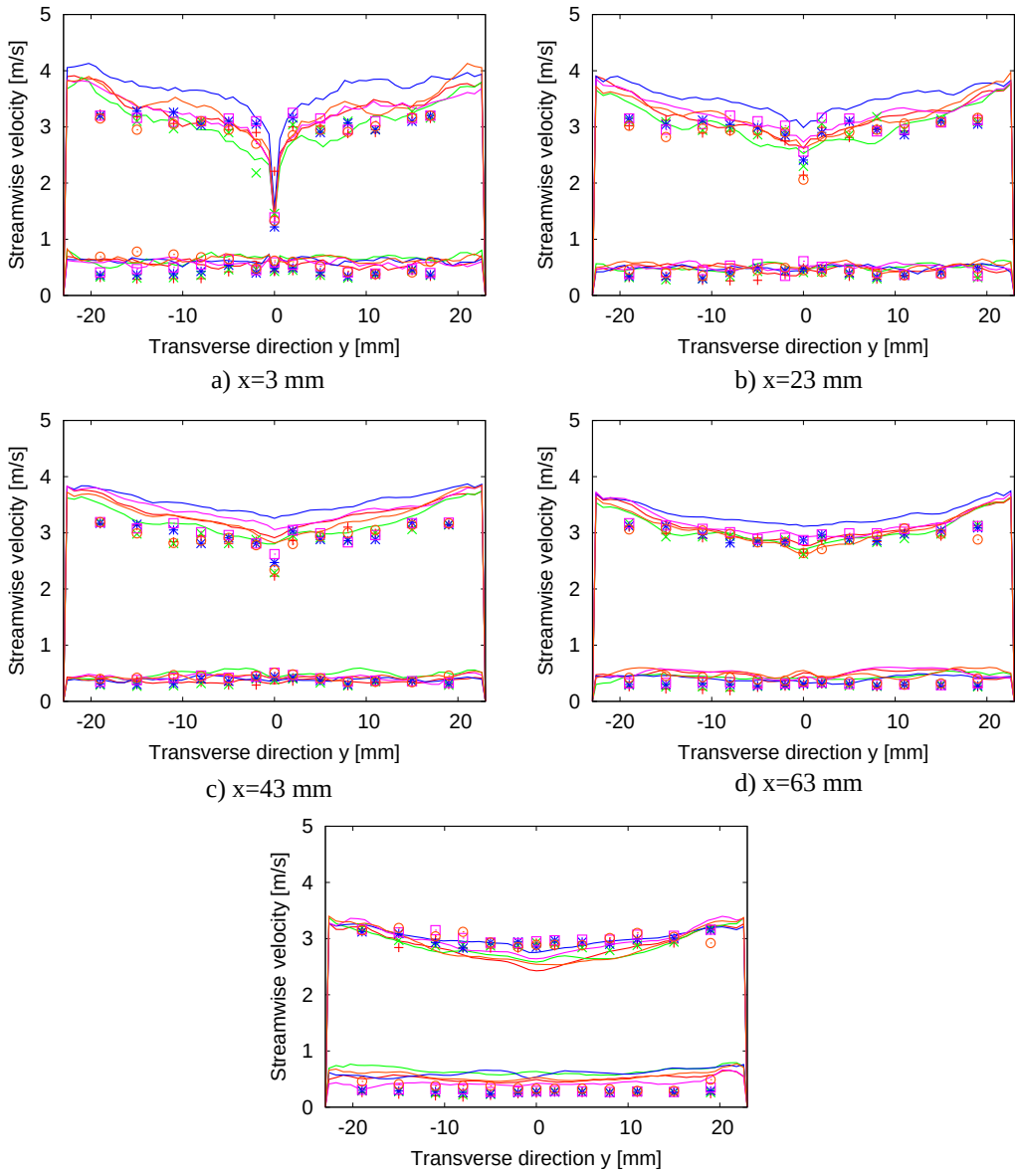

Figure 4.5: Mean streamwise velocity u and RMS of its fluctuations along the transverse direction y at different streamwise and spanwise locations. Lines: LES, symbols: experimental data [10]. Red lines and $+$: $z = -15\,\mathrm{mm}$, green lines and $\times$: $z = -5\,\mathrm{mm}$, blue lines and $*$: $z = 0$, magenta lines and $\boxdot$: $z = 5\,\mathrm{mm}$, orange lines and $\odot$: $z = 15\,\mathrm{mm}$.

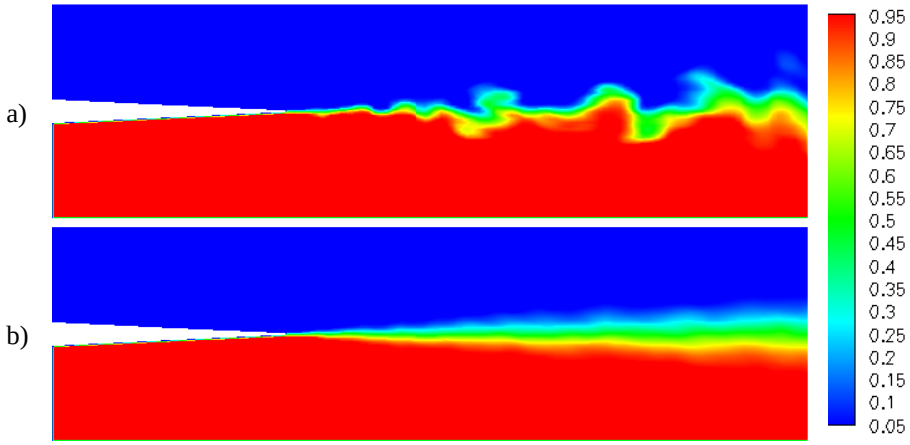

Figure 4.6: a) Instantaneous and b) time averaged contours of the mixture fraction field.

regarding the data. No experimental data for the RMS of the mixture fraction are available.

Near the splitter plate ($x = 3\,\text{mm}$), the gradient of ξ is very sharp and uniform in the z direction. Further along the streamwise direction, the two streams mix and the mixing layer becomes wider; the width of the mixing layer grows from approximately $10\,\text{mm}$ at $x = 23\,\text{mm}$ to $10\,\text{mm}$ at $x = 63\,\text{mm}$ and $20\,\text{mm}$ at $x = 83\,\text{mm}$. At the same time some non-uniformity appears in the z direction. The RMS of the mixture fraction follows the pattern of the width of the mixing layer. The narrow profile at $x = 3\,\text{mm}$ expands further down the x direction. Overall, the agreement with the available experimental data is very good.

4.5 Spark ignition

The ignition simulations are summarised in Table 4.1. The simulation parameters are different for each simulation. Different CMC mesh resolutions, bulk velocities and convection schemes are used. In addition, the influence of the term T4 in eq. (2.28) is investigated.

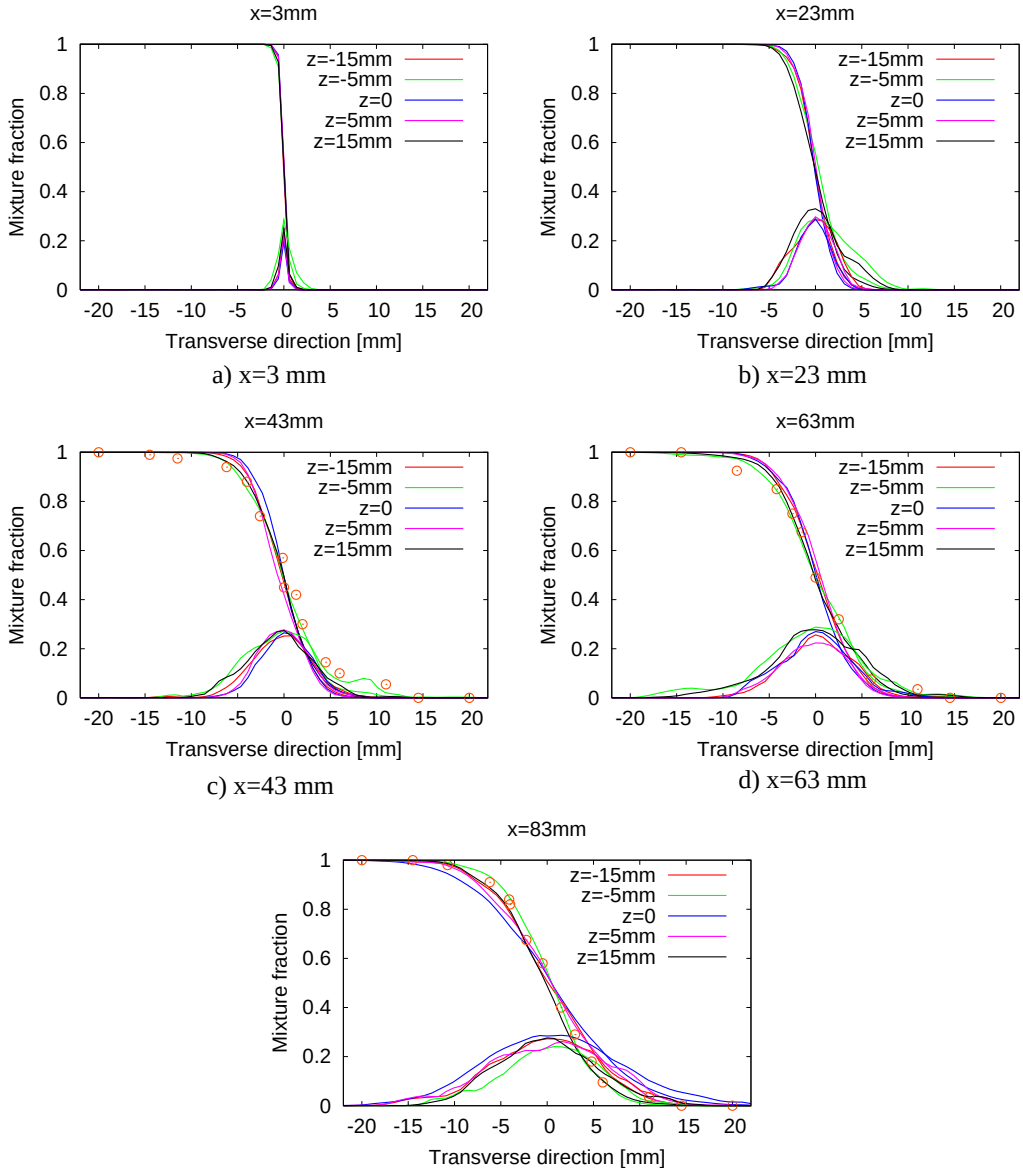

Figure 4.7: Mean mixture fraction and RMS of its fluctuations from the LES (solid lines) and the experiment (symbols, Ref. [10]) along the transverse direction y at different streamwise and spanwise locations. Red lines: $z = -15\,\mathrm{mm}$, green lines: $z = -5\,\mathrm{mm}$, blue lines: $z = 0$, magenta lines: $z = 5\,\mathrm{mm}$, black lines: $z = 15\,\mathrm{mm}$.

Table 4.1: Parameters of the ignition simulations.

Case	CMC Mesh size	Bulk velocity	Convection scheme	Term T4?	Chemical Mechanism
CS1	$29 \times 13 \times 35$	3 m/s	Upwind	Yes	Single step [7]
CS2	$29 \times 13 \times 35$	3 m/s	TVD	Yes	Single step [7]
FS1	$45 \times 35 \times 35$	3 m/s	Upwind	Yes	Single step [7]
FS2	$45 \times 35 \times 35$	3 m/s	Upwind	No	Single step [7]
FS3	$45 \times 35 \times 35$	8 m/s	Upwind	Yes	Single step [7]

As has already been mentioned, the spark in all cases was located at $x = 40\,\text{mm}$, $y = 0$, $z = 0$ and its size was $1.5 \times 3 \times 3\,\text{mm}$. The one-step mechanism (see also section 3.4) [7] has been used in all simulations. In cases CS1 and CS2 a relatively coarse CMC mesh was used (total of $13,195$, $29 \times 13 \times 35$, cells), but the convection scheme used was different (upwind and TVD, respectively). In cases FS1, FS2 and FS3 a finer CMC mesh is used ($55,125$, $45 \times 35 \times 35$, cells). The resolution of the mesh is the only difference between cases CS1 and FS1. In FS2, the term T4 in Eq. (2.28) (turbulent diffusion) has been omitted, while in case FS3 a higher bulk velocity is used ($u_b = 8\,\text{m/s}$).

4.5.1 Effect of mesh resolution

Cases CS1 and FS1 are compared in this section and the effect of the mesh resolution in the solution is investigated. A coarse CMC mesh is used in CS1 while a fine one is used in FS1 with the initial conditions being identical in both cases. Instantaneous isosurfaces of stoichiometric mixture fraction ($\xi_{st} = 0.452$), coloured by temperature, at different times from the moment of ignition for cases CS1 and FS1 are shown in Fig. 4.8 and 4.9, respectively. In both cases, the flame expands in the streamwise direction, driven by the bulk velocity. In case CS1, the flame does not expand significantly in the z direction, while in FS1 it does, under the effect of turbulent

diffusion and convection. Despite the fact that the mesh has not been refined in the z direction (35 cells were used in both cases), the refinement in the other directions has produced a more realistic solution.

The flame edge position as a function of time in the streamwise and spanwise directions, compared with experimental data is shown in Fig. 4.10. The experimental line is based on a linear curve fit, while the LES results are based on a temperature threshold; $\widetilde{T} = 1500\,\mathrm{K}$ was used to determine the location of the flame. In addition, the experimental curve is based on 50 separate ignition events, whereas the LES curve is based on a single calculation. The evolution of the location of the front branch of the flame is captured reasonably well by CS1 and very well by FS1. The front branch moves in the x direction under the effect of the streamwise velocity and the expansion of the hot gases, which causes an acceleration of the front branch of the flame. The current LES/CMC formulation is capable of predicting the correct flame speed both in the streamwise (where the flame expansion is assisted by the mean flow velocity) and in the spanwise direction (where the the mean flow velocity is zero). It is worth noting, however, that the expansion of the rear branch of the flame is not predicted well. In both CS1 and FS1, the flame remains 'anchored' at the spark location and does not move under the effect of the mean flow velocity. For the spanwise direction, the flame expansion in case CS1 is very different to the experimental data. The width of the flame does not change significantly with time and this behaviour is unrealistic. Case FS1 predicts a reasonable flame expansion. The rate of expansion (gradient of the curve) is reasonably well reproduced, but the width of the flame is slightly under-predicted. Qualitatively, the expansion pattern in the z direction is captured with reasonable accuracy.

When a condition with a lower bulk velocity (a velocity equal to half the bulk velocity here) was investigated experimentally, it was observed that the flame would indeed remain 'anchored' at the spark location for a considerable length of time and then expand upstream via the boundary layer which is formed in the wall. This kind of behaviour cannot be predicted here, because the LES resolution is not high

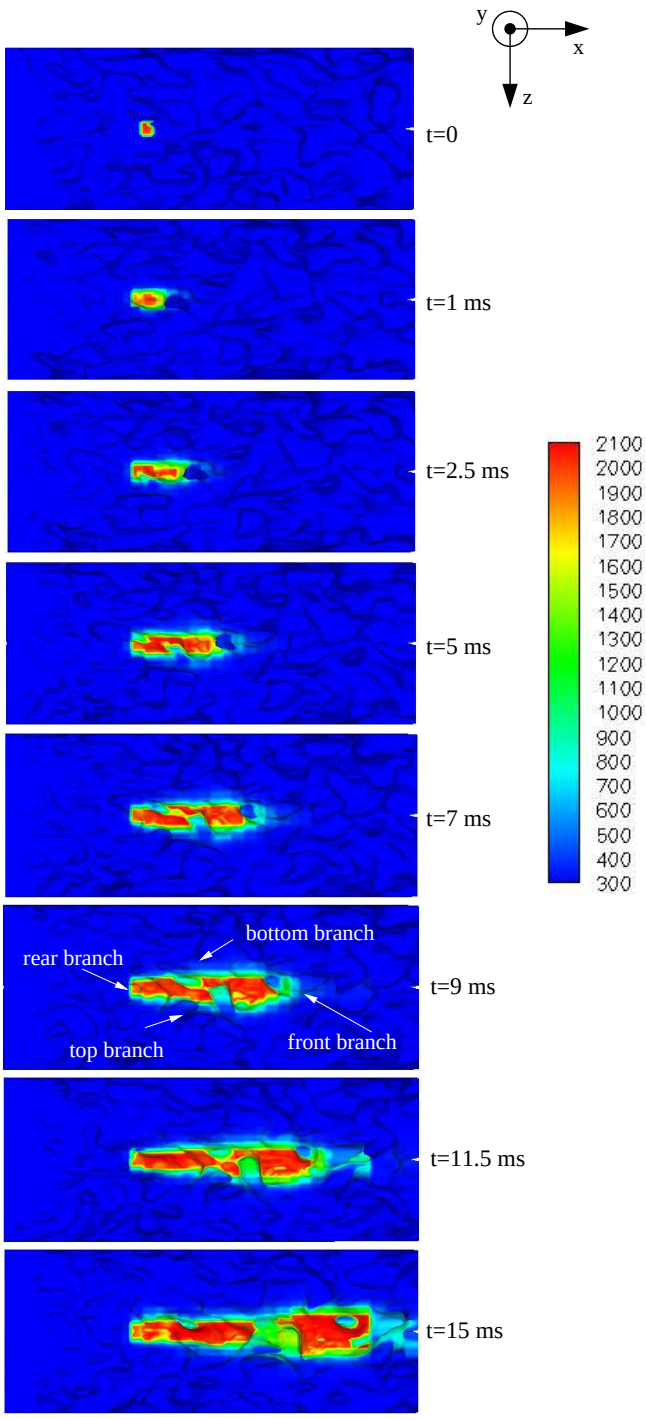

Figure 4.8: Instantaneous isosurfaces of stoichiometric mixture fraction, coloured by temperature [K] at different times from the moment of ignition, case CS1.

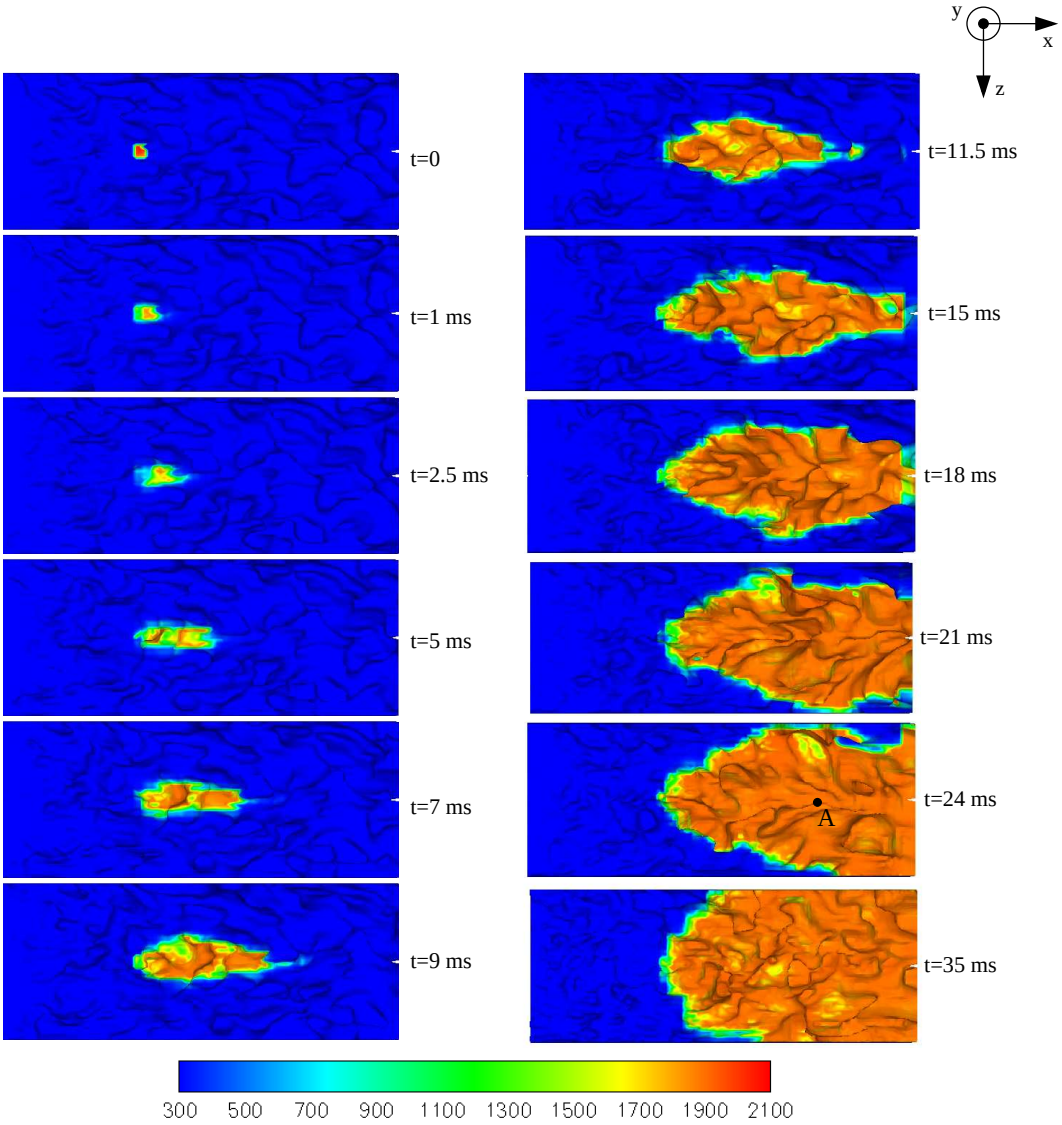

Figure 4.9: Instantaneous isosurfaces of stoichiometric mixture fraction, coloured by temperature [K] at different times from the moment of ignition, case FS1.

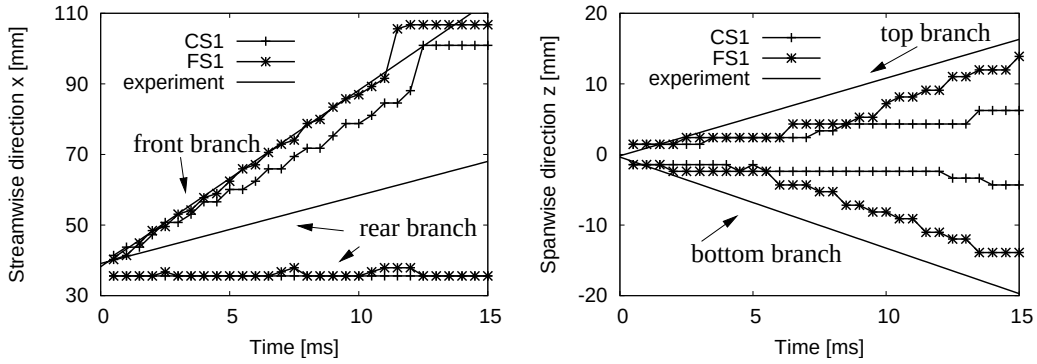

Figure 4.10: Flame location in the streamwise (left) and spanwise (right) directions, cases CS1 and FS1, see Fig. 4.8 for definition of front, rear, top and bottom branch of the flame.

enough near the wall to resolve the boundary layer. The reason for which the flame remains anchored at a velocity higher than in the experiment could be related to the gradient model used for the sub-grid scale conditional flux (see Eq. (2.42)). DNS studies for low turbulence levels ($u'/S_L = 4$) have shown counter-gradient diffusion [120], which, in the context of this study, would assist to 'de-anchor' the flame. The levels of turbulence here are low ($u'/S_L \approx 0.3/0.4 = 0.7$) and it is possible that counter-gradient diffusion is present.

In order to investigate how fluctuations of the velocity field affect the CMC solution, the evolution of the velocity, the FDF of the mixture fraction, the conditional scalar dissipation rate and the conditional temperature and concentrations of CH_4, O_2, CO_2 and H_2O were monitored at close intervals for a period of 1 ms at the location of point A (see Fig. 4.9 for location of A). The results are shown in Fig. 4.11. All three components of the velocity fluctuate significantly and this causes the FDF of the mixture fraction to fluctuate too, both in terms of the mean value and its sub-grid scale variance, since both the location and the width of the FDF changes. The conditional scalar dissipation rate also fluctuates during this time. The fluctuations of the velocity, mixture fraction and scalar dissipation rate seem to

have little effect on the conditional temperature and species mass fractions. They remain almost unchanged implying that the timescale over which they change is larger than the timescale of the flow. The expansion in η-space is a relatively slow process, compared to the flame expansion in physical space.

4.5.2 Effect of convection scheme

In chapter 3 the upwind and a TVD scheme (for the discretisation of the convection term in the CMC equation) were compared in terms of accuracy and computational time for a simplified one-dimensional problem. In this section, the two convection schemes are applied to a real three-dimensional ignition problem and their performance is assessed. The conditional temperature at $\xi = \xi_{st}$ along the x direction at different times from the moment of ignition using the upwind (case CS1) and the TVD scheme (case CS2) is shown in Fig. 4.12. The TVD scheme is clearly shown to be less diffusive and maintains the sharp temperature gradient at the flame front.

In terms of computational time, using the TVD scheme resulted in an increase of the computational time of the order of 50%. Taking Fig. 3.10 under consideration, this increase in computational time appears to be reasonable; for low CFL numbers (as is the case here) the TVD scheme would be almost two times more expensive than the upwind scheme. Taking into account that solving the convection-diffusion equation is only part of the CMC/LES calculation, the 50% increase in computational time is reasonable.

Despite the fact that when using the TVD scheme, the sharp gradient are retained and the solution is in principle more accurate, the flame 'anchoring' observed in section 4.5.1 remains, which implies that it is not a 'numerical' problem but rather a more conceptual problem. The 'anchoring' is due to the fact that there is no extinction of the flamelets that were originally located in the spark. It is possible that close to extinction, the fluctuations of the conditional averages are important and this additional mixing process leads eventually to extinction. Therefore, first-

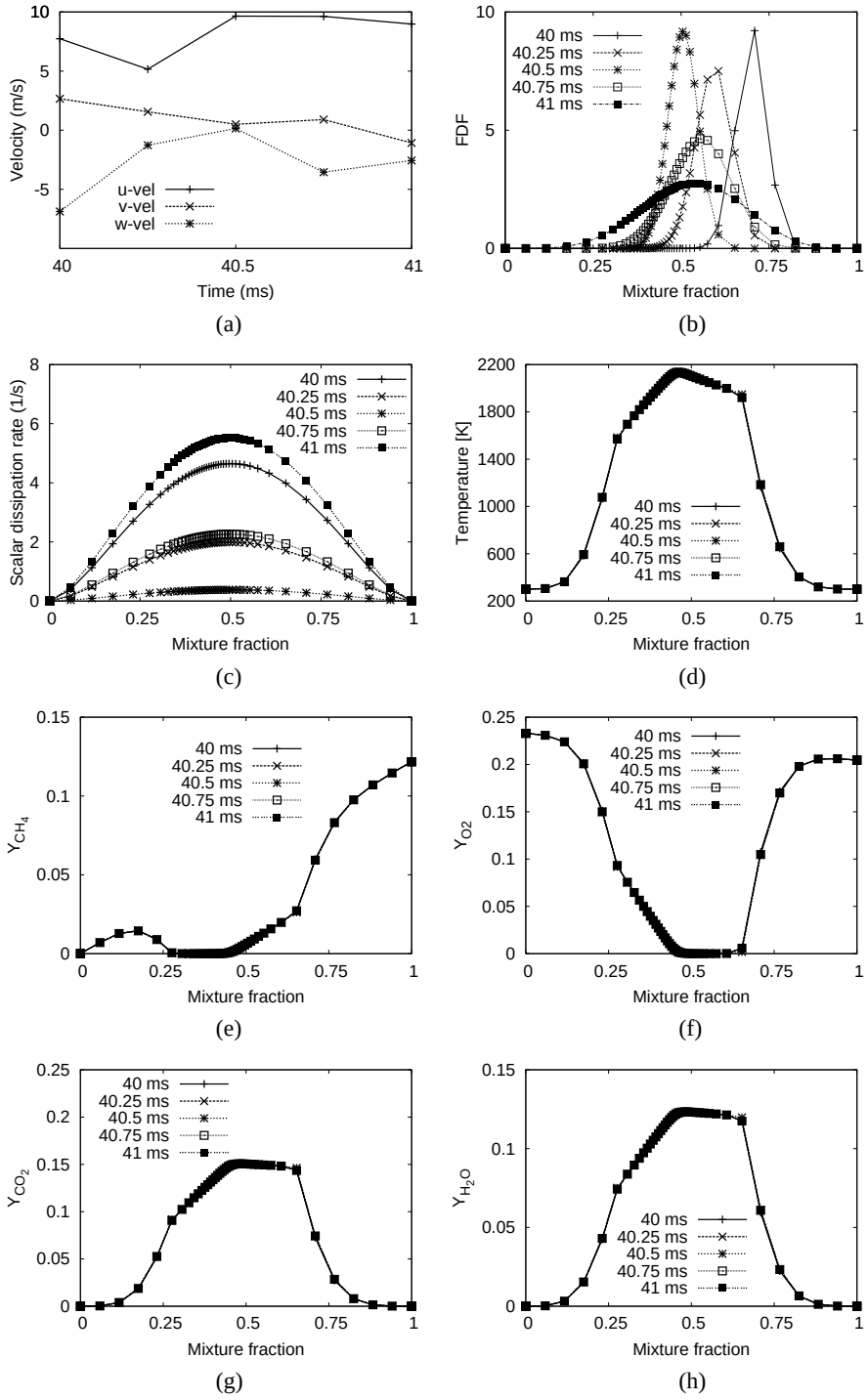

Figure 4.11: Evolution in time of the velocity, the FDF of the mixture fraction, the conditional scalar dissipation rate and the conditional temperature and concentrations of CH_4, O_2, CO_2 and H_2O at point A (see Fig. 4.9) over 1 ms of simulated time, case FS1.

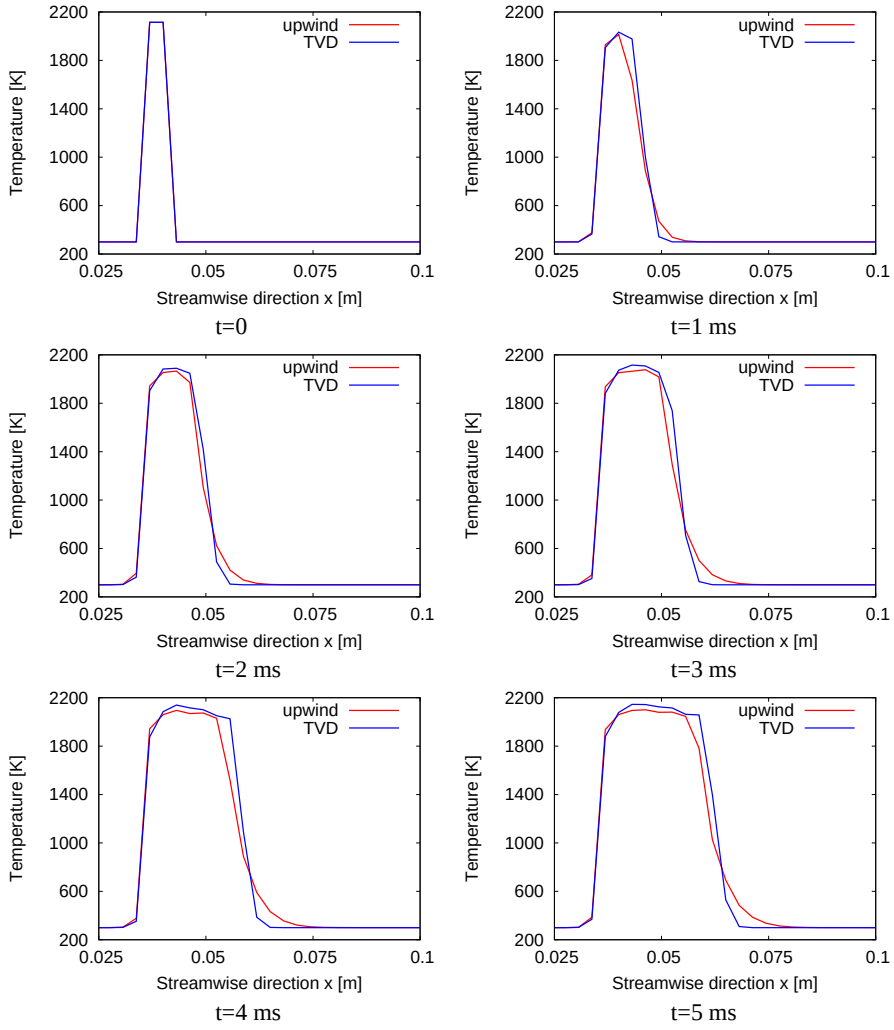

Figure 4.12: Conditional temperature at the stoichiometric mixture fraction ($\widetilde{T|\eta = \xi_{st}}$) along the streamwise direction, at $y = 0$ and $z = 0$ for different times from the moment of ignition, for the upwind (case CS1) and the TVD scheme (case CS2).

order closure may be inappropriate for this type of problems and the variances and co-variances of the conditional averages might have to be taken into account, leading to a second-order closure formulation.

4.5.3 Effect of turbulent diffusion

In order to assess the importance of turbulent diffusion (term T4 in (2.28)) in the flame expansion process, a simulation was performed without that term (case FS2) and compared with case FS1. By directly comparing the results from the two simulations, the relative importance of the resolved and sub-grid scale fluctuations of the velocity will be revealed.

Instantaneous isosurfaces of stoichiometric mixture fraction, coloured by temperature at different times from the moment of ignition for cases FS1 and FS2 are shown in Fig. 4.9 and 4.13 respectively. The two figures look very similar, which suggests that turbulent diffusion has little effect to flame expansion for this problem.

The location of the flame in the streamwise (x) and spanwise (z) directions is shown in Fig. 4.14. Cases FS1 and FS2 produce almost identical results (the two lines cannot be distinguished) which is further evidence that the resolved fluctuations of the velocity dominate over the diffusion.

More detailed comparison is shown in Fig. 4.15 to 4.19 where the conditional temperature is plotted at different streamwise locations at different times from the moment of ignition for different spanwise locations. The spark is located at $x = 40\,\text{mm}$ and spans three CMC cells, located at $z = 0$. 1 ms after ignition, the flame has expanded in the two neighbouring cells (in the z direction) at each side of the spark. After this, the flame stays in the same location and does not expand any further (at 7 ms the image is very similar to 2.5 ms). Further along the streamwise direction, the flow is inert at the start of the simulation (Fig. 4.17 and 4.18, $t = 1\,\text{ms}$ and Fig. 4.19, $t = 1\,\text{ms}$ and $t = 2.5\,\text{ms}$) and only later does the flame arrive and expand.

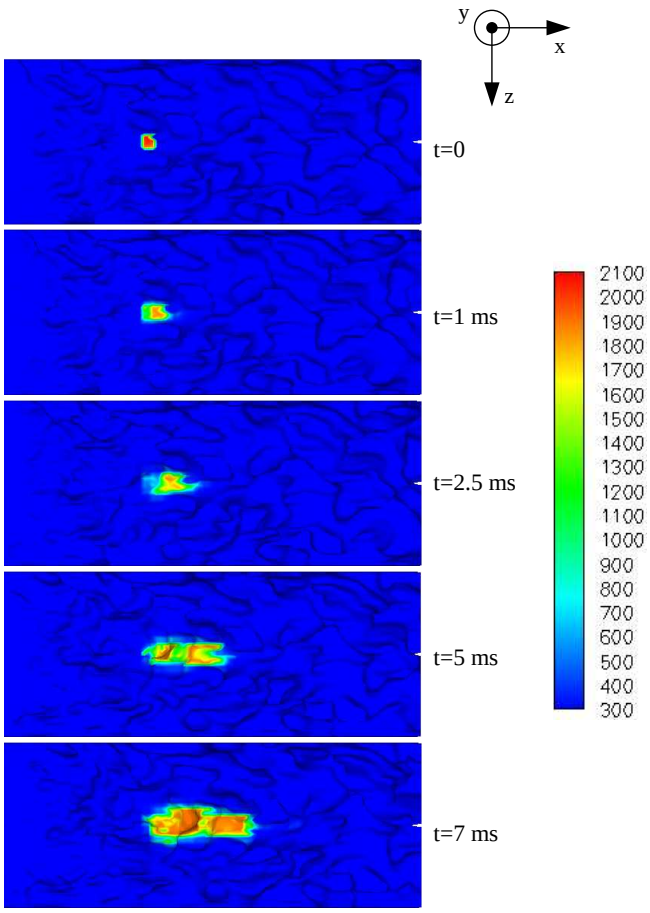

Figure 4.13: Instantaneous isosurfaces of stoichiometric mixture fraction, coloured by temperature [K] at different times from the moment of ignition without diffusion, case FS2.

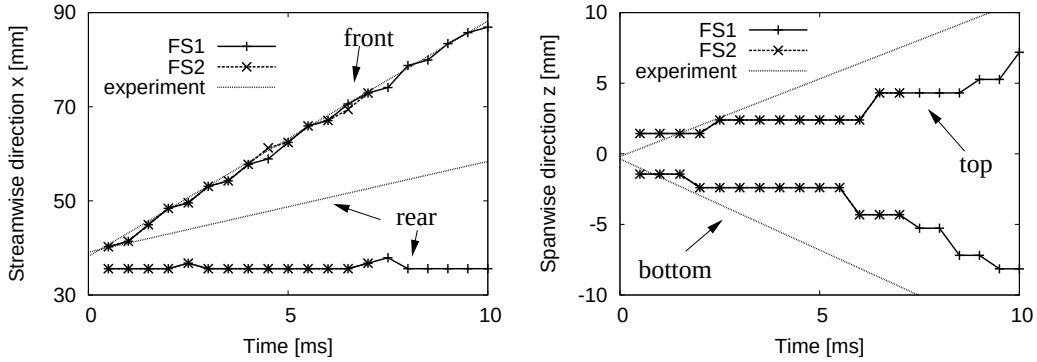

Figure 4.14: Flame location in the streamwise (left) and spanwise (right) directions, cases FS1 and FS2, see Fig. 4.8 for definition of front, rear, top and bottom branch of the flame.

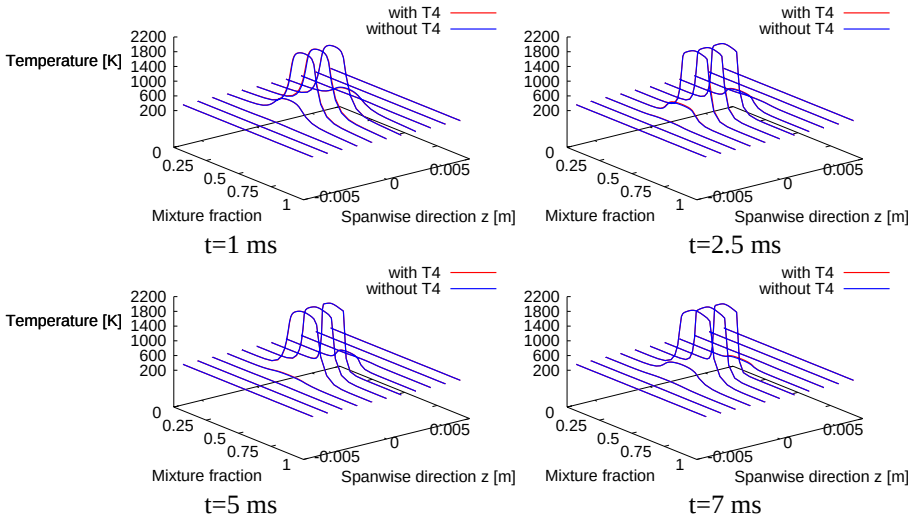

Figure 4.15: Conditional temperature at $x = 40\,\mathrm{mm}$ at different times on the $y = 0$ plane with (case FS1) and without (case FS2) term T4 in Eq. (2.28).

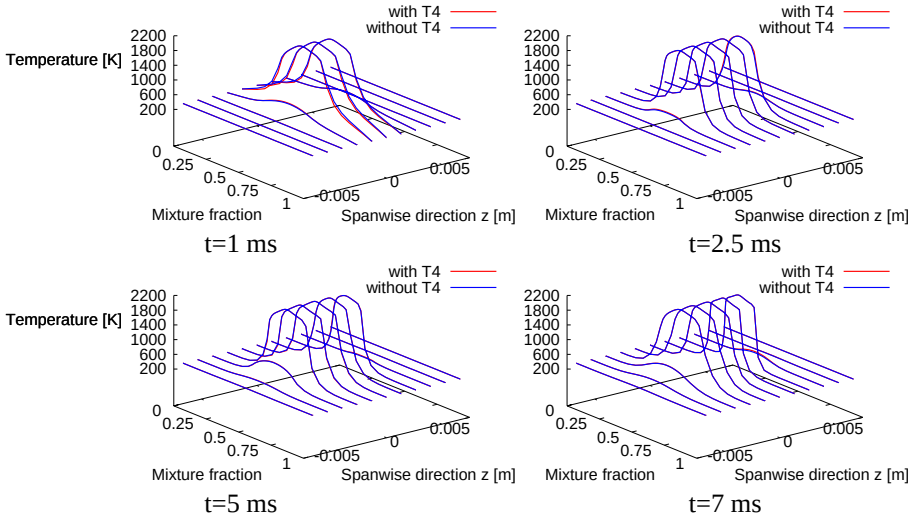

Figure 4.16: As in Fig. 4.15, but at $x = 44.75\,\mathrm{mm}$.

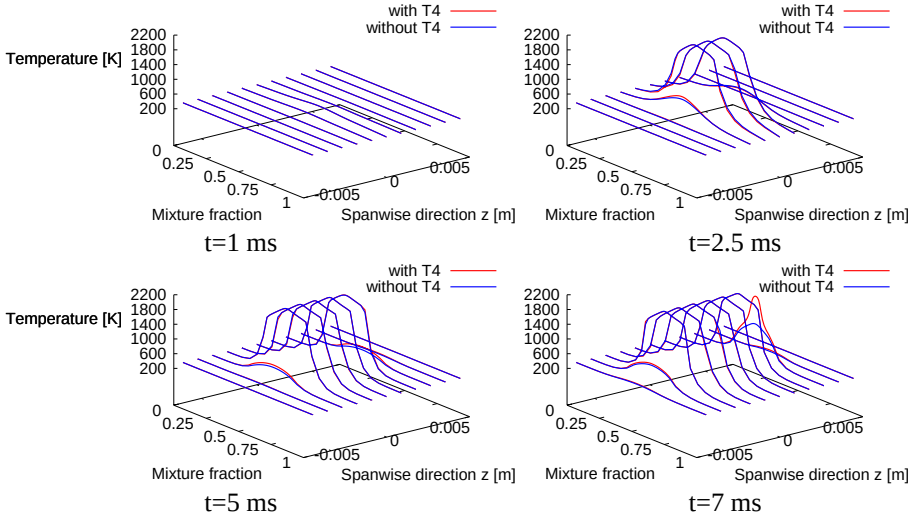

Figure 4.17: As in Fig. 4.15, but at $x = 49.75\,\mathrm{mm}$.

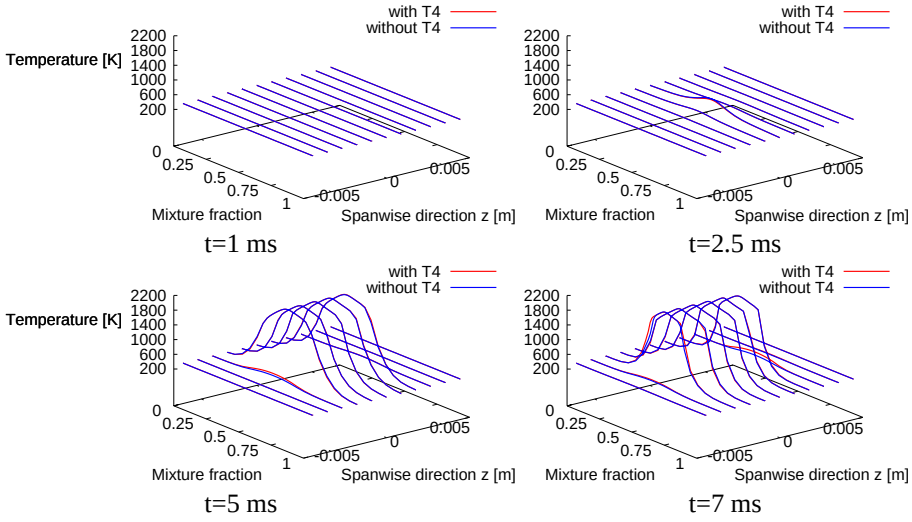

Figure 4.18: As in Fig. 4.15, but at $x = 56.125\,\mathrm{mm}$.

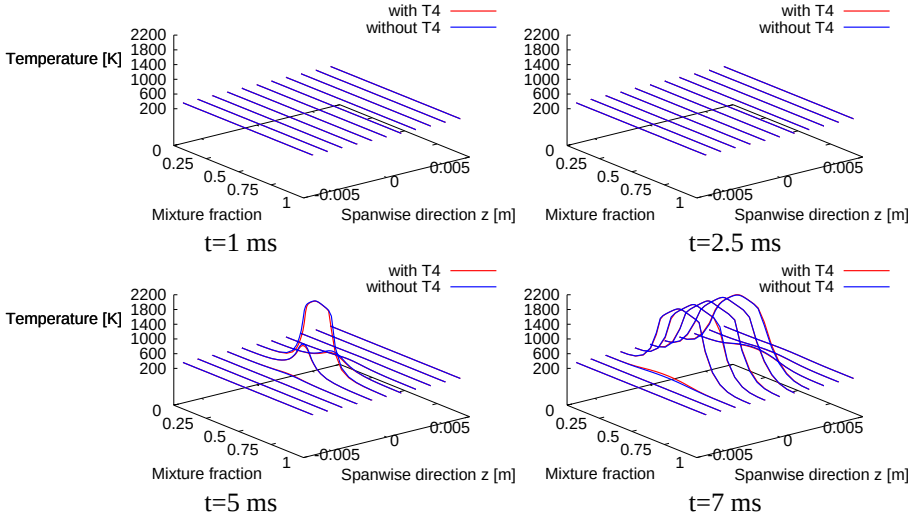

Figure 4.19: As in Fig. 4.15, but at $x = 65.875\,\mathrm{mm}$.

The results from FS1 (red line) and FS2 (blue line) are very similar in most cases, which shows that compared to convection, the sub-grid scale turbulent diffusion is not very significant in the flame expansion process. Small differences can be seen in some locations (for example Fig. 4.17, $t = 7\,\text{ms}$) where the flame expands more quickly as convection is aided by turbulent diffusion, but in general it can be concluded that convection (i.e. the resolved velocity fluctuations) determines the rate of flame expansion.

This conclusion is physically consistent with Ref. [121, 122], where in both the experimental and DNS study, it was found that the local flame edge propagation speed (relative to the fluid) was a fraction of the laminar burning velocity S_L. In our problem, $u'/S_L \approx 1$, so local propagation is less important than flame spreading by the turbulent velocity fluctuations.

4.5.4 Effect of bulk velocity

In order to investigate further the flame 'anchoring' discussed in section 4.5.1 and 4.5.2, a simulation with a higher bulk velocity was performed ($u_b = 8\,\text{m/s}$ in FS3). The instantaneous isosurfaces of stoichiometric mixture fraction, coloured by temperature at different times from the moment of ignition are shown in Fig. 4.20. The flame is seen to detach from the spark location and does not exhibit the same behaviour as when $u_b = 3\,\text{m/s}$. However, the velocity at which the rear branch of the flame moves is much smaller than the mean flow velocity. From Fig. 4.21, where the location of the flame in the streamwise direction is shown, it can be deducted that the flame moves approximately 5 mm in 4 ms, resulting to an average velocity of 1.2 m/s.

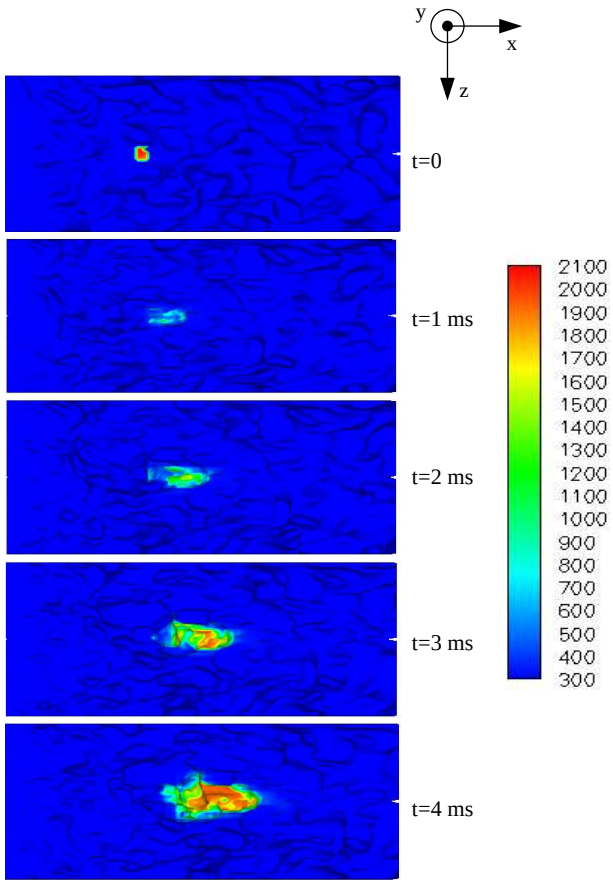

Figure 4.20: Instantaneous isosurfaces of stoichiometric mixture fraction, coloured by temperature [K] at different times from the moment of ignition, case FS3.

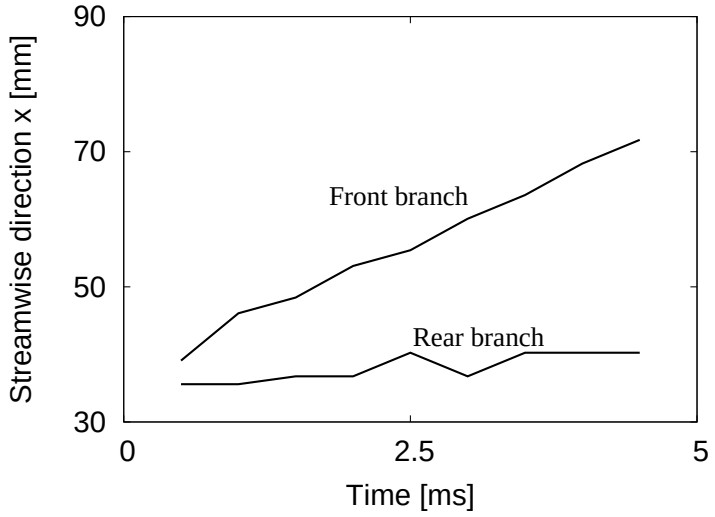

Figure 4.21: Flame location in the streamwise direction, case FS3, see Fig. 4.8 for definition of front, rear, top and bottom branch of the flame.

4.6 Conclusions

LES/CMC calculations of forced ignition in a a simple shearless burner have been presented in this chapter. The sensitivity of the predictions to basic parameters of the CMC, such as the CMC mesh resolution and the convection scheme, but also to the flow conditions (bulk velocity) and to more general modelling parameters (effect of turbulent diffusion) was investigated.

The expansion of the flame was found to be sensitive to the resolution of the CMC mesh. Increased resolution was required to capture the expansion of the flame across the flow (spanwise direction) with reasonable accuracy. However, expansion against the flow and flame extinction could not be predicted. A TVD scheme resulted in a more accurate solution, but at the expense of computational time.

The expansion of the flame was governed mainly by convection (resolved fluctuations of the velocity), since little difference was noticed when the sub-grid scale diffusion term was neglected (term T4 in Eq. (2.28)). By increasing the bulk velocity of the flow, the flame was found to detach from the spark location and convect

with the flow, but at a smaller rate compared to the experiment.

The results for the spanwise direction suggest that the LES/CMC formulation results in reasonable predictions. The discrepancy between the experiment and the simulation for the flame speed in the streamwise direction may be related to the local distortions of the flow due to the steep density gradients, implying that a very good resolution may be needed.

Chapter 5

Ignition of a Bluff-Body Stabilised Methane Flame

5.1 Introduction

Bluff bodies are widely used in engineering applications for the stabilisation of flames. Although the geometry of a real combustor is more complicated than those that have been experimentally and numerically investigated, the structure of the flame can be similar and qualitative conclusions can be drawn. The recirculation zone produced behind the bluff body offers a region of low velocity, giving enough time for the fuel and the air to mix (in the case of a non-premixed flame) and for the flame to stabilise [123]. There have been both experimental (e.g. [124–126]) and numerical (e.g. [40, 55, 60, 76, 127, 128]) studies of flows behind bluff bodies.

The expansion due to combustion will result in an increase of the volume of the recirculation zone behind the bluff body, modifying the velocity field and hence the mixing process. The overall flow structure will evolve during ignition, making this configuration interesting to investigate in terms of the two-way coupling between the LES and the CMC solvers.

In this chapter, LES of ignition events of a turbulent bluff-body non-premixed

methane flame are presented. In particular the experiment of Ref. [11] is simulated. Preliminary LES of this experiment with tabulated chemistry have also appeared [26], where it was shown that the time history of the velocity and the mixture fraction can have an impact on the success or failure of a spark. That work further highlighted the value of LES for ignition problems. The fuel is injected radially through a slit before the exit of the bluff body (more details about the configuration are presented in section 5.2), creating a reasonably well-mixed recirculation zone that presents an opportunity to additionally examine how good the CMC predictions will be in a flow with well-mixed regions. It has already been mentioned in chapter 1 that a rich behaviour has been observed in this ignition experiment. The probability of finding a kernel was found to be smaller than the probability of finding flammable mixture, which may be attributed to the fluctuations of the velocity (and hence of the strain rate). The highest ignition probability was in the shear layer between the annular jet and the recirculation zone, where the mixture is within the flammability limits and the radial velocity is negative, thus bringing heat and species from the spark location to the recirculation zone. Furthermore, three different modes of failed ignition were observed: (i) failure to initiate a kernel, (ii) initiation of a kernel that is then convected away and (iii) flame growth, filling a significant part of the burner, but inability to stabilise the flame [13].

The objective of this chapter is to examine whether the LES/CMC approach is appropriate for problems of forced ignition and flame expansion in non-premixed configurations of this complexity and to investigate how accurately the different phenomena observed in the experimental studies can be reproduced. Different spark locations and sizes are examined, while chemical mechanisms of different complexity are presented to investigate which, if any, of the characteristics of flame expansion can be reproduced using a simple (and hence less computationally expensive) chemical mechanism. The overall flame stabilisation process is also examined.

5.2 Configuration

The experiment modelled in this chapter has been performed in the University of Cambridge, Department of Engineering. Details on the configuration, the measurement techniques and the set of measurements can be found in Ref. [11]. This setup has also been used for an experimental study of the response of a premixed flame to imposed oscillations of the inlet velocity [129], while a CFD study of the same problem has also been performed [130].

A schematic of the investigated burner is shown in Fig. 5.1. It consists of two concentric cylindrical ducts; one of inner diameter 35 mm carrying air and one of outer diameter 7 mm carrying fuel (pure methane). The latter leads to a bluff body of diameter $D_b = 25\,\text{mm}$ with a 45° cone angle, resulting in a blockage ratio of approximately 50%.

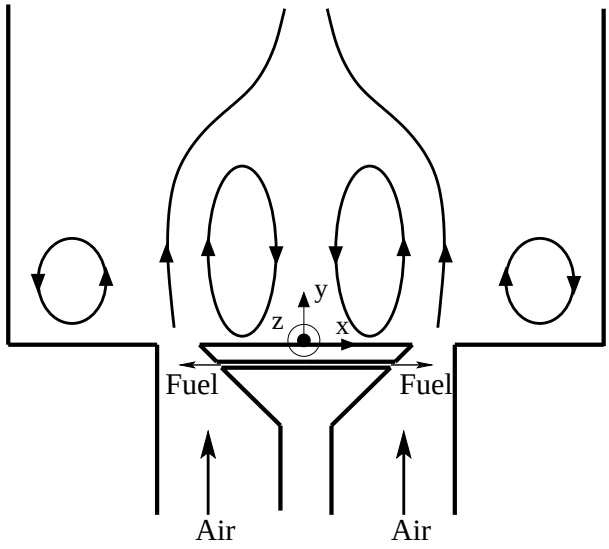

Figure 5.1: Schematic of the bluff-body burner.

The fuel is injected radially through a 0.7 mm wide slit, situated 2 mm before the exit of the bluff body. The bulk velocity of the air stream at the exit of the bluff body is $V_b = 10\,\text{m/s}$, while that of the fuel at the injection point is $U_f = 5\,\text{m/s}$. Both air and fuel enter the burner at room temperature.

The burner is surrounded by a cylindrical tube of diameter 70 mm and length 80 mm. Behind the bluff body, a large recirculation zone is created (Central Recirculation Zone, CRZ), while a toroidal recirculation zone is also formed at the sides of the cylindrical tube. The y-axis represents the axial direction, while the x and z axes define a horizontal plane, normal to the axial direction.

In the spark ignition experiments, ignition was achieved by means of two 1 mm thick tungsten electrodes, separated by a 2 mm gap. The nominal values of the electrical spark energy and duration were 200 mJ and 500 μs respectively [11].

5.3 Computational meshes

Three LES meshes of different resolution were used in the simulations presented in this chapter (Table 5.1). They all extend to 25 mm upstream of the bluff-body and 50 mm downstream of the cylindrical tube surrounding the burner. The coarse mesh consists of approximately 820k cells, the normal mesh of 1.8M cells and the fine mesh of approximately 4.9M cells. A slice through a $z = 0$ plane is shown in Fig. 5.2. The normal mesh is much finer than the coarse mesh in the shear layer, but also in the fuel injection region. The fine mesh is finer than the normal mesh in the same regions, but also in the azimuthal direction, where it has twice the number of cells. A detail of the fuel injection region is shown in Fig. 5.3. It will be demonstrated later in this chapter that the resolution in this region is crucial for the prediction of the mixing field.

A cut through a $y = 20$ mm plane for the coarse mesh is shown in Fig. 5.4 where the O-grid structure, which is suitable for cylindrical geometries, is shown.

5.4 Inert flow

Before the ignition simulations, simulations of the inert flow were performed to assess the quality of the meshes and the velocity and mixture fraction predictions. The

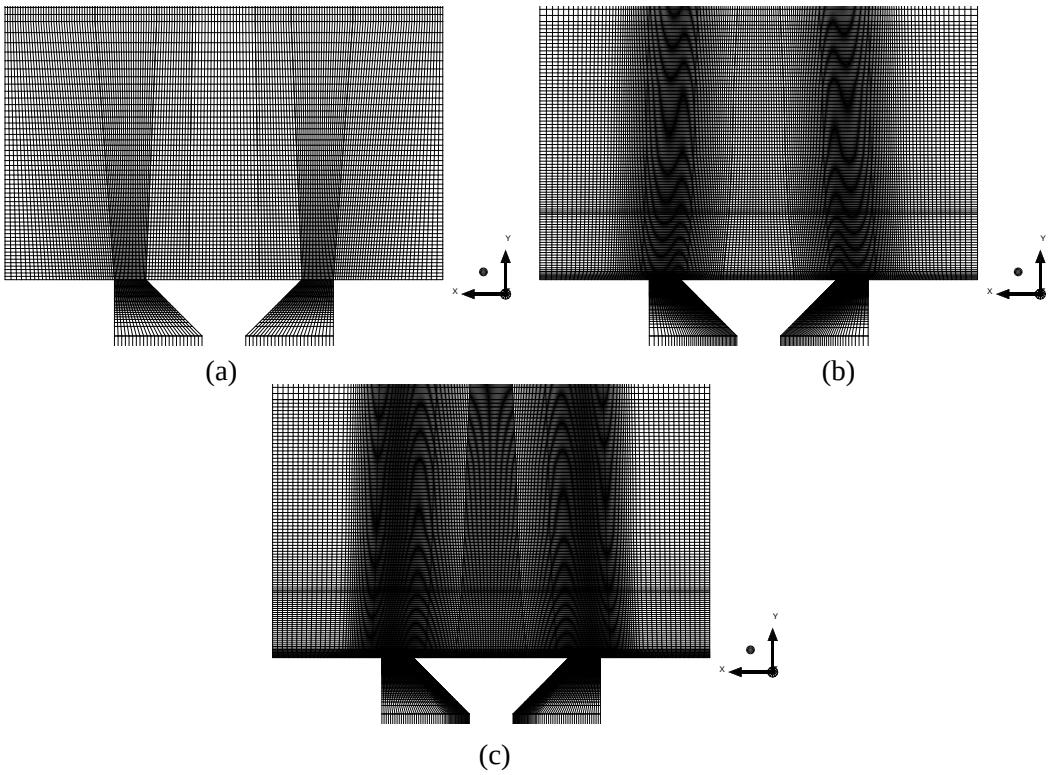

Figure 5.2: Meshes of different resolutions, $z = 0$ plane, a) coarse mesh, b) normal mesh, c) fine mesh.

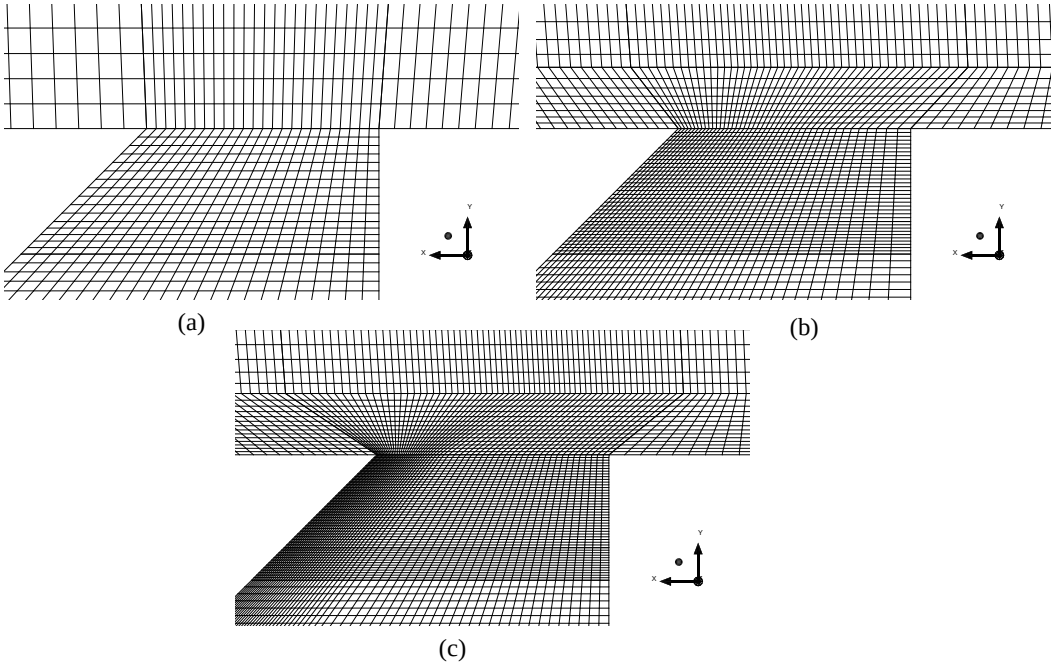

Figure 5.3: Meshes of different resolutions, $z = 0$ plane. Detail, corner of bluff body, a) coarse mesh, b) normal mesh, c) fine mesh.

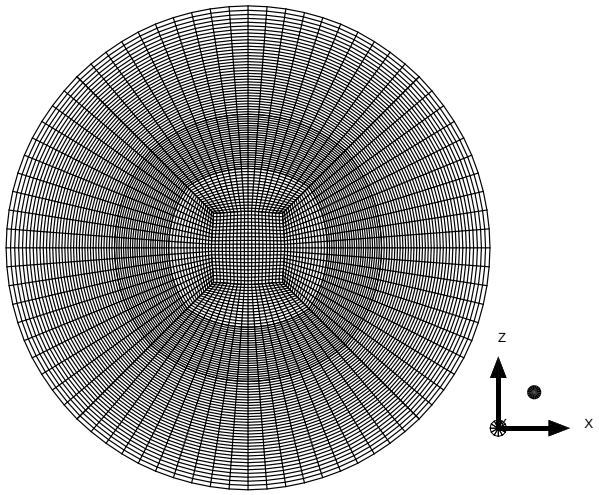

Figure 5.4: Coarse mesh, $y = 20\,\mathrm{mm}$-plane.

Table 5.1: Performed inert flow simulations.

Case	Mesh size	Fuel?
I1	820k	No
I2	1.8M	No
I3	1.8M	Yes
I4	4.9M	Yes

performed simulations are summarised in Table 5.1. The coarse mesh was used in case I1, the normal mesh in I2 and I3 and the fine mesh in case I4. No fuel was injected in I1 and I2 (no fuel was present when the velocity was measured), while methane was injected in I3 and I4. In every case, the timestep was selected so that the maximum CFL number in the domain was smaller than 0.5.

Instantaneous contour plots of the mixture fraction from the experiment and the LES (case I4) are shown in Fig. 5.5. The basic structure of the flow is captured accurately (quantitative comparison will be presented later in this section). The fuel breaks up before the exit of the bluff-body, which is demonstrated by the low value of ξ at the shear layer. The CRZ is reasonably well-mixed with $\xi \approx 0.08$, which means that it is richer than stoichiometric (it is noted that $\xi_{st} = 0.055$). Contour plots of the mean axial velocity and mixture fraction fields are shown in Fig. 5.6. In the axial velocity contour, the recirculation zone can be clearly seen (blue colour) surrounded by the high velocity jet (red colour). The mean mixture fraction field shows the well-mixed recirculation zone, surrounded by a mixing layer across which the value of ξ eventually goes to zero.

5.4.1 Velocity

The radial profiles of the mean and the resolved RMS of the axial and radial velocity for different distances y/D_b from the bluff body, using the coarse (case I1)

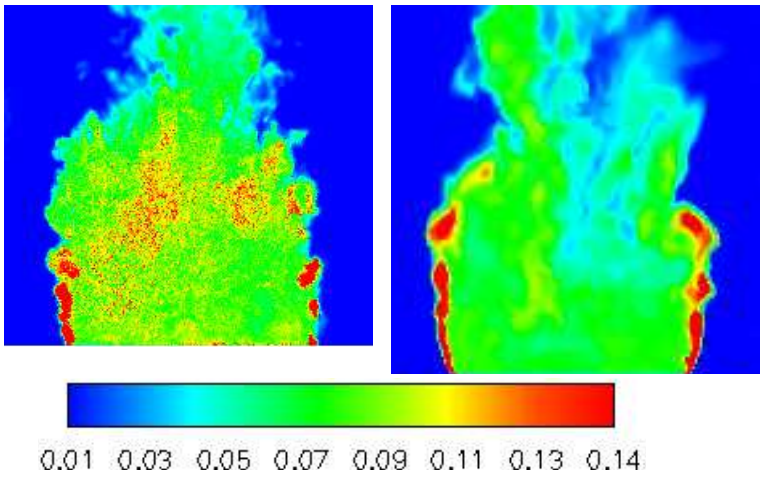

Figure 5.5: Instantaneous contours of the mixture fraction. Left: experiment [11], right: LES (case I4). Image size is 40×40 mm.

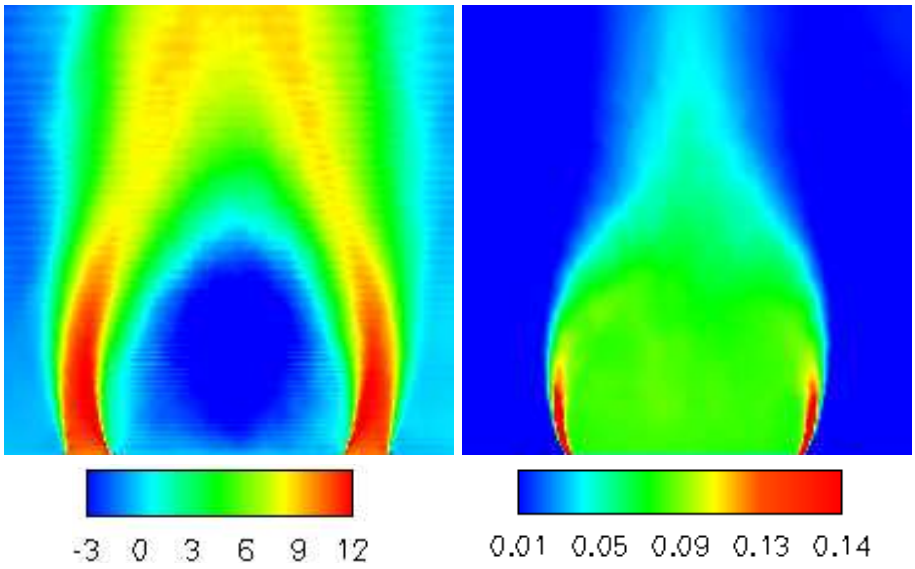

Figure 5.6: Mean axial velocity in m/s (left) and mixture fraction field (right) from LES (case I4). Image size is 50×50 mm.

and the normal (case I2) mesh, compared to the experimental data (laser doppler measurements) are shown in Fig. 5.7. Both meshes produce excellent predictions of the mean axial velocity, while unexpectedly the RMS is better predicted in case I1. The axial velocity has a peak value of approximately $1.2V_b$ ($V_b = 10\,\mathrm{m/s}$) after the exit of the bluff-body and a minimum value of approximately $-0.5V_b$ inside the recirculation zone at $y/D_b = 0.62$. After the exit of the bluff-body, mixing takes place and the velocity profile becomes more uniform. The recirculation zone is predicted to be approximately $0.8D_b$ wide and $1.2D_b$ long, which is consistent with experimental studies of other flows behind bluff bodies [125]. The level of fluctuations of the axial velocity is also predicted accurately. They reach their highest value at the exit of the bluff-body and they are equal to approximately 15% of V_b inside the recirculation zone. Both meshes reproduce very well the radial velocity, with the normal mesh (case I2) producing results which are closer to the experimental data. The turbulence is anisotropic in most locations. Apart from the location close to the bluff-body ($y/D_b = 0.22$), the axial component of the RMS seems to be low inside the CRZ ($r/D_b < 0.5$) and higher at the shear layer ($r/D_b > 0.5$), whereas the radial component is higher inside the recirculation zone and lower in the shear layer. Due to the good prediction of the velocity field using the normal mesh, a simulation with no fuel using the fine mesh was not performed. It was considered that the normal mesh (and possibly even the coarse mesh) is adequate for the prediction of the velocity field with reasonable accuracy.

5.4.2 Mixture fraction

Radial profiles of the mean and the resolved RMS of the mixture fraction using the normal (case I3) and the fine (case I4) mesh, compared with experimental data (taken with PLIF of acetone laden with the fuel) are shown in Fig. 5.8. The distribution of the mixture fraction is clearly more sensitive to the resolution of the mesh than the velocity field. The normal mesh (case I3) over-predicts largely the

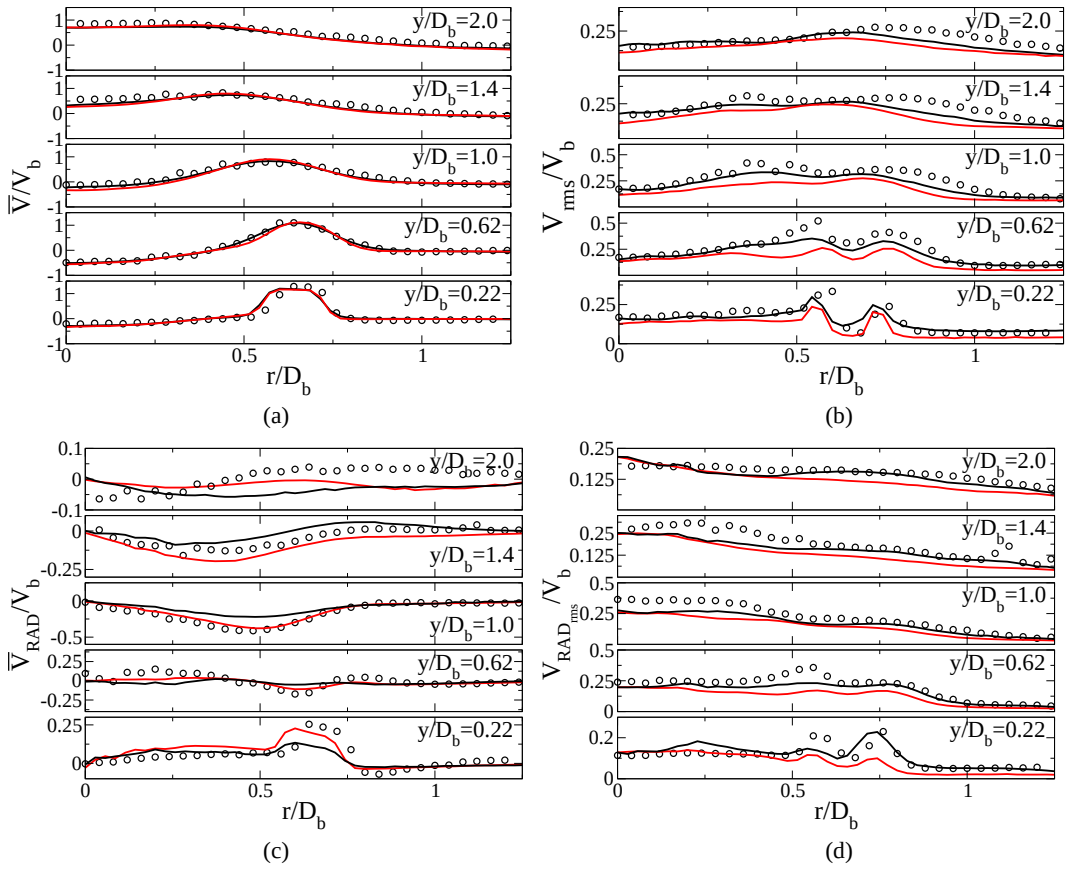

Figure 5.7: Radial profiles of a) the mean axial, b) the RMS of the axial, c) the mean radial and d) the RMS of the radial velocity at different distances from the bluff body. Symbols: experimental data [11], black lines: case I1 (coarse mesh), red lines: case I2 (normal mesh).

value of ξ everywhere in the flow. This is because it cannot capture the break-up of the fuel jet before the exit of the bluff body, whereas the fine grid (case I4), which has been refined in that region, can. The RMS of the mixture fraction is also more accurately predicted in the fine grid simulation. At $y/D_b = 0.2$, the two meshes produce similar results, but further downstream the fine mesh simulations are closer to the experimental values. All the reacting flow simulations which follow in the next section were performed using the fine grid. Note that with an LES code which used unstructured meshes, it would have been possible to resolve well this region without having to have exceedingly fine resolution everywhere. However, such an LES code was not available.

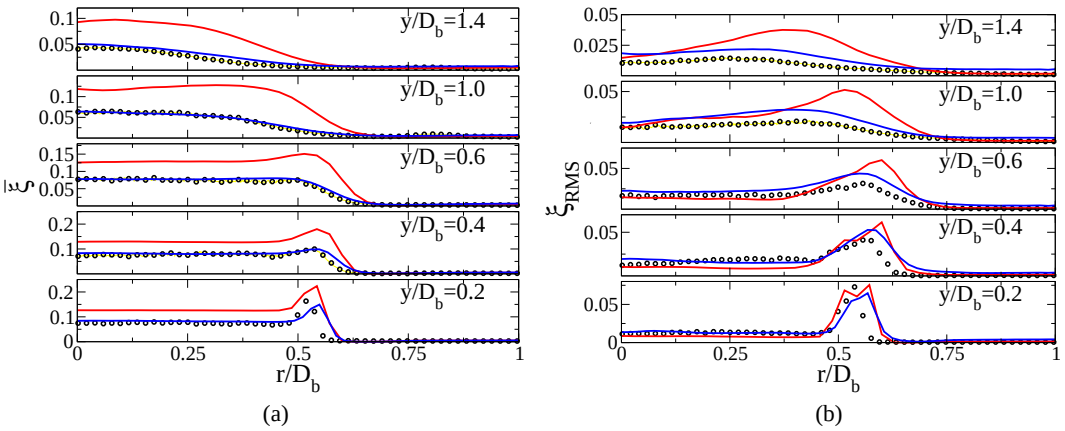

Figure 5.8: Radial profiles of a) the mean and b) the RMS of the mixture fraction at different distances from the bluff body. Symbols: experimental data [11], red lines: case I3 (normal mesh), blue lines: case I4 (fine mesh).

5.4.3 Flammability Factor

In addition to the mean and the RMS of the mixture fraction, the flammability factor F was also calculated. F is defined as the cumulative probability of a potentially

flammable mixture occurring at a given point in the flow [19]:

$$F = \int_{\xi_{lean}}^{\xi_{rich}} P_R(\eta) d\eta \tag{5.1}$$

where $\xi_{lean} = 0.028$ and $\xi_{rich} = 0.089$ are the lean and rich flammability limits respectively and $P_R(\eta)$ is the resolved probability density function of the mixture fraction, composed over a simulated time of 56 ms. This corresponds to 22.4 D_b/V_b, which provides sufficient statistical convergence. Contour plots of F, obtained from experimental data and LES (case I4), are shown in Fig. 5.9. There is very good agreement between the two with both the shape and the values of F being accurately predicted. The flammability factor takes its highest values inside the recirculation zone and at the stagnation point. Just at the exit of the bluff-body, in the location of the annular jet, the flammability factor is very low, since at that point the mixture is rich in fuel, as can be observed in the contour of the mean mixture fraction in Fig. 5.6.

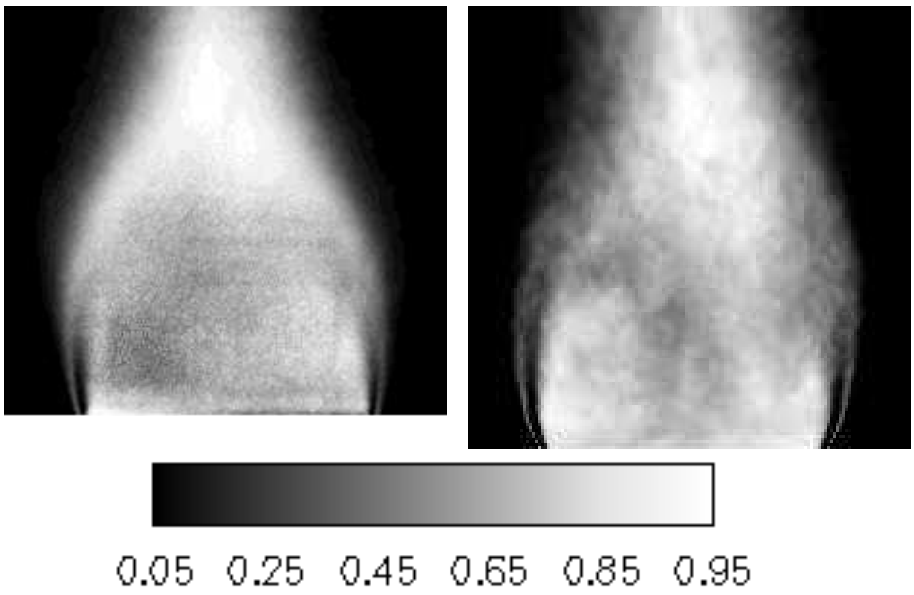

Figure 5.9: Contours of the flammability factor F (see eq. (5.1)). Left: experiment [11], right: LES (case I4). Image size is 40×40 mm.

The conclusion from the inert flow simulations is that the LES reproduces with

acceptable accuracy the velocity and mixture fraction fields both in terms of means and fluctuations, but also in terms of probability density functions. Similar levels of accuracy have been achieved in the LES of Ref. [26], where an unstructured mesh was used. Using the fine mesh, the level of the sub-grid scale turbulence was in most places less than 5% of the resolved, while in some locations, especially near the shear layer, it rises to almost 20%. This is consistent with the fact that near the shear layer the turbulent length-scale is small compared to locations further downstream. Note that these estimates of the level of the sub-grid scale turbulence are approximate since they depend on the model used for the calculation of the sub-grid scale stresses. The fact that in most regions the turbulence is very well resolved by the LES can be justified by the fact that the flow studied here does not have a very high Reynolds number and therefore much of the turbulent spectrum is resolved.

5.5 Preliminary flame results

Before the ignition simulations, which form the main body of this chapter, preliminary flame results using the normal mesh are presented. Despite the fact that the mixing field is not predicted very accurately (see Fig. 5.8), these results give an idea of the expected flame. Furthermore, the two options for calculating the integrated diffusivity (see section 2.4.3.6 and table 2.1) are used and compared here.

The 16-species mechanism [8] (analysed in chapter 3) was used to provide the chemical source terms. At the air and fuel inlets, frozen mixing distributions of reactive scalars against mixture fraction were used as input (i.e. 'frozen flamelet'). Initialisation of the simulation was achieved by starting from low-scalar dissipation rate distributions corresponding to a flame, calculated by a stand-alone 0D-CMC code (without physical transport, Eq. (3.11), 'burning flamelet'). This was initialised at all regions downstream of the bluff body. The choice of inlet and initial conditions resulted in a small lift-off region, where the gradients of the conditional

averages are steep, which provides an opportunity for differences between the options discussed in chapter 2 on the LES-CMC implementation to show.

Two instantaneous images of the flame are shown in Fig. 5.10 and 5.11. The integrated diffusivity used here is D_{t_2} (Eq. (2.64)). It is clear that there are strong fluctuations of the flow field. There always seems to be a high reaction rate at the annular jet, where the fuel and oxygen mix. In the recirculation zone, the reaction rate and the concentrations of all the species seem to be fluctuating, according to the concentrations of fuel and oxygen. In the recirculation zone of the flame in Fig. 5.11, the mixture fraction takes values much higher than the stoichiometric value, which implies that rich combustion is taking place. This can be confirmed by the relatively high concentration of CH_2O.

In Fig. 5.12 contours of the azimuthally and time-averaged mixture fraction, temperature, reaction rate and a number of major and minor species are shown. The flame seems to be lifted with a lift-off height of approximately 6 mm. A lift-off height can be defined as the location at which $\widetilde{Y}_{OH} = 0.002$, which corresponds to 45% of the peak value of $\widetilde{Y}_{OH}$ of a steady 0D-CMC flame, calculated for $N_0 = 5\,\mathrm{s}^{-1}$ (see Eq. (2.39)). This structure is consistent with the experimental results [11], and the local flame structure there in mixture fraction space shows a gradual progression from the incoming 'frozen' distributions to the 'burning' distributions, as in lifted jet flames at the stabilisation height [54].

In Fig. 5.13, the integrated diffusivity is D_{t_1} (Eq. (2.63)). It is evident that the two flames have very similar shapes. The reaction rate reaches its highest value in the layer where the fuel and oxygen mix and therefore stoichiometric mixture fraction is achieved.

The two flames look very similar qualitatively. The fact that different diffusivities have been used, would affect the position where the flame would stabilise. D_{t_1} is predicted to be approximately one or two orders of magnitude smaller than D_{t_2} (Eq. (2.64)), depending on the local strain rate. In Fig. 5.13), the flame seems to stabilise in a position which is slightly higher than in Fig. 5.12. This is demonstrated by the

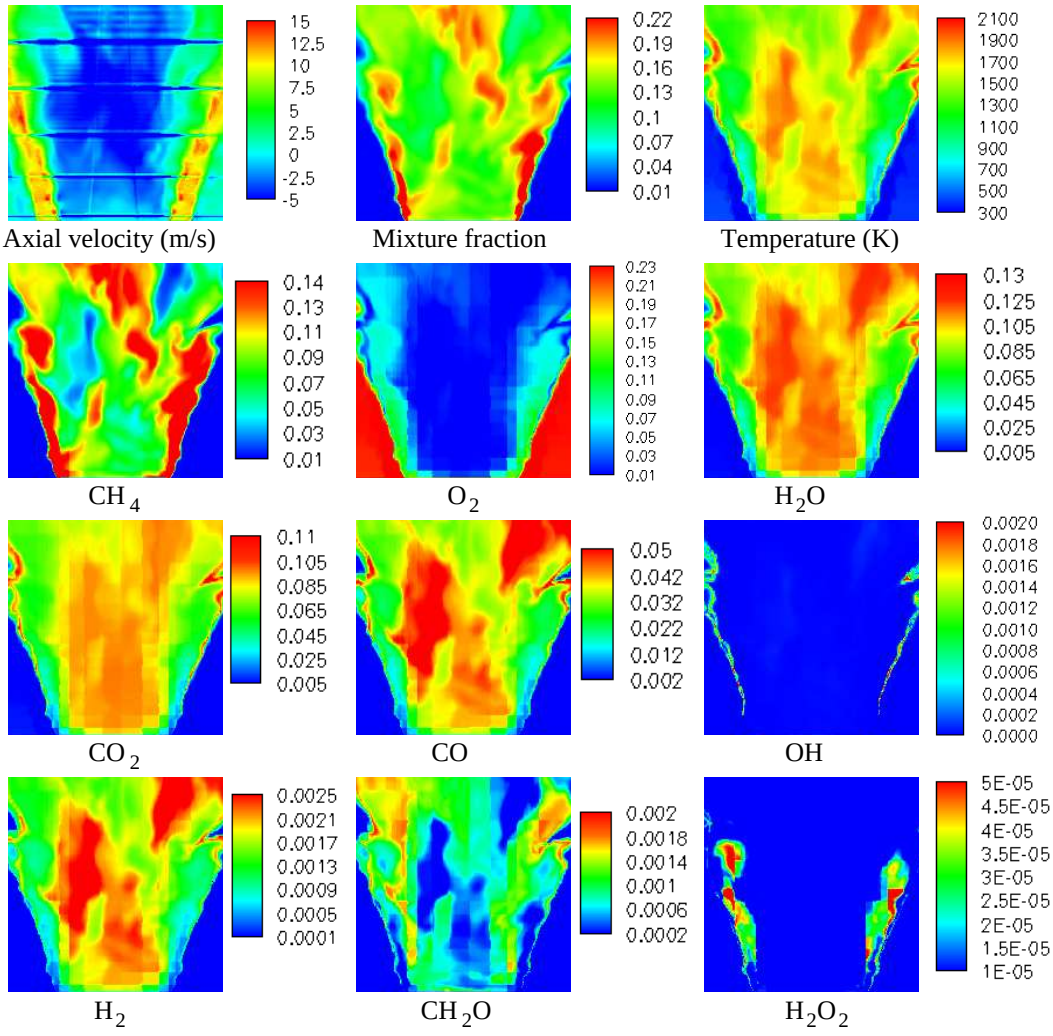

Figure 5.10: Instantaneous contours of the mixture fraction, temperature, heat release rate and mass fractions of species of the bluff-body stabilised flame. Image shown is $70 \times 85\,\text{mm}$, normal mesh.

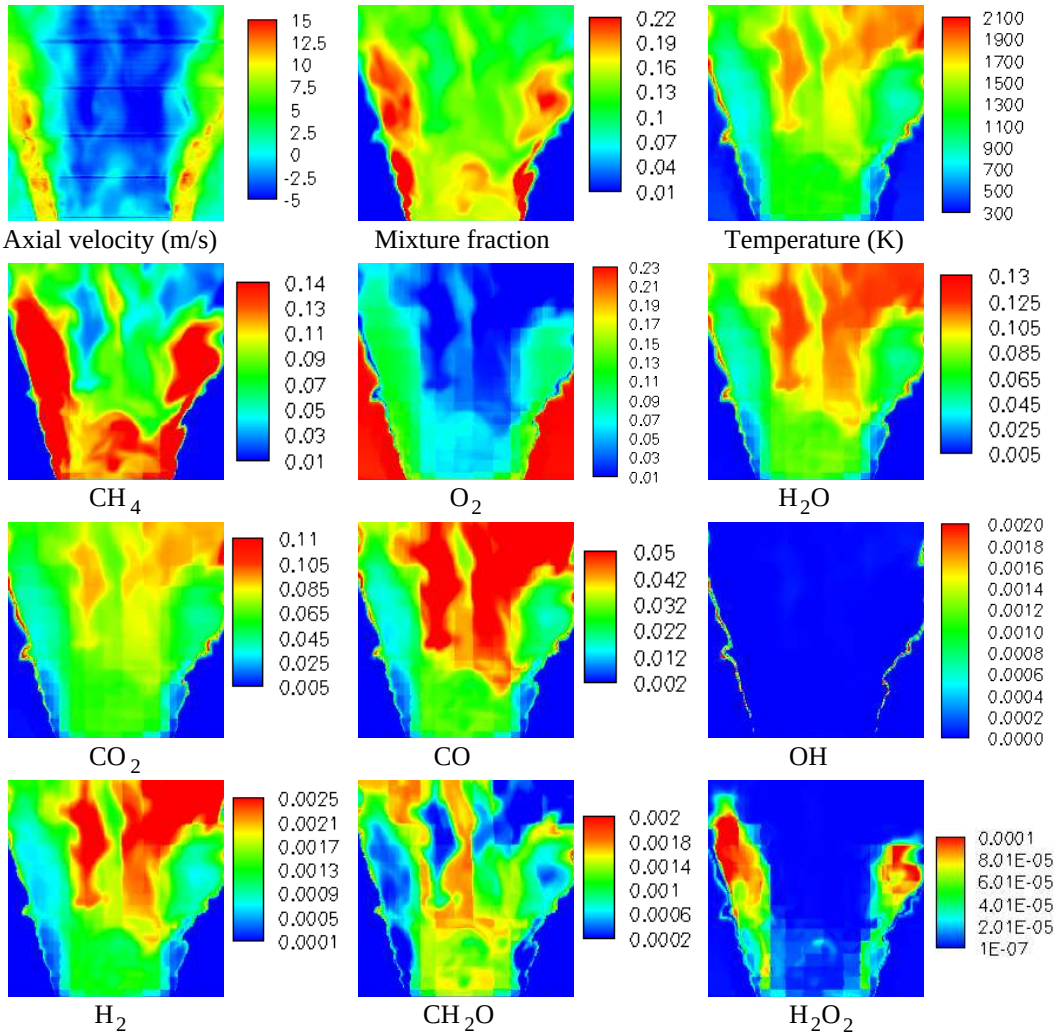

Figure 5.11: As in Fig. 5.10, but at a different time instant.

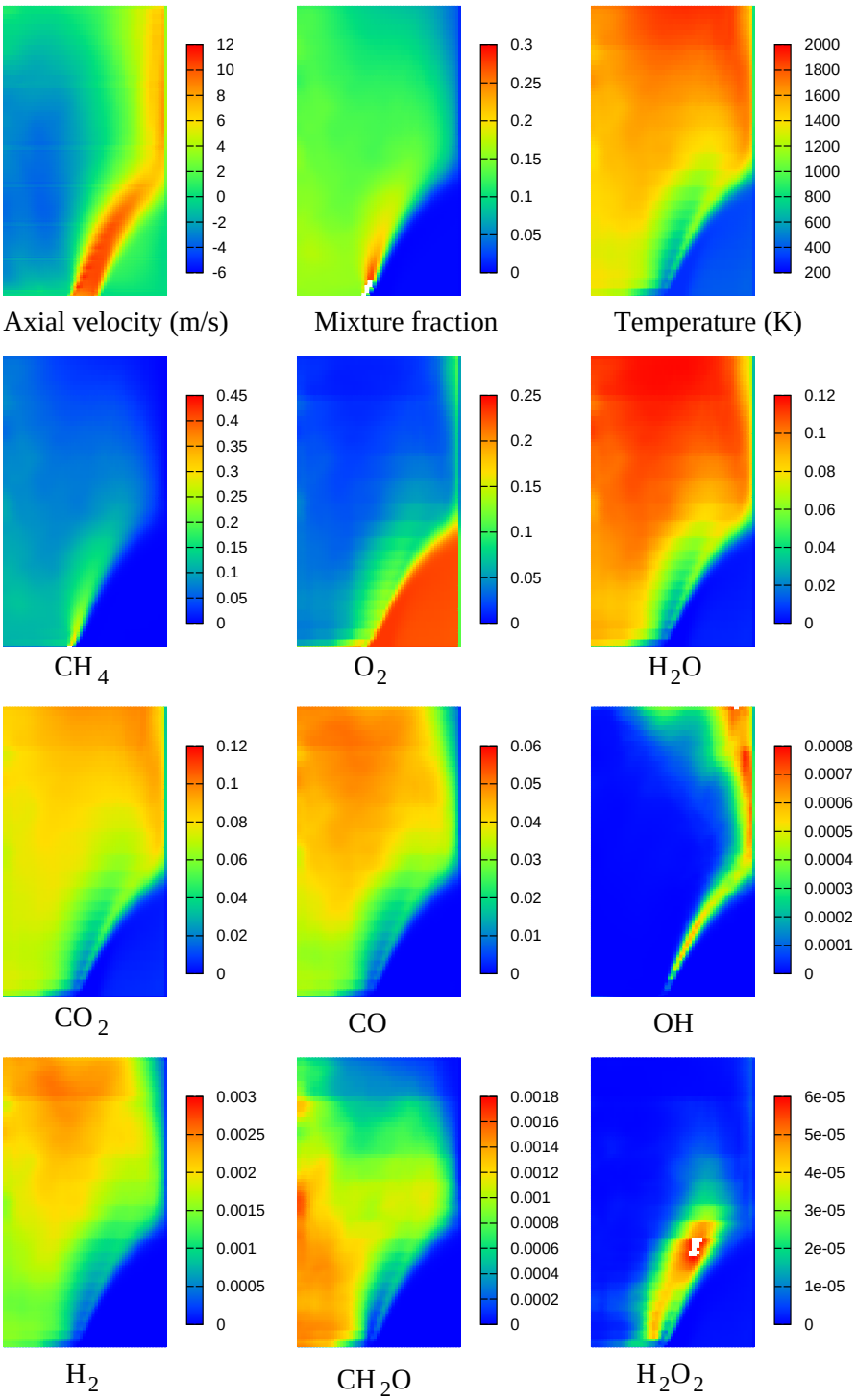

Figure 5.12: Contours of the time-averaged mixture fraction, temperature, heat release rate and mass fractions of species of the bluff-body stabilised flame. Size of each image shown is 35×80 mm, normal mesh.

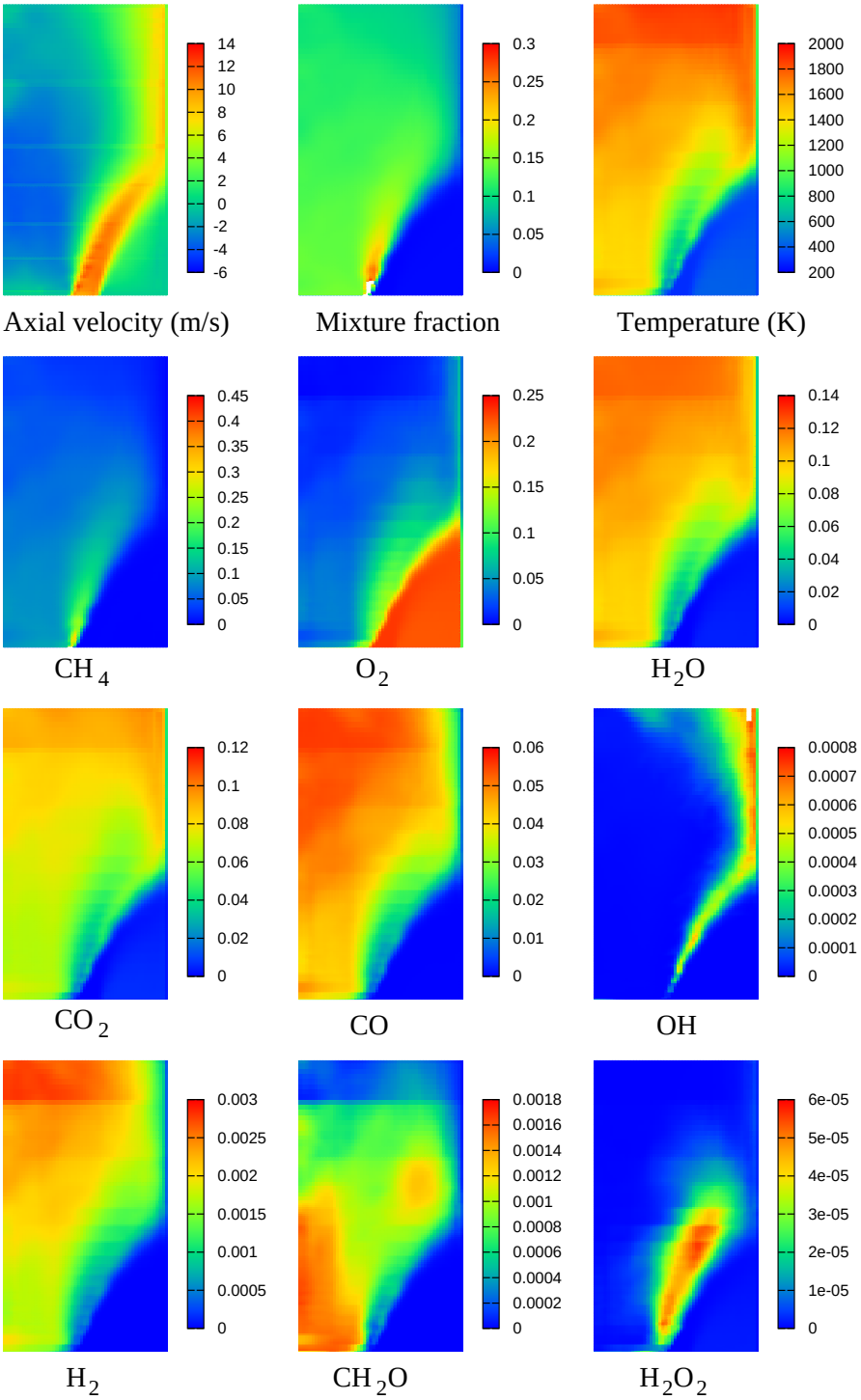

Figure 5.13: As in Fig. 5.12, but D_{t_1} (Eq. (2.63)) is used instead of D_{t_2} (Eq. (2.64)).

concentration of OH and the contours of the temperature. This is seen more clearly in Fig. 5.14 where the line contours of the mass fractions of OH are shown, close to the exit of the bluff-body. Using the same definition as before ($Y_{OH} = 0.002$), the lift-off heights using the two models for D_t^* are within 8% of each other. The small difference between the two lift-off heights may be due to the dominance of the radial convection in the stabilisation of the flame, as will be shown later in this chapter.

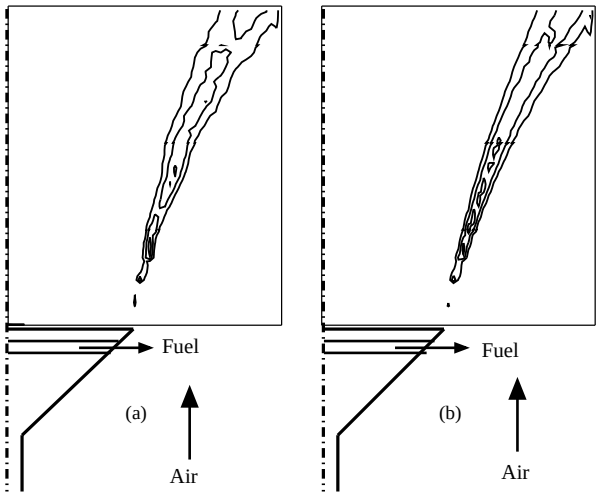

Figure 5.14: Line contours of the time averaged mass fraction of OH using a) D_{t_1} (Eq. (2.63)) and b) D_{t_2} (Eq. (2.64)). Image shown (excluding the sketch of the bluff-body) is $30 \times 35\,\text{mm}$, normal mesh.

5.6 Ignition transient

5.6.1 CMC mesh

A coarser mesh than the LES mesh was used to solve the CMC equations, as is the common practice [2, 61]. The CMC mesh is shown in Fig. 5.15. It consists of $15,625$ ($25 \times 25 \times 25$) cells in physical space, clustered around the recirculation zone and the mixing layer, which is the area of interest in this study. To discretise mixture fraction space, 51 cells were used, clustered around the stoichiometric mixture fraction.

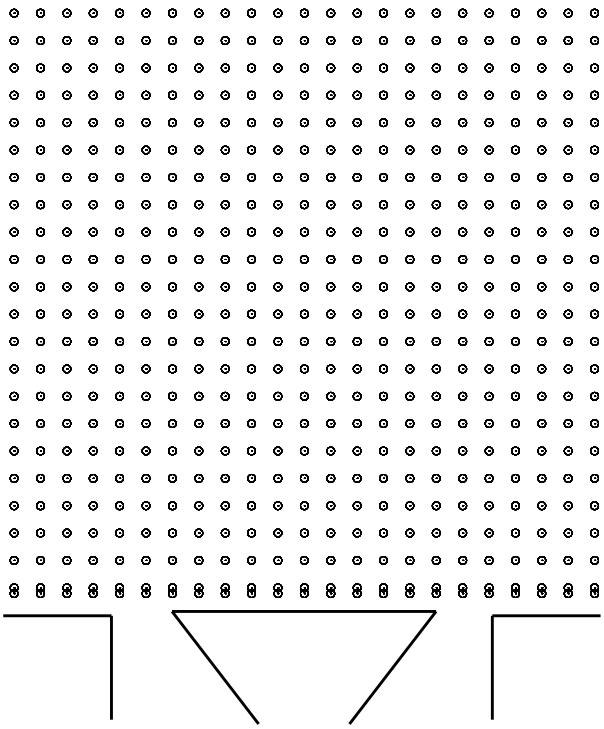

Figure 5.15: CMC mesh used in the ignition simulations. Area shown is $50 \times 50\,\mathrm{mm}$.

Table 5.2: Parameters of the ignition simulations (all dimensions in mm). Cases RS1 and RS1-repeat differ only in the initial condition. The fine mesh was used for all the simulations.

Case	Spark location (x, y, z)	Successful ignition?	Chem. mech.
RS1	9.375, 8.75, 0	Yes	Single step [7]
RS1-repeat	9.375, 8.75, 0	Yes	Single step [7]
RD1	9.375, 8.75, 0	Yes	16-species [8]
RS2	1.125, 8.75, 0	Yes	Single step [7]
RD2	1.125, 8.75, 0	Yes	16-species [8]
RD3	9.375, 8.75, 0	No	16-species [8]

5.6.2 Parametric studies and computational time

The ignition simulations presented in this chapter are summarised in Table 5.2. The fine LES mesh was used for all the ignition simulations. Six simulations were performed, which have different levels of complexity (the single-step chemical mechanism is used in cases RS1, RS1-repeat and RS2 and the detailed 16-species mechanism in cases RD1, RD2 and RD3), but also have different spark parameters; in cases RS1, RS1-repeat, RD1 and RD3, the spark is located in the shear layer, while in cases RS2 and RD2 it is located in the recirculation zone. Furthermore, the spark size in case RD3 is smaller than in all the other cases. The initial snapshot at which the spark is initiated is different in cases RS1 and RS1-repeat, in order to examine qualitatively the repeatability of the observed behaviour.

The conditions inside the spark at the moment of ignition ($t = 0$) are summarised in Table 5.3. Except for case RD3, where the spark occupies a single CMC cell, the spark in the other cases spans many CMC ($2 \times 2 \times 3$) and LES cells. In real dimensions, in RD3 the spark is $2.25 \times 2.25 \times 2.25$ mm, while in the other cases it

Table 5.3: Conditions inside the spark for the different ignition cases. The unconditional scalar dissipation rate $\widetilde{N}_{CMC}$ is given in s^{-1} and the velocities $\widetilde{u}_{CMC}$, $\widetilde{v}_{CMC}$ and $\widetilde{w}_{CMC}$ in m/s. See eq. (2.68), (2.51) and (2.61) for definitions of the quantities with a * superscript. Size of spark in all ignition cases is $4.5 \times 4.5 \times 6.75$ mm except in case RD3 where it is $2.25 \times 2.25 \times 2.25$ mm.

	RS1, RD1	RS1-repeat	RS2,RD2	RD3
No. of CMC cells	12	12	12	1
No. of LES cells	7329	7329	9758	538
$\widetilde{\xi}^*$	0.004 : 0.080	0.051 : 0.142	0.077 : 0.090	0.075
$\widetilde{N}^*$	0.065 : 7.25	1.23 : 8.73	0.047 : 0.330	4.46
$\widetilde{u}^*$	−6.53 : 8.50	−4.46 : 2.20	−13.07 : 1.84	−3.87
$\widetilde{v}^*$	16.05 : 19.79	0.36 : 7.10	−12.5 : −6.44	2.57
$\widetilde{w}^*$	−4.74 : 0.48	−6.74 : 6.32	−1.39 : 0.78	−3.88

is $4.5 \times 4.5 \times 6.75$ mm. When the spark is located in the shear layer (RS1, RD1 and RS1-repeat), the variation of the mixture fraction $\widetilde{\xi}_{CMC}$ and the scalar dissipation rate $\widetilde{N}_{CMC}$ is much greater than when the spark is located in the centre (RS2 and RD2). This is because the mixture fraction field is more uniform in the CRZ than in the shear layer, and therefore the gradients of $\widetilde{\xi}$ are much smoother. In RS1, RD1 and RS1-repeat, the axial velocity is positive and high, while in RS2 and RD2 it is negative and high (as expected since in the former cases the spark is located in the shear layer, while in the latter ones the spark is inside the CRZ). Cases RS1 and RS1-repeat have very different initial conditions. The mixture is richer in RS1-repeat and the variation of the axial velocity inside the spark is much greater.

All the simulations were performed in parallel on 16 dual-core processors. Each processor is an AMD 2.8 GHz Opteron with 3 GB of memory. When using the fine grid, for 1 ms of simulated time 350 min were required for the inert flow, 440 min for the ignition simulations when the single-step chemistry was used and 560 min when the detailed 16-species chemical mechanism was used. Typically, when the

detailed mechanism is used, approximately 50% of the time is spent solving the CMC equations and calculating the unconditional density and temperature and 50% is spent on the LES solver.

5.6.3 Effect of chemical mechanism

In order to visualise the evolution from a small hot gas kernel to the fully-burning flame, iso-surfaces of heat release rate Q will be presented. Three values for Q will be used: a low value ($Q = Q_l = 0.16\,\mathrm{MJm^{-3}s^{-1}}$), a medium value ($Q = Q_m = 65\,\mathrm{MJm^{-3}s^{-1}}$) and a high value ($Q = Q_h = 485\,\mathrm{MJm^{-3}s^{-1}}$). These correspond to 8%, 32% and 240% respectively of the peak heat release rate of a steady laminar flame calculated by a stand-alone, 0D-CMC calculation for $N_0 = 5\,\mathrm{s^{-1}}$ (see eq. (2.39)). Snapshots through an $x - y$ ($z = 0$) plane will also be shown. The comparison with experiment [11] is done on a qualitative basis based on visualisations and images of OH at various times because the experiment did not give a well-defined quantity that can be used to denote the end of the ignition transient and hence the speed of flame expansion cannot be validated in detail. However, a comparison with the global OH^* chemiluminescence emission observed experimentally is attempted.

5.6.3.1 Spark in the shear layer (RS1 and RD1)

Iso-surfaces of heat release rate ($Q = Q_m$) at different times from the moment of ignition, for cases RS1 and RD1 are shown in Fig. 5.16. Both simulations began from the same initial condition at time $t = 0$. In both cases (i.e. when using single-step and detailed chemistry), the flame is initially convected in the axial direction under the effect of the high axial velocity and only later it expands in the radial and azimuthal directions. This behaviour is more pronounced in case RD1, where the whole branch of the flame starts burning before it starts expanding in the other directions. The pattern of the flame expansion will be discussed in more detail in section 5.6.4.

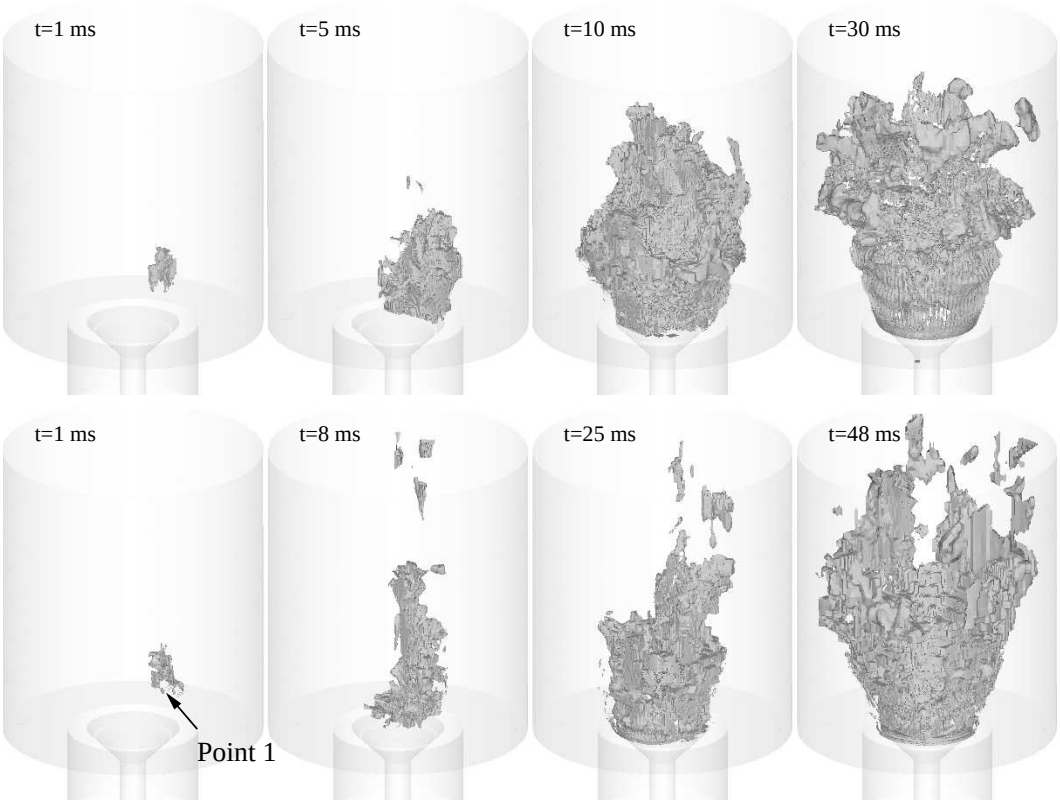

Figure 5.16: Iso-surfaces of heat release rate $Q = Q_m = 65\,\mathrm{MJm^{-3}s^{-1}}$, cases RS1 (top) and RD1 (bottom).

The time for the flame to cover the whole burner depends on the complexity of the chemical mechanism. For the single-step chemistry case (RS1), this time was approximately 25 ms, while for the case with the detailed chemistry it was approximately 40 ms. It is noted that in the experimental study, it took approximately 40 to 50 ms for the flame to stabilise (based on fast cinematography). The over-prediction of the expansion rate of the flame in the case of the single-step chemistry can be explained by the fact that generally, the single step mechanism predicts higher temperatures than the 16-species mechanism. Indeed, in Fig. 5.17 the conditional temperature at a point in the shear layer ($x = 13.16$ mm, $y = 12.85$ mm, $z = 0$) is shown using the two mechanisms at a moment in time when macroscopically the two flames look similar. Compared to the 16-species mechanism, the single step chemistry predicts a higher temperature in the region near stoichiometric where reaction takes place and a lower one at rich mixtures. This is consistent with Fig. 3.11, where for the same value of the scalar dissipation rate, the single-step mechanism produces higher temperatures than the 16-species mechanism. These higher temperatures lead to a faster expansion of the hot products and therefore to a faster flame propagation.

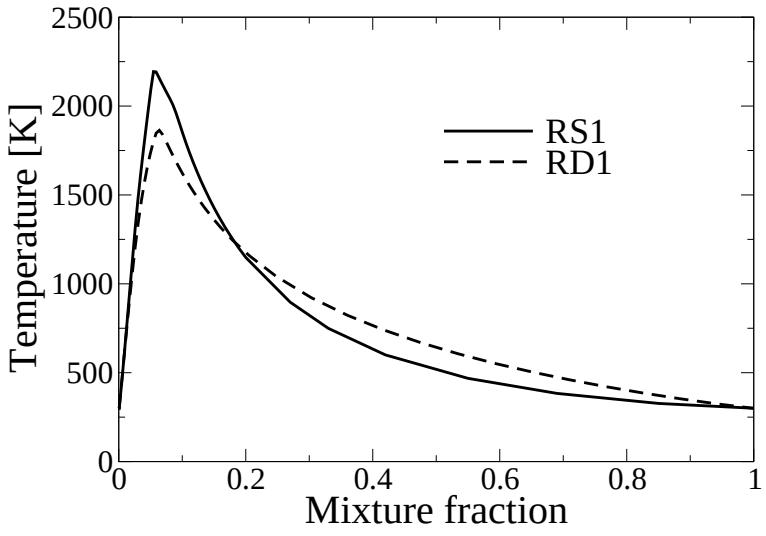

Figure 5.17: Conditional temperature at Point 1 ($x = 13.16$ mm, $y = 12.85$ mm, $z = 0$, see Fig. 5.16) at time $t = 25$ ms for case RS1 and $t = 35$ ms for case RD1.

5.6.3.2 Spark in the CRZ (RS2 and RD2)

The evolution of the flame in terms of iso-surfaces of the heat release rate for cases RS2 and RD2, where the spark is located in the central recirculation zone, is shown in Fig. 5.18. The hot gases move initially towards the bluff-body, driven by the negative axial velocity in the recirculation zone, and then towards the shear layer to finally cover the whole burner after approximately 30 ms. In the case where detailed chemistry is used (case RD2), a slower expansion of the flame is found: it takes approximately 50 ms for the flame to seem to be fully ignited. At about 20 ms, the flame seems to be as large as from the experimental images (e.g. compare Fig. 5.18, 21 ms with Fig. 15 of Ref. [11], 20 ms). The heat release rate is relatively low in the initial stages of the flame expansion, in accordance with experimental findings, where the flame is invisible (i.e. with luminosity lower than the camera's detection limit) during the stage when the flame expands inside the recirculation zone and only later does it become visible when it expands to the shear layer where stoichiometric ξ is found [11]. The flame expansion in case RD2 will be discussed in more detail in section 5.6.4.

5.6.4 Effect of spark location (RD1 and RD2)

In order to show more details of the flame expansion process depending on the spark location, contour plots of unconditional reacting scalars will be used. Plots of resolved temperature, $\widetilde{Y}_{OH}$, $\widetilde{Y}_{CH_4}$ and $\widetilde{Y}_{CH_2O}$ on a $z = 0$ plane are shown in Fig. 5.19 and 5.20 for cases RD1 and RD2 respectively at different times from the moment of ignition.

In case RD1, where the spark is located in the shear layer, the flame moves initially in the downstream axial direction, driven by the high axial velocity. After this initial stage, the flame moves towards the central recirculation zone (see images at t=3 and 6 ms) and then follows the negative velocity there that brings the flame towards the bluff body. Finally, after approximately 28 ms, the flame has expanded

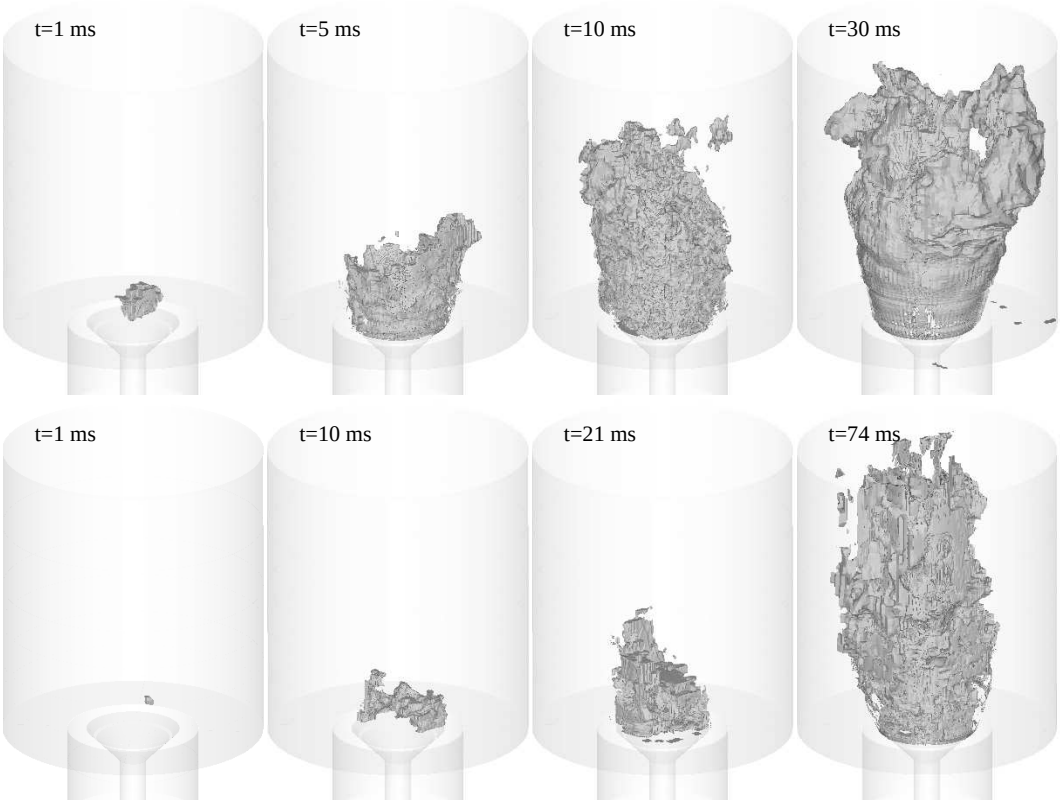

Figure 5.18: Iso-surfaces of heat release rate $Q = Q_m = 65\,\mathrm{MJm^{-3}s^{-1}}$, cases RS2 (top) and RD2 (bottom).

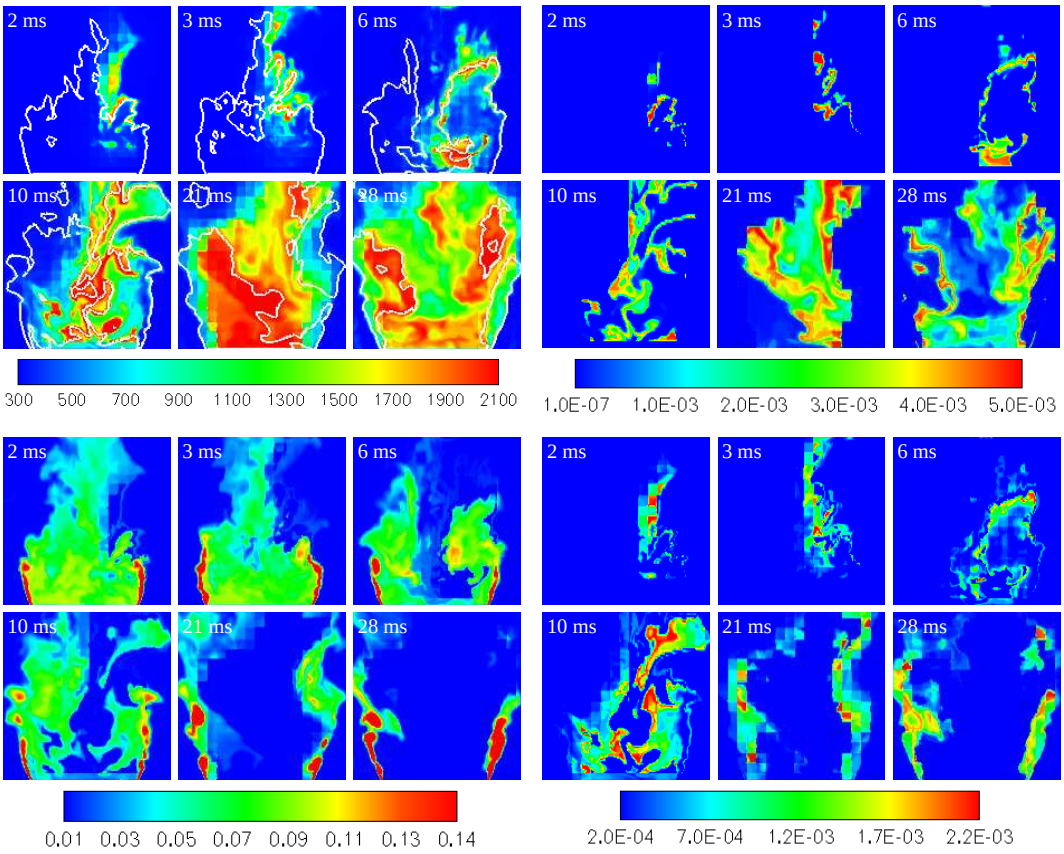

Figure 5.19: Contours of temperature (top left), $\widetilde{Y}_{OH}$ (top right), $\widetilde{Y}_{CH_4}$ (bottom left) and $\widetilde{Y}_{CH_2O}$ (bottom right) at different times from the moment of ignition (noted on the top left corner of each picture), case RD1. Solid white line at the top left graph: stoichiometric mixture fraction. Size of each image is 40×40 mm.

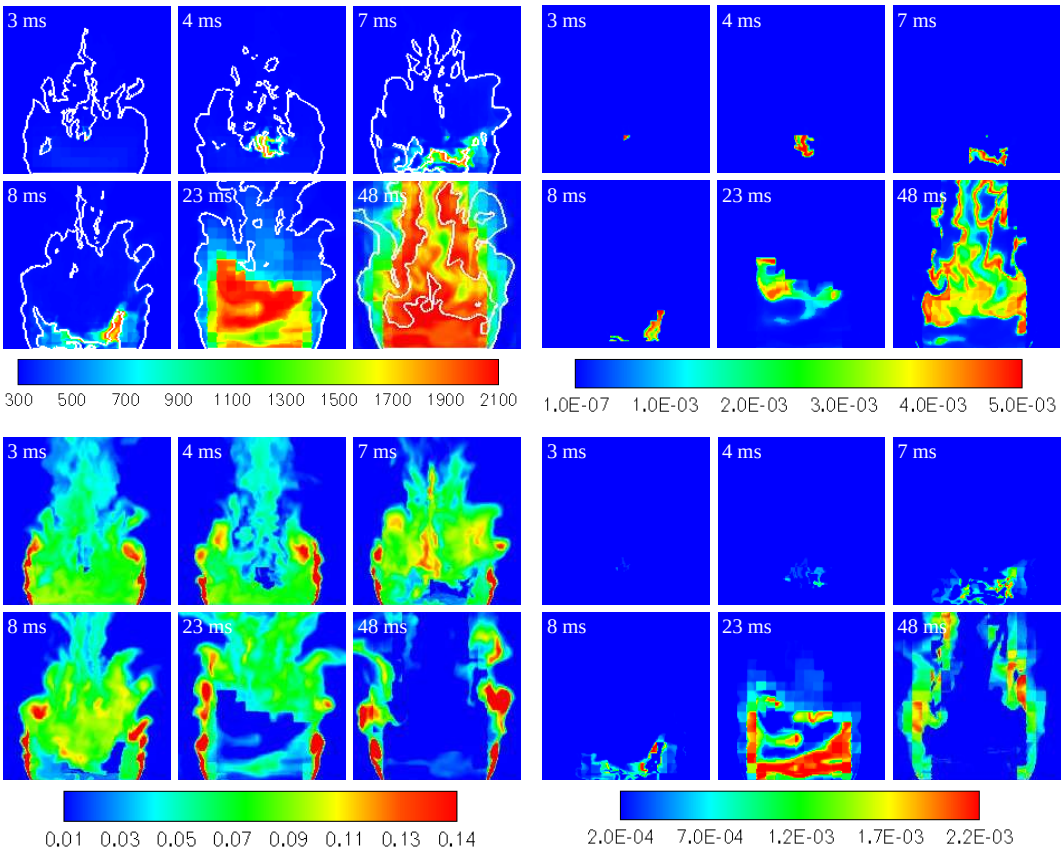

Figure 5.20: Contours of temperature (top left), $\widetilde{Y}_{OH}$ (top right), $\widetilde{Y}_{CH_4}$ (bottom left) and $\widetilde{Y}_{CH_2O}$ (bottom right) at different times from the moment of ignition (noted on the top left corner of each picture), case RD2. Solid white line at the top left graph: stoichiometric mixture fraction. Size of each image is 40×40 mm.

and has covered the whole CRZ. As the flame expands inside the recirculation zone (for example at times $t = 3 - 10\,\text{ms}$) the flame front (visualised by $\widetilde{Y}_{OH}$) is following a pre-heat zone, which is apparent by the presence of $\widetilde{Y}_{CH_2O}$. Formaldehyde seems to lie more in rich mixture fractions, as expected also from the stand-alone simulations of Fig. 3.15. When the flame front passes through the CRZ, all the fuel that was initially present is consumed, leaving the recirculation zone bare of reactants and full of hot combustion products (e.g. $t = 21\,\text{ms}$). The flame seems to expand quickest inside the recirculation zone when it follows the highly-contorted stoichiometric mixture fraction line, where the reaction rate is high (e.g. $t = 3 - 10\,\text{ms}$), but seems to take a longer time to expand *across* mixture fraction iso-lines (e.g. from $t = 10\,\text{ms}$ to $t = 21\,\text{ms}$).

Initially the mixture in the CRZ is rich. The closed stoichiometric mixture fraction contour that surrounds the CRZ is 'broken' by the flame and stoichiometric mixture enters the CRZ bringing the flame with it. However, once the flame is inside the CRZ, the recirculation zone expands and the ξ_{st} iso-surface is now inclined at a wider angle from the vertical (see image at $t = 28\,\text{ms}$).

In case RD2 (Fig. 5.20), where the spark is located in the central recirculation zone, the flame initially expands towards the bluff-body, driven by the negative velocity in the recirculation zone (e.g. see images from $t = 3\,\text{ms}$ to $t = 8\,\text{ms}$). Then, it moves towards the shear layer. After it has reached the shear layer, it re-enters the recirculation zone and the whole burner is filled with hot gases after approximately 50 ms. This evolution is fully consistent with experimental data (see, for example, Fig. 18 of Ref. [11]).

The flame front is preceded by a pre-heat zone in which formaldehyde is created in the rich and cold part of the flame. The post-flame region is devoid of fuel and formaldehyde and has high OH and temperature (see, for example, the images at $t = 23\,\text{ms}$). Eventually, the whole CRZ is hot and containing OH, with a relatively thick zone of formaldehyde in the rich part of the stoichiometric iso-line (i.e. towards the CRZ rather than the annular cold air layer).

It is evident from Figs. 5.19 and 5.20 that the concentration of OH in the recirculation zone is very 'patchy' during the expansion of the flame. A very similar observation has been made in the experimental study of this problem (see Fig. 18 of Ref. [11]). During flame expansion, at a given instant, there are parts of the CRZ where the flame has expanded, with the distribution of Q_α (conditional reacting scalars, see section 2.3.2) corresponding to a burning condition. There are also regions that the flame has not reached yet and there the distribution of Q_α corresponds to a non-burning condition. Moreover, in some parts of the CRZ the distribution of Q_α corresponds to an intermediate level, for example the pre-heat zone. This co-existence of different Q_α causes sharp gradients of species, especially in the case of species such as OH that only exist when the reaction rate is high and for a small range of mixture fractions. After the flame has expanded (for example $t = 28\,\text{ms}$ in Fig. 5.19), the concentration of OH is more uniform and the gradients are less steep. These gradients are present mainly because of the fluctuations of the mixture fraction, with the Q_α everywhere in the CRZ and at most locations in the shear layer corresponding to fully-burning distributions.

Contour plots of temperature in a horizontal plane ($y = 15\,\text{mm}$) for case RD1 are shown in Fig. 5.21. The flame moves initially towards the recirculation zone, assisted by the radial velocity fluctuations. While the recirculation zone is heating up, there is little expansion in the azimuthal direction; the flame must traverse the CRZ to reach the other side of the burner. When the whole of the CRZ is burning, the volumetric expansion is evident by the larger radius of the ξ_{st} contour.

5.6.5 Flame expansion (RD1)

In order to determine which transport term in the CMC equation dominates the expansion of the flame and what effect the different models for the integrated diffusivity have (eq. (2.64) and (2.63)), the following numerical experiments were performed: (i) Eq. (2.63) was used to provide the diffusivity ($D_t^* = D_{t_1}$), as opposed to Eq.

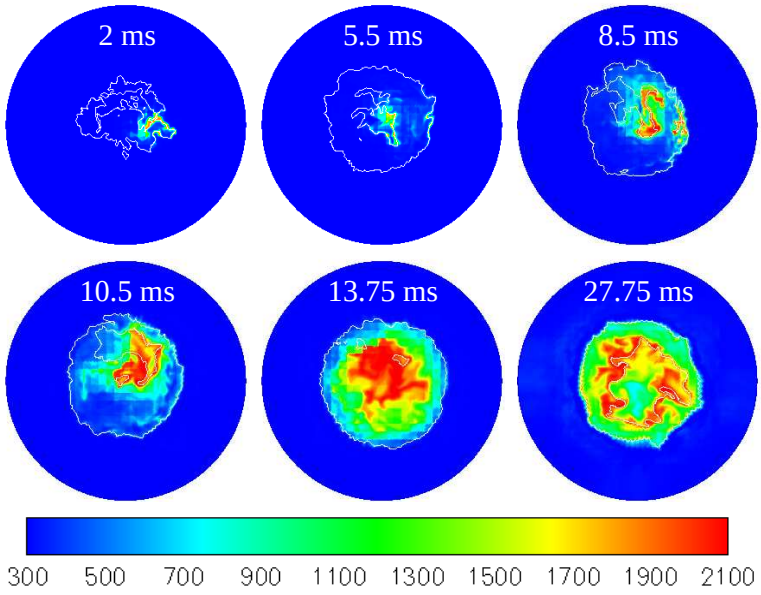

Figure 5.21: Contours of temperature at different times from the moment of ignition (noted on the top left corner of each picture) on the $y = 15\,\text{mm}$ plane, case RD1. Solid white line: stoichiometric mixture fraction.

(2.64) ($D_t^* = D_{t_2}$) which is used in all the other simulations and (ii) the term that accounts for diffusion in physical space (term T4 in Eq. (2.28)) was de-activated. These two simulations started at the same time instant ($t = 6\,\text{ms}$ in RD1) and the flame expansion was monitored closely for 0.8 ms (Fig. 5.22). At first glance the results look similar; none of the flames extinguishes or expands at a much higher rate than the others. At closer inspection, however, there seem to be some differences, especially when D_{t_1} (middle row) and D_{t_2} (top row) are compared. To further investigate these differences, focus is given to a small region (white box in top left image of Fig. 5.22) of the flow (Fig. 5.23). When the term T4 is included (red or blue lines lines) the solution is, as expected, more diffused. There are significant differences between D_{t_1} (blue lines) and D_{t_2} (red lines). Note that this analysis is based on instantaneous slices of a three-dimensional simulation and therefore cannot be used for detailed validation. Nevertheless, the effect of the different models is

pointed out and there is no attempt to draw any detailed conclusions.

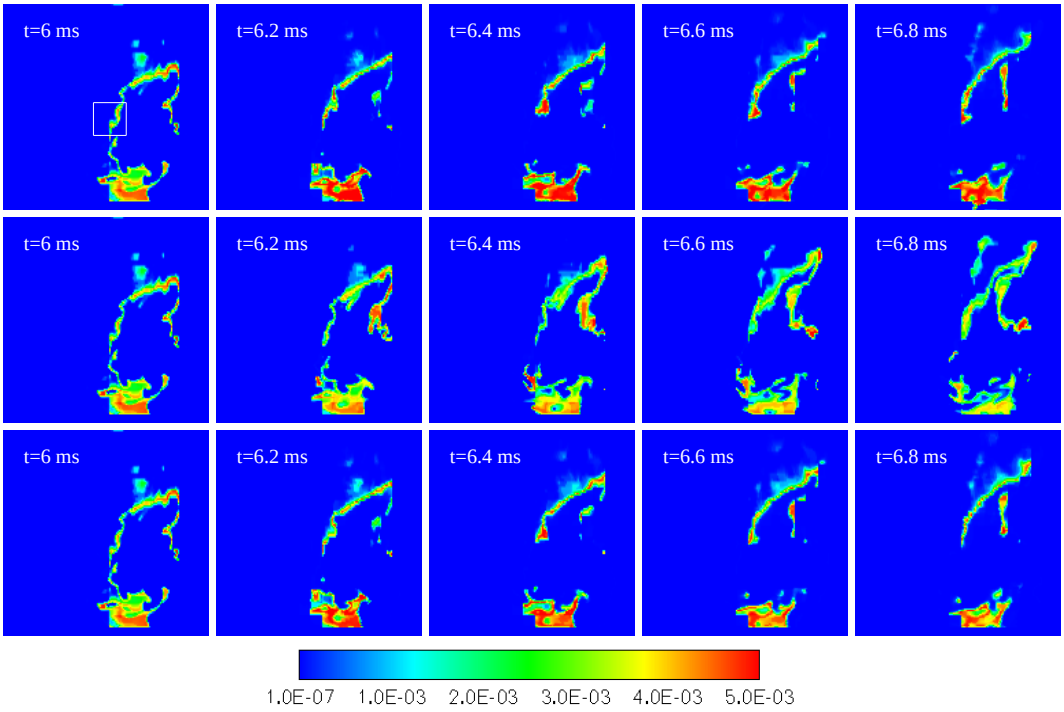

Figure 5.22: Contours of $\widetilde{Y}_{OH}$ at close intervals at the stage of the flame expansion using D_{t_2} (Eq. (2.64)) (top), using D_{t_1} (Eq. (2.63)) (middle) and without the effect of diffusion (term T4 in Eq. (2.28)) (bottom), case RD1.

Figs. 5.22 and 5.23 provide evidence that although the diffusion term may not be as critical for the expansion of the flame as the convection term in this configuration, it may still be important and some validation of this term against detailed experimental or DNS data should be made in the future.

5.6.6 Global heat release rate

The total heat release rate (i.e. integrated over all computational cells) for all the different successful ignition cases as a function of time is shown in Fig. 5.24. The total chemical enthalpy flow rate at the inlet is also shown (straight dashed line), calculated as the product of the fuel mass flow rate and the fuel lower calorific

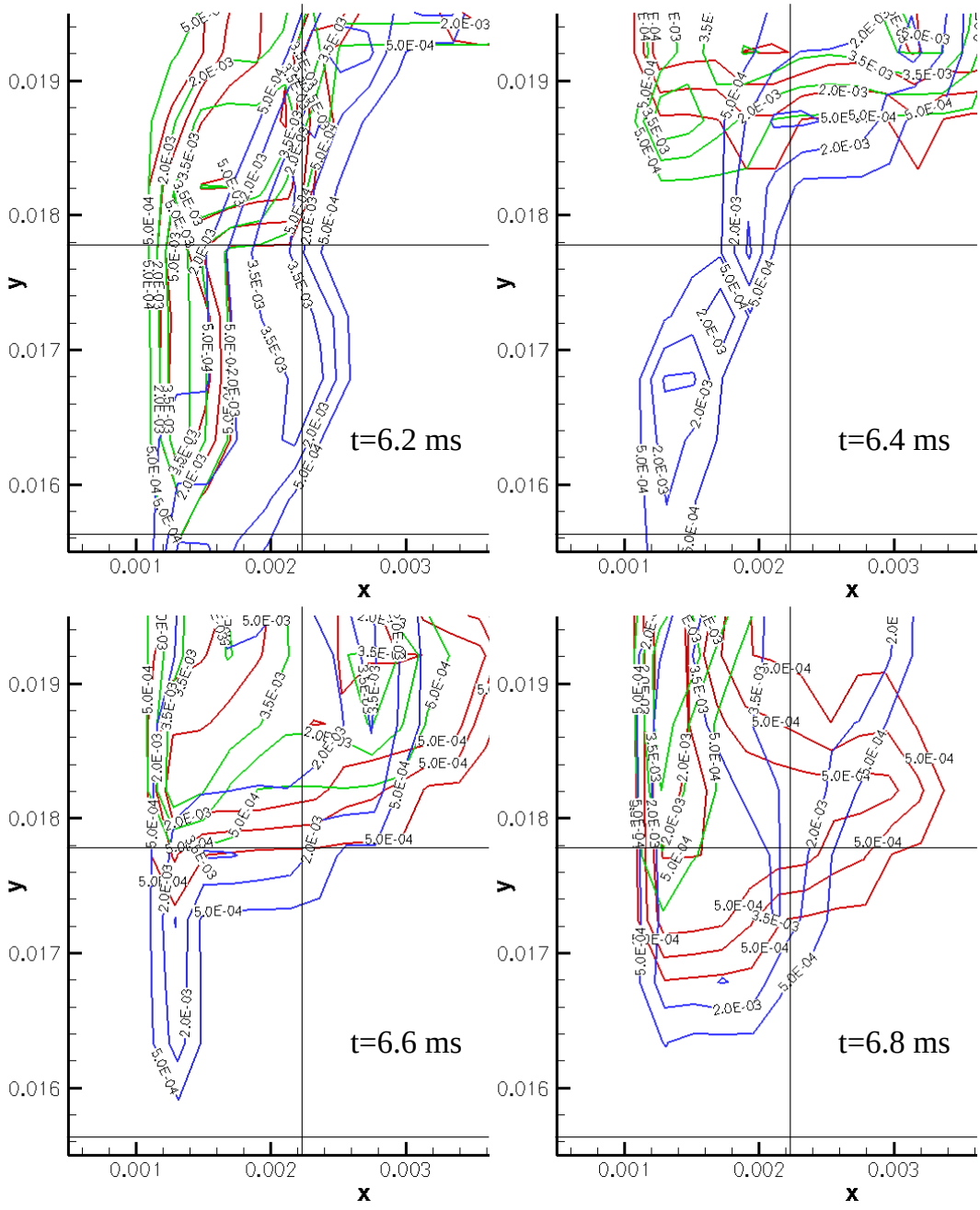

Figure 5.23: Line contours of $\widetilde{Y}_{OH}$ using D_{t_2} (Eq. (2.64)) (red lines), using D_{t_1} (Eq. (2.63)) (blue lines) and without the effect of diffusion (term T4 in Eq. (2.28)) (green lines), case RD1. The solid black lines represent the CMC grid. Image shown is equal to the white square on the top left image of Fig. 5.22.

value $Q_{total} = \dot{m}_f \times LCV$. Finally, from experiment, the global emission of OH^* chemiluminescence when the spark is located in the shear layer (as in RS1, RS1-repeat and RD1), is shown. The chemiluminescence can be used to give a measure of the total heat release rate and the curve shown is an average over many successful ignition events. More information about the way it was measured can be found in Ref. [12]. Note that this measurement can only be used in a qualitative manner, as chemiluminescence in non-premixed situations is not necessarily proportional to the heat release rate.

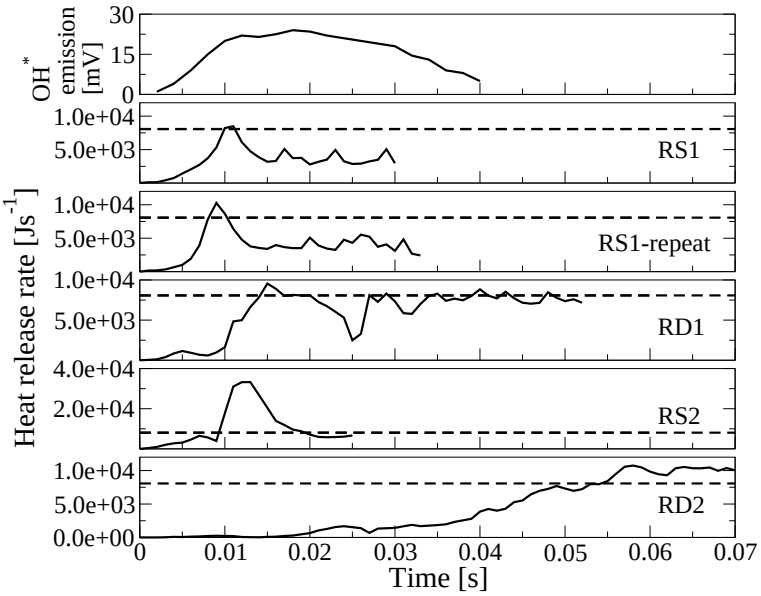

Figure 5.24: Total heat release rate for the different ignition cases and experimental data for OH^* emission when the spark is located in the shear layer; data from Ref. [12]. Straight dashed line is the total chemical enthalpy flow rate at the inlet ($Q_{total} = \dot{m}_f \times LCV$).

In cases RS1, RD1, RS1-repeat and RS2, the heat release rate gradually increases until at some moment in time (different for every simulation) and the heat release rate increases rapidly. This happens at about 10 ms for the spark in the shear layer, which corresponds approximately to the time when the flame has travelled through

the CRZ (compare with Fig. 5.19). After this peak, it decreases and stabilises around a constant value. In RS1 and RS1-repeat, the peak in the reaction rate occurs before it does in RD1 and lasts for a shorter period of time (approximately 5 ms compared to 15 ms in RD1). Cases RS1 and RS1-repeat exhibit a similar behaviour, which demonstrates that despite the differences in the initial condition, the global expansion mechanism is approximately the same. Comparison of case RD1 with the experimental curve shows that the time for which the heat release rate assumes high values is predicted with reasonable accuracy. In the experimental study it lasts for approximately 15 ms (from $t = 10$ ms to 25 ms), while in case RD1 it lasts for approximately 12.5 ms (from $t = 12.5$ ms to 25 ms). At $t = 25$ ms there is a short decrease in the heat release rate, before it reaches a constant value at $t = 27$ ms around which it fluctuates. This is a quantitative demonstration that the global process of flame expansion is captured with reasonable accuracy.

In RS2, the peak of the heat release rate is one order of magnitude higher than in all the other simulations. It is predicted that all the fuel in the recirculation zone is consumed very quickly, leading to a very high global heat release rate. In RD2, the heat release rate increases gradually until it reaches Q_{total} around which it fluctuates. The single-step chemical mechanism predicts reaction zones that are wider in mixture fraction space. This keeps the temperature high even for the relatively rich mixture in the recirculation zone. To demonstrate this, the conditional chemical source term for $\widetilde{Y_{H_2O}|\eta}$ and the conditional temperature in the location of the spark, 5 ms after ignition are plotted in Fig. 5.25. In RS2, the chemical source term 'covers' more values of ξ than in RD2. Consequently, the temperature is higher for rich mixtures, as is the mixture in the recirculation zone. This explains why the fuel in RS2 is consumed quickly and the heat release rate exhibits a very large peak value, compared to the other cases.

After the initial transient of the flame expansion, the global heat release rate assumes a constant value and fluctuates around it. In cases RD1 and RD2, this value is very close to the fuel enthalpy flow rate at the inlet. Values smaller than

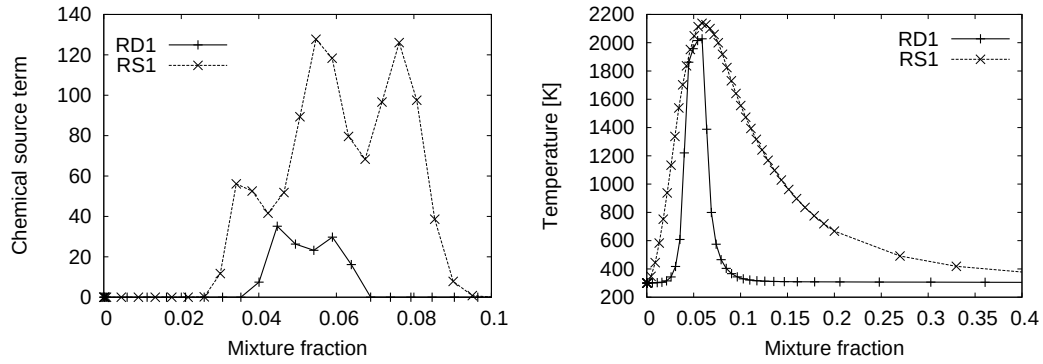

Figure 5.25: Chemical source term of the CMC equation (term T3 in eq. (2.28)) for $\widetilde{Y_{H_2O}|\eta}$ (top) and conditional temperature (bottom) at the location of the spark, 10 ms after ignition, cases RS2 and RD2.

Q_{total} imply that there is unburnt fuel at the exit of the burner. It is shown here that there seems to be little unburnt fuel exiting the burner. In the cases where the single-step chemical mechanism is used, this limit is not reached. This is due to the fact that the heat release rate is tuned to reproduce the premixed flame laminar burning velocities (see section 3.4) and therefore it is very low at rich mixtures, leaving some of the fuel unburnt.

The conclusion is that the overall pattern of flame expansion, for both spark locations, is very similar qualitatively to the experimental observations [11] and that overall better agreement is obtained with the detailed mechanism. For the case of the ignition inside the CRZ, the flame seems to take longer to establish than in the experiment (e.g. approximately 50 ms rather than about 30 ms in the experiment), while for ignition at the shear layer the time taken to ignite the whole flame is close to the experimental data. We also conclude that since the flame expansion process involves transitions from unburnt to burnt and reactions at a very wide range of mixture fractions and scalar dissipations, a full 3D combustion model, such as the present formulation of CMC, appropriate for all mixture fractions is necessary to capture ignition events in non-premixed combustion.

5.6.7 Effect of spark size

In RD3, a smaller spark is used. The location of the spark is identical to case RD1, but its volume is 12 times smaller. The evolution of the unconditional temperature is shown in Fig. 5.26. In the context of the CMC, heat is transported very quickly and eventually the spark is extinguished. The evolution of the conditional temperature at locations P1 (location of spark) and P2 (4.5 mm downstream of the spark) are shown in Fig. 5.27. At the location of the spark, the temperature decreases rapidly, since heat is transported to all the neighbouring cells through convection and diffusion. After approximately 0.5 ms, the temperature has fallen to levels corresponding to inert mixing ($\widetilde{T|\eta} \approx 300\,\mathrm{K}$). At P2, the temperature initially rises, since it receives heat from the spark location, but the maximum temperature that is reached ($\widetilde{T|\eta} \approx 400\,\mathrm{K}$ at time $t = 0.2\,\mathrm{ms}$) is not high enough to sustain a flame. After $t = 0.2\,\mathrm{ms}$, the temperature starts decreasing reaching the initial levels of $\widetilde{T|\eta} \approx 300\,\mathrm{K}$ after about 2 ms.

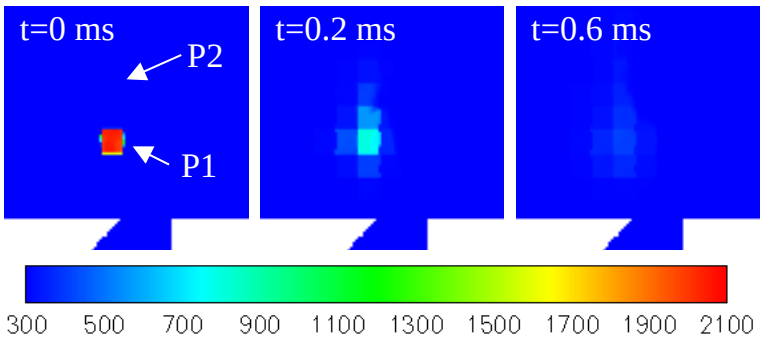

Figure 5.26: Contours of temperature at different times from the moment of ignition (noted on the top left corner of each picture), case RD3. Image size is 25×25 mm.

The flame is quenched because the rate with which heat is extracted from the spark region is higher than the rate at which heat is created. Heat is extracted through micromixing (via the scalar dissipation rate), convection and sub-grid scale turbulent diffusion (the two latter mechanisms can be collectively described as spa-

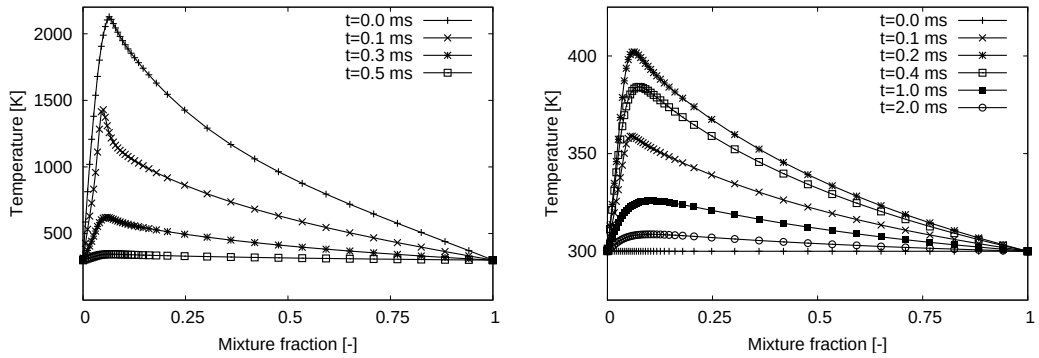

Figure 5.27: Evolution of the conditional temperature at locations P1 (top, location of spark) and P2 (bottom, 4.5 mm downstream of the spark, see Fig. 5.26), case RD3.

tial transport). The scalar dissipation rate in the case of this burner is very small; due to the initial mixing of fuel and air before the exit of the bluff-body, the gradients of ξ are small at the spark location and hence the scalar dissipation rate is small. Indeed at the spark position, $\widetilde{N} = 4.46\,\mathrm{s}^{-1}$ (see Table 5.3), which is one order of magnitude smaller than the extinction scalar dissipation rate, shown in Fig. 3.11. In order to demonstrate that this is a case of extinction through spatial transport, the balance of terms of the CMC equation for $\widetilde{Y_{H_2O}|\eta}$ in the location of the spark at $t = 0$ is shown in Fig. 5.28. The negative convection and diffusion terms dominate the only positive term (chemical reaction term) resulting to a very high negative right-hand-side of the CMC equation, which leads to the rapid transport of heat and species from the location of the spark and eventually to extinction.

The demonstration that a small spark results in a quenched ignition event is in qualitative agreement with the theory that a minimum ignition energy is required from the spark to start a flame [14]. In the context of these simulations, a low ignition energy may be translated to a small region of hot gases. It is demonstrated here that if the hot gases do not occupy a large enough region, the transport of heat and species is so strong, that the initial spark region extinguishes. The timescale

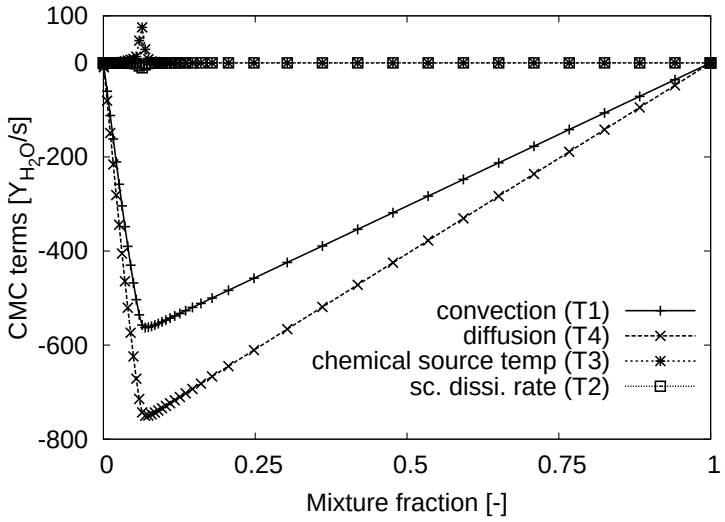

Figure 5.28: Balance of terms of CMC equation (eq. ((2.28))) for $\widetilde{Y_{H_2O}|\eta}$ at the location of the spark (P1 in Fig. 5.26) at time $t = 0$, case RD3.

for flame extinction is quicker than in the experiment: in Fig. 23 of Ref. [11] it is evident that kernels that do not eventually ignite the flame may survive for a few ms, while in the present simulations the kernel has disappeared after a maximum of 1 ms. The difference probably lies in the lack of adequate resolution in physical space in the CMC equation. It is evident, however, that the multidimensional CMC formulation includes the correct physics to predict spark failure.

5.7 Flame stabilisation

At a long time after ignition, the flame reaches a statistically-steady condition where the spatial gradients of Q_α are less steep than in the initial stages of flame expansion. This condition will be investigated in this section for cases RD1 and RS1. Recall that the simulation always has Q_α corresponding to a frozen condition (inert mixing) in η-space at the inlet of the burner.

Iso-surfaces of low ($Q = Q_l$) and high ($Q = Q_h$; see section 5.6.3 for definition of

Q_l and Q_h) heat release rate are shown for cases RS1 and RD1 in Fig. 5.29 for long times after ignition. The appearance of the flame is similar using both the single step and the detailed mechanism. The iso-surface for $Q = Q_l$ seems to be 'wider' than for $Q = Q_h$. The regions of lower heat release rate are further away from the bluff-body, where the mixture is leaner. The iso-surface for $Q = Q_h$ is very 'patchy' due to the fluctuations of the mixture fraction and of the scalar dissipation rate.

Contour plots of the time-averaged $\langle \widetilde{Y}_{OH} \rangle$ and $\langle \widetilde{Y}_{CH_2O} \rangle$, composed over a simulated time of 10 ms, starting at time $t = 38$ ms for case RD1, are shown in Fig. 5.30. The highest values of OH are located in the mixing layer, where ξ is close to its stoichiometric value, while there is also some presence of OH inside the recirculation zone. This image is very similar to the respective experimental image (Fig. 19 in Ref. [11]). Most of the CH_2O is located in the shear layer. Inside the recirculation zone, where $\xi < \xi_{st}$ and there are no cold reactants, there is no CH_2O.

In order to investigate the flame stabilisation mechanism, the conditional temperature from a series of CMC cells on a $z = 0$ plane for four distances from the bluff body is plotted in Fig. 5.31. Each graph corresponds to one axial location and each line on each graph corresponds to one CMC cell. For $y = 3$ mm, moving radially outwards from the centreline of the burner (which is located at $x = 0$), the shape of the conditional temperature changes from that corresponding to a flame (i.e. similar to that in Fig. 3.12 to 3.15) to that corresponding to an intermediate condition and then to the 'frozen' (i.e. inert) condition, which is the inlet condition at the entry to the burner. Moving away from the bluff body in the axial direction (y-direction), the conditional temperature gradually corresponds to that of a fully-burning flame everywhere except for the outer recirculation zone, where it takes longer for the Q_α to burn fully.

The conditional temperature, $\widetilde{Y_{OH}|\eta}$, $\widetilde{Y_{CH_4}|\eta}$, and $\widetilde{Y_{CH_2O}|\eta}$ for four locations in the stabilisation region (see Fig. 5.30) at $t = 40$ ms from the start of ignition are shown in Fig. 5.32. Point A is closest to the incoming inert flow and shows intermediate values of temperature, virtually zero OH, and some CH_4 transformation to CH_2O.

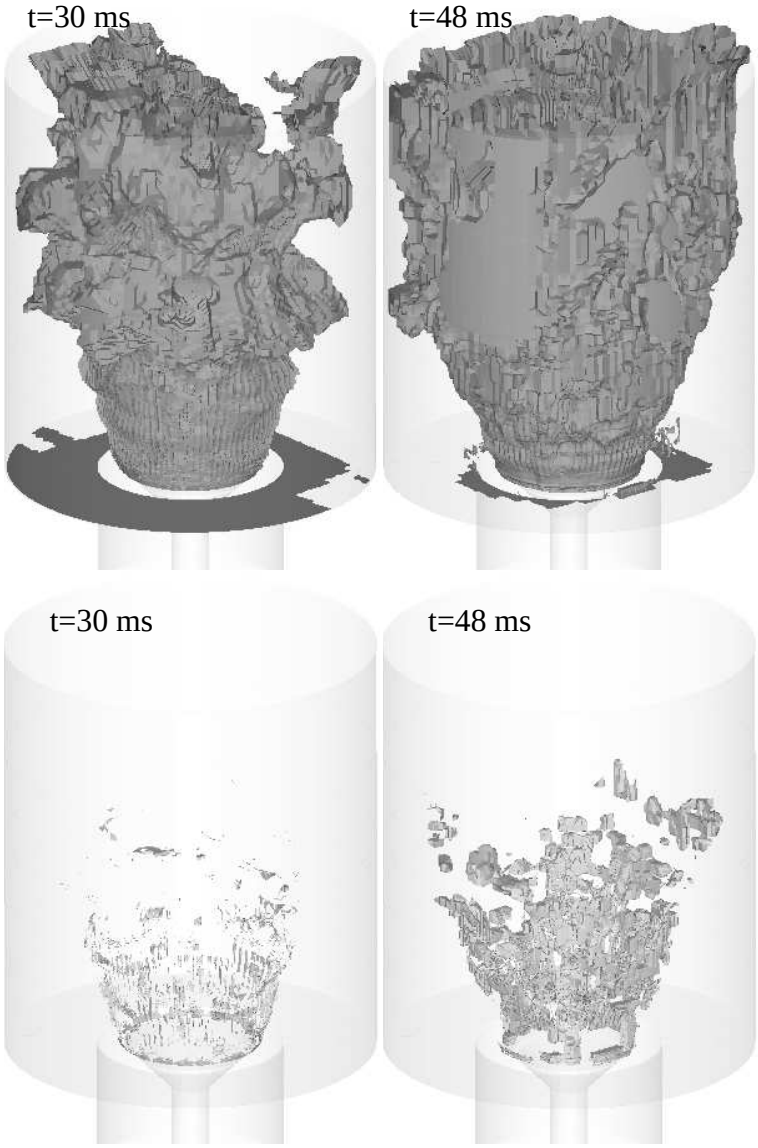

Figure 5.29: Iso-surfaces of low (top, $Q = Q_l = 0.16\,\mathrm{MJm^{-3}s^{-1}}$) and high (bottom, $Q = Q_h = 485\,\mathrm{MJm^{-3}s^{-1}}$) heat release rate for cases RS1 (left) and RD1 (right).

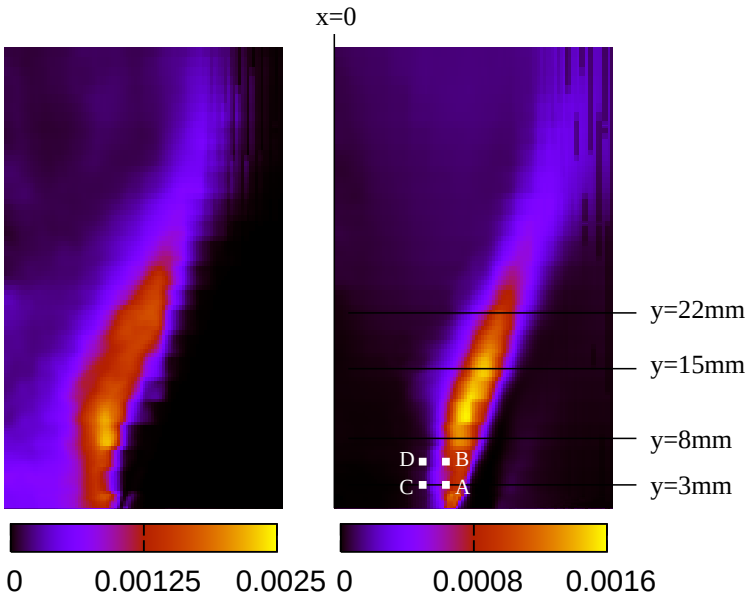

Figure 5.30: Contours of $\langle \widetilde{Y}_{OH} \rangle$ (left) and $\langle \widetilde{Y}_{CH_2O} \rangle$ (right), case RD1. Image size is $30 \times 50\,\mathrm{mm}$. Time-averaging was performed with data being collected over 10 ms starting from 38 ms after ignition.

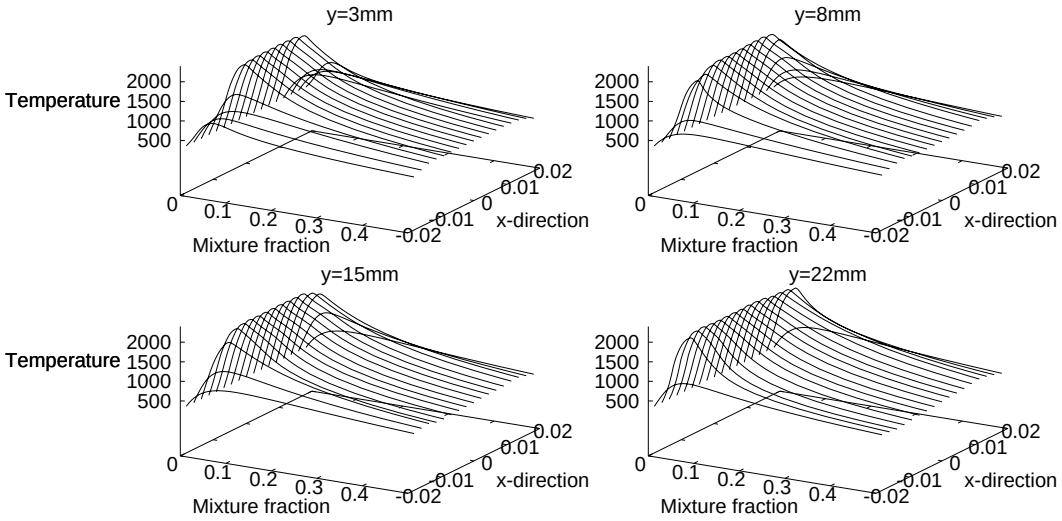

Figure 5.31: Conditional temperature in [K] on a $z = 0$ plane for four distances from the bluff body (see Fig. 5.30) at time $t = 40$ ms after ignition, case RD1. Each graph corresponds to one axial location and each line on each graph corresponds to one CMC cell.

Points C and D have distributions of a fully-burning nature (very close to Fig. 3.12 to 3.15). The distributions for Point B show that this point has approached the fully-burning state.

The relatively high temperature at the positions of intermediate condition is sustained by transport of heat and species from the recirculation zone and not by chemical reaction. This is demonstrated more clearly in Fig. 5.33, where the balance of terms of the CMC equation for $\widetilde{Y_{H_2O}|\eta}$ is shown at these four locations at the same time as for Fig. 5.32. The spatial diffusion terms (terms T1 and T4 in eq. (2.28)) at point C and D appear as sinks, while at point A they appear as a source. The chemical source term for $\widetilde{Y_{H_2O}|\eta}$ at A is negligible. There is no $\widetilde{Y_{OH}|\eta}$ and there is little consumption of fuel at point A. There is, however, presence of $\widetilde{Y_{CH_2O}|\eta}$, which demonstrates the fact that point A belongs to some form of pre-heat zone, before the stabilised flame appears at point B. At point B, the temperature is high and the flame is sustained by heat-releasing chemical reactions and hence the presence

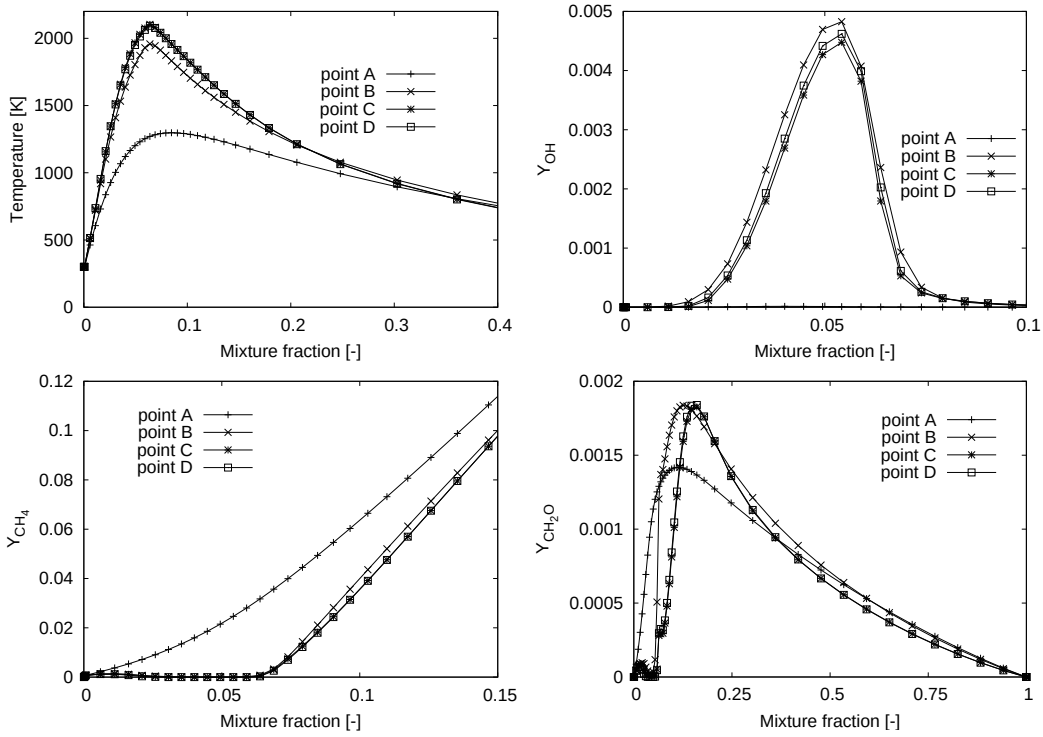

Figure 5.32: Conditional temperature (top left), $\widetilde{Y_{OH}|\eta}$ (top right), $\widetilde{Y_{CH_4}|\eta}$ (bottom left) and $\widetilde{Y_{CH_2O}|\eta}$ (bottom right) at locations A-D (see Fig. 5.30) at time $t = 40\,\mathrm{ms}$ after ignition, case RD1.

of $\widetilde{Y_{OH}|\eta}$ and the consumption of fuel. Point D is also fully burning and provides heat and radicals (through diffusion and convection) to the colder neighbouring regions. In the context of the multi-dimensional CMC model, flame stabilisation occurs through the spatial gradients of conditional quantities and clearly this cannot be predicted with integrated forms of the CMC. The structure of the base of the flame is similar to the stabilisation region of a lifted jet flame from CMC predictions [54] and experiments [131], suggesting a small lift-off height from the bluff body face.

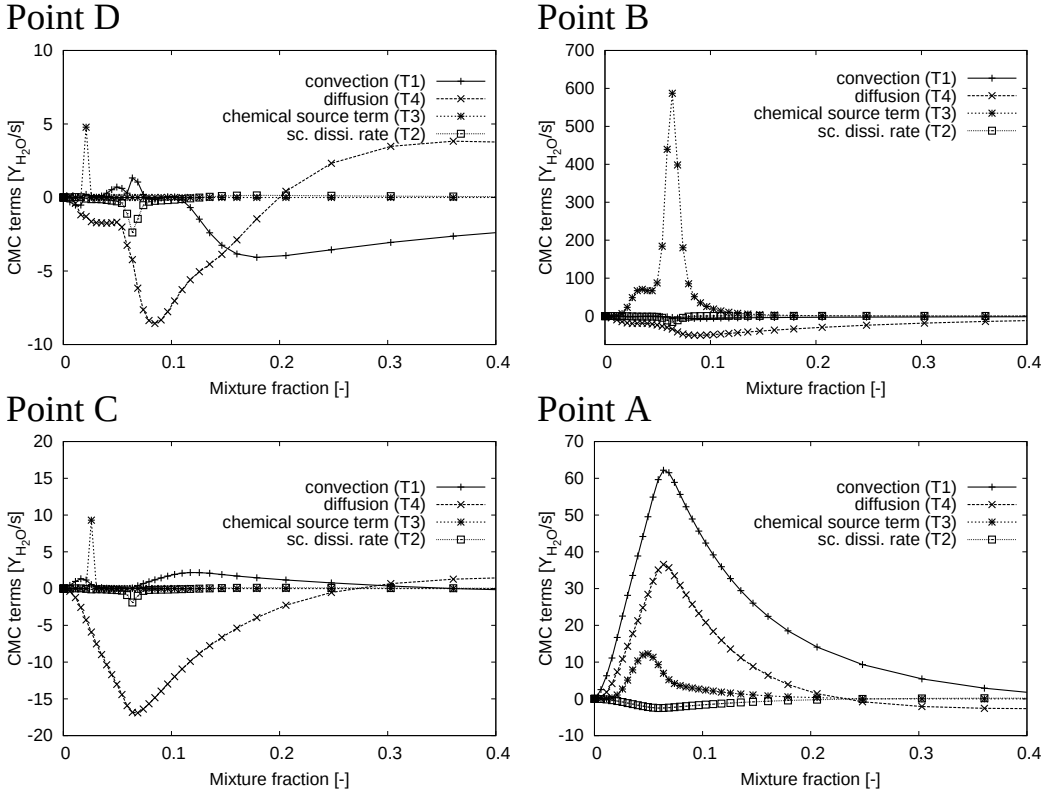

Figure 5.33: Balance of terms of CMC equation (eq. (2.28)) for $\widetilde{Y_{H_2O}|\eta}$ at locations A-D (see Fig. 5.30) at time $t = 40\,\mathrm{ms}$ after ignition, case RD1.

The present results are consistent with the intuition that a hot central recirculation zone (i.e. a fully burning Q_α distribution as in points C and D) is responsible for overall flame stabilisation. The diffusion and convection of heat and radicals

in the radial direction to the incoming inert Q_α distribution must be successful for the flame to ignite there, which will then result in burning distributions to be available inside the CRZ. The overall ignition of the burner necessitates enough time for physical transport to spread the burning Q_α distributions across the whole burner.

Finally, a simulation similar to the one presented in section 5.5 (in terms of the initial conditions) was performed, but this time the fine mesh was used. The comparison between the two flames can reveal the differences in the flame structure when the mixing field is different. Instantaneous contour plots of the axial velocity, the mixture fraction, the temperature and a number of species are shown in Fig. 5.34.

Comparing the velocity and mixture fraction fields with the ones from the inert flow (Fig. 5.6), it is obvious that due to the expansion of the hot gases in the recirculation zone, the angle at which the flow enters the burner has changed and the recirculation zone covers a bigger part of the burner than in the inert flow.

The mixture inside the recirculation zone remains well within the flammability limits and as a result the temperature remains reasonably high and indeed higher than in section 5.5 where the mixture was predicted to be richer (the normal mesh was used in section 5.5). The presence of OH in the recirculation zone and the consumption of fuel in the recirculation zone prove that there are chemical reactions taking place in that region, which is something that was not observed in section 5.5. Furthermore, the shape of the contour of $\widetilde{Y}_{OH}$ is similar to OH-PLIF images from Ref. [11]. The levels of CH_2O are low in the recirculation zone, but reasonably high in the shear layer and more specifically close to the bluff-body. Compared to section 5.5 (Fig. 5.10) there is much more CO_2, CO and H_2 in the recirculation zone, which can be related to the difference in the mixture fraction fields. The comparison between the two flames demonstrates how crucial it is to capture the mixing field for the correct prediction of the flame structure.

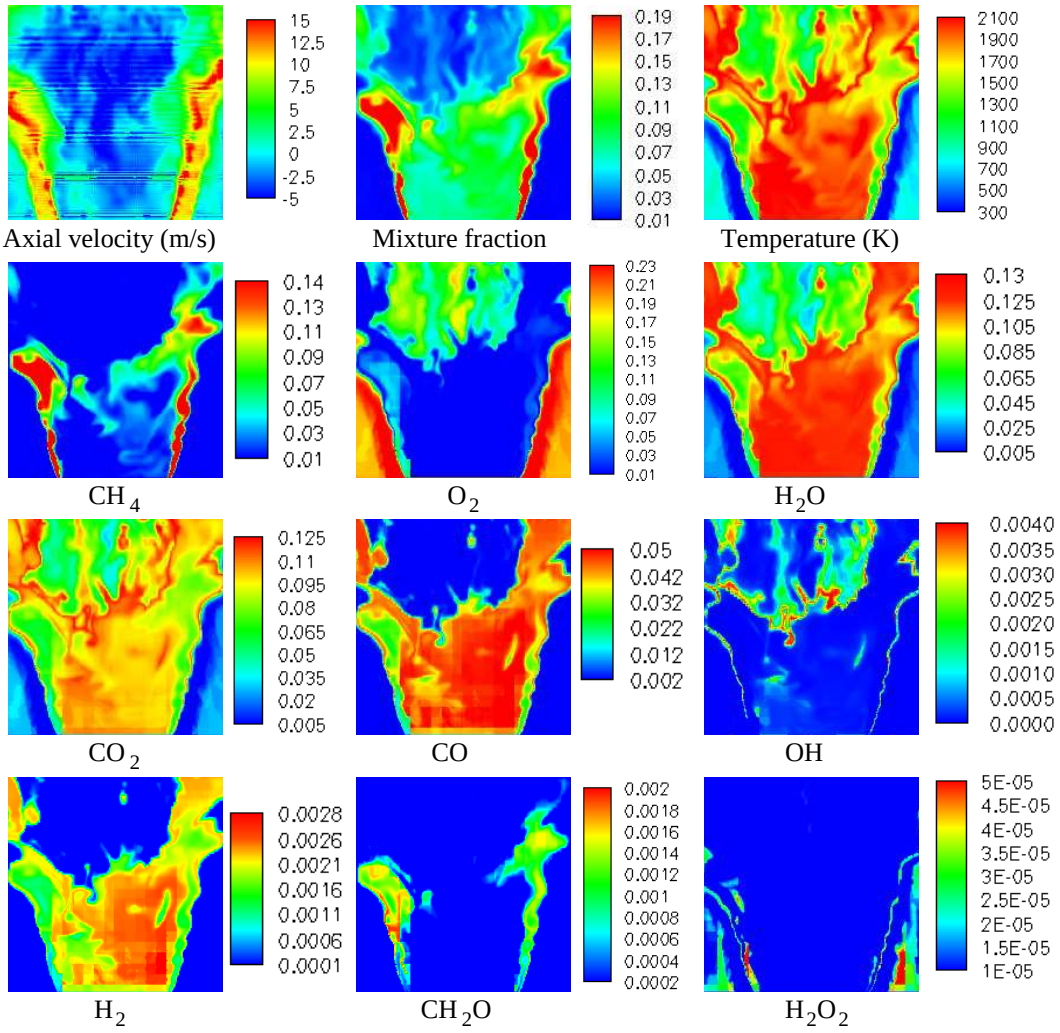

Figure 5.34: Instantaneous contours of axial velocity, mixture fraction, temperature and a number of species in the case of the statistically-steady flame. Size of images is $50 \times 50\,\mathrm{mm}$.

5.8 Conclusions

The CMC model has been applied to LES of forced ignition of a bluff-body stabilised non-premixed methane flame for which experimental data are available. Meshes of different resolution were used to simulate the inert flow. It was found that the velocity field was not sensitive to the resolution of the mesh and very good predictions were obtained even with a relatively coarse grid. The mixture fraction, however, was more sensitive to the resolution of the mesh and use of a very fine grid was required to predict its distribution accurately.

Preliminary results of the statistically steady flame showed that the different options for the integrated diffusivity presented in chapter 2 gave similar results. When using the diffusivity proposed from Eq. (2.64), the results are similar to using a volume-averaged diffusivity, with a slight difference in the lift-off height of the stabilised flame.

Ignition simulations using chemical mechanisms of different complexity showed that the global expansion of the flame could be predicted with reasonable accuracy. When a single-step chemical mechanism was used, it was found that the shape and the overall appearance of the flame were similar to the experimental findings, with the expansion rate being over-predicted by a factor of approximately 2. When the detailed mechanism was used, the expansion rate was predicted with greater accuracy. Moreover, the distribution of OH in the burner during the ignition transient and when the flame was stabilised was qualitatively consistent with experiment.

The manner in which the size and the location of the spark affect the flame expansion was also investigated. It was found that the pattern of the flame propagation and the time for the flame stabilisation depends on the location of the spark relative to the recirculation zone. If the spark is located close to the shear layer, the flame expands rapidly inside the recirculation zone and fills the recirculation zone with hot combustion products. If the spark is located inside the recirculation zone, the flame initially moves towards the bluff body, then to the shear layer and eventually

it re-enters the CRZ. If the spark is very small, transport of heat causes a rapid decrease of the temperature leading to extinction of the spark. At the same time, the increase of temperature in the neighbouring region is not high enough to cause ignition and a flame cannot be sustained.

At long times after ignition, the flame reaches a statistically steady condition where the spatial gradients of the conditional quantities vary slowly with time. Even in this fully-ignited state, the region very close to the inlet has distributions of the conditional quantities corresponding to the inert condition, showing a small lift-off distance from the bluff body. The transport of heat from the fully-burning CRZ to the cold gases that enter the burner is done by sub-grid scale turbulent diffusion and convection; indeed, these terms appear as sink terms in the CMC equation for locations inside the CRZ and as source terms for locations in the shear layer.

The results demonstrate that LES/CMC can reproduce successfully many of the features of recirculating non-premixed flame ignition from a hot kernel. Detailed chemistry seems to be necessary. Further work is needed for modelling accurately the spark and for more focused validation of the rate of the flame propagation process.

Chapter 6

Conclusions

This thesis describes research undertaken into the modelling of ignition and flame expansion in turbulent flows. This has been carried out using first-order Conditional Moment Closure (CMC) [44] in Large Eddy Simulations (LES) of flows of different complexity. The objectives of this thesis are to examine the feasibility of using an LES/CMC approach for ignition of non-premixed flames and to investigate the sensitivity of the predictions to parameters related to the spark and to the numerical setup.

The governing equations and the sub-models used in the literature and in this thesis were presented in chapter 2. Due to the high computational cost of the CMC method (a stiff system of five-dimensional partial differential equations, one for each species in the chemical mechanism must be solved), in the few LES/CMC calculations performed so far [45, 60–63] hypotheses have been made, depending on the nature of the studied flow, to reduce either the dimensionality of the CMC equation or the required resolution of the CMC mesh. The fact that the CMC equations would be solved on a different mesh than the LES, introduces issues regarding the exchange of information between the two meshes. Information about the flow is available in the LES resolution, but is required in the CMC resolution and the opposite is true about information concerning the reacting scalars. In order to transfer

information from one mesh to the other, some sort of volume averaging must take place. This averaging can be in terms of unconditional properties and the model to obtain the conditional properties would be applied in the CMC resolution, or in terms of conditional properties, where the model would be applied in the LES resolution and then volume-averaged. To assess the differences between the two options, detailed measurements of the mixture fraction in a turbulent plume were examined (taken from Ref. [100]), in the context of filtering using different filter sizes. The main conclusions of this study were that in order to have an accurate estimate of the sub-grid scale variance of the mixture fraction in the CMC resolution, the variation of the resolved mixture fraction within a CMC cell must be taken into account. In that case, a presumed shape for the FDF (filtered density function) may be used with reasonable accuracy. Furthermore, the model for the conditional scalar dissipation rate may be applied in either the LES or the CMC resolution (as long as the FDF is accurate) with very similar results. A model was also presented for the sub-grid scale diffusivity in the CMC resolution, where instead of a volume-averaging, the Smagorinsky model would be applied using the velocity filed in the CMC resolution. This model was tested in chapter 5 where, because of the dominance of the convection term, little difference was observed between this model and a simple volume-averaged sub-grid scale diffusivity.

6.1 Ignition of a flame in a shearless turbulent mixing layer

Forced ignition in a shearless planar mixing layer has been investigated (chapter 4). The configuration consisted of two turbulent streams of equal velocity (one carrying air one carrying fuel) that mix forming a turbulent mixing layer. Forced ignition simulations were performed and it was found that the expansion of the flame in the streamwise, but also in the spanwise direction (expansion along and across the flow)

was captured with reasonable accuracy, compared to experimental results. However, the flame was found to be 'anchored' in the spark location, contrary to experimental findings, where the flame would detach from the spark location and either propagate upstream (if the bulk velocity is low) or convect in the streamwise direction (at higher bulk velocities, similar to the velocity in the simulations). This may present a limitation of first-order CMC, as extinction of flamelets in the spark location is not captured. It is possible that second-order CMC may be able to capture this, since close to extinction, the variances and co-variances of the conditional averages may become important and therefore cannot be neglected.

Several simulations were performed, investigating the sensitivity of the predictions both to numerical aspects, but also to parameters related to the flow. It was found that the resolution of the CMC mesh is important for the prediction of the expansion of the flame across the flow. Even if the resolution in the spanwise direction was kept the same, altering the resolution in the transverse and in the streamwise direction resulted in a more realistic pattern of flame expansion. Another numerical parameter whose influence was investigated was the discretisation scheme for the convection term in the CMC equation. Predictions using the first-order upwind scheme, known to introduce significant amounts of numerical diffusion, and a TVD scheme were compared and it was found that the TVD scheme would retain the sharp gradients of the reacting scalars at the flame front. This, however, would come at a great computational cost. Furthermore, the flame 'anchoring' appeared in the results using the TVD scheme too. This led to the conclusion that the additional computational cost would counter-balance the higher accuracy of the TVD scheme and therefore the first-order upwind scheme was considered to be a reasonable discretisation scheme.

The expansion of the flame across the flow was found to be dominated by convection (i.e. resolved fluctuations of velocity). A simulation where the sub-grid scale diffusion term (term T4 in Eq. (2.28)) had been neglected resulted in predictions very similar to those where the diffusion term had been included. This may be true in the case of this configuration, but it may not be true in other problems (such

as a lifted flame) where sub-grid scale diffusion and convection may be of the same importance. The bulk velocity of the turbulent streams was also found to be an important parameter. It has been mentioned earlier in this section that the flame was found to be 'anchored' in the spark location. This 'anchoring' was found to disappear when the bulk velocity was increased.

6.2 Ignition of a bluff-body stabilised flame

Simulations of forced ignition of a bluff-body stabilised flame have been performed and presented in chapter 5. Although this configuration is simpler than a gas turbine combustor chamber, it has some of the characteristics encountered in real combustors, such as a recirculation zone for the stabilisation of the flame, and therefore could be considered as a good test-case for the feasibility of the CMC method in real gas turbine combustors. The configuration consisted of an annular jet of high velocity carrying air and a radial injection of fuel before the exit of the bluff-body. This resulted in a reasonably well-mixed recirculation zone (CRZ), where the mixture is slightly richer in fuel than stoichiometry, surrounded by a mixing layer.

Simulations of the inert flow revealed that the mixture fraction field was more sensitive to the resolution of the mesh than the velocity field. Good agreement with experimental data for the velocity was achieved even using a relatively coarse mesh, but in order to capture the mixture fraction field correctly, a mesh that was almost six times finer had to be used.

Overall, the results from the simulations were found to agree reasonably well with the experimental findings, at least at a qualitative level. It was difficult to make quantitative comparison with the experimental results, because there were not many quantities measured and most of the comparison was made based on fast camera and OH-PLIF images. Nevertheless, it was possible to draw conclusions about the flame expansion process based on the experimental data that were available.

The location of the spark affected the expansion pattern and the time required

for the flame to stabilise. Positioning the spark in the mixing layer resulted in faster expansion compared to a spark in the recirculation zone. This was due to the fact that in the mixing layer, the mixture that was 'sampled' by the spark was closer to stoichiometry and the higher axial velocity caused a fast flame expansion. When the spark was located in the recirculation zone, a significant amount of time was spent heating the CRZ, and only later did the flame expand. During flame expansion (independent of the spark location), the OH field appeared to be very 'patchy', as observed in the experiment [11]. This was due to the fact that at different times, different regions corresponded to different levels of burning, with some locations fully burning, others being inert and others corresponding the intermediate conditions. The size of the spark also played a vital role. If the spark was very small, the rapid diffusion and convection of heat and species caused extinction of the flame.

Two chemical mechanisms of different complexity were used in these simulations. Both the global single-step mechanism and a detailed 16-species mechanism reproduced the pattern of the flame expansion reasonably well, but the rate of expansion was over-predicted by the single-step mechanism by a factor of two, whereas the detailed chemical mechanism resulted in better predictions.

The stabilisation mechanism of the flame was also investigated. Transport of heat and species from the hot recirculation zone to the fresh unreacted gases that constantly enter the burner, resulted to what can be interpreted as a lift-off hight where the transition from cold unreacted to hot reacting gases is made.

6.3 Suggestions for future work

This thesis has shown some of the capabilities and limitations of first-order CMC, when applied to ignition problems. In cases where the flame expansion is due to convection, either in terms of mean velocity or resolved fluctuations (for example chapter 4) and/or volumetric expansion, recirculation and turbulence (for example chapter 5) it appears that the CMC/LES combination produces good predictions.

However, in diffusion-dominated cases, such as the upstream flame propagation in chapter 4, some problems were encountered. Further research must be undertaken in the modelling of the sub-grid scale conditional flux, but also in the sub-models themselves (for example the conditional diffusivity) if the gradient model is used.

The models used for the conditional scalar dissipation rate must also be further investigated and validated. In principle, flame extinction is caused by high scalar dissipation rate and hence, the CMC should be able to capture such phenomena. It has been seen, however, in chapter 4 that there have been problems of flame anchoring at the spark location. This is partly due to the fact that the flamelets that were in the spark location initially could not be extinguished and this may be related to the model for the conditional scalar dissipation rate.

The models for the conditional velocity must also be validated further. Knowledge from CMC/RANS calculations is being used at the moment and the accuracy of these models in an LES context has not been validated yet. LES offer amazing capabilities and by refining the sub-models in the CMC, it is possible to have a model that could be used for a variety of transient combustion phenomena.

The use of higher order CMC should also be investigated. For flames close to extinction, it is possible that first-order closure is inadequate. In any case, the feasibility of using second-order closure in LES (bearing in mind the increase in the size of the system and hence in computational time that would have to be solved) should be examined.

The long term goal of this study is to use a CMC/LES approach in real gas turbine combustors. This poses many questions and many challenges to overcome. The introduction of spray atomisation and evaporation and the way this would appear in the CMC equations is still a subject of research [132, 133]. Furthermore, the combustion of the fuels used in real combustors are described by more complicated chemical mechanisms than the ones presented in this thesis. The increase of the number of ODEs that must be solved and therefore of the computational cost of an LES/CMC calculation puts pressure for creating more effective and less time-

consuming computer codes. There are therefore challenges both in terms of theory and modelling, but also in terms of code development and efficiency.

Appendix A

Calculation of variance-2

The resolved mixture fraction and its sub-grid scale variance are defined:

$$\widetilde{\xi} = \int_0^1 \xi \, \widetilde{\mathcal{P}}(\eta) \, d\eta \tag{A.1}$$

$$\widetilde{\xi''^2} = \int_0^1 (\xi - \widetilde{\xi})^2 \, \widetilde{\mathcal{P}}(\eta) \, d\eta \tag{A.2}$$

where ξ is the mixture fraction and $\widetilde{\mathcal{P}}(\eta)$ is the Filtered Density Function. One of the properties of the FDF is that:

$$\int_0^1 \widetilde{\mathcal{P}}(\eta) \, d\eta = 1 \tag{A.3}$$

Expanding (A.2) we obtain:

$$\begin{aligned} \widetilde{\xi''^2} = \int_0^1 (\xi^2 - 2\xi\widetilde{\xi} + \widetilde{\xi}^2) \, \widetilde{\mathcal{P}}(\eta) \, d\eta = \int_0^1 \xi^2 \, \widetilde{\mathcal{P}}(\eta) \, d\eta - 2\widetilde{\xi} \int_0^1 \xi \, \widetilde{\mathcal{P}}(\eta) \, d\eta + \\ \widetilde{\xi}^2 \int_0^1 \widetilde{\mathcal{P}}(\eta) \, d\eta = \int_0^1 \xi^2 \, \widetilde{\mathcal{P}}(\eta) \, d\eta - 2\widetilde{\xi}^2 + \widetilde{\xi}^2 \Rightarrow \widetilde{\xi''^2} = \int_0^1 \xi^2 \, \widetilde{\mathcal{P}}(\eta) \, d\eta - \widetilde{\xi}^2 \end{aligned} \tag{A.4}$$

The integrated mixture fraction and its variance can be defined:

$$\widetilde{\xi}^* = \int_0^1 \xi \, \widetilde{\mathcal{P}}^*(\eta) \, d\eta \tag{A.5}$$

$$\widetilde{\xi''^2}^*_2 = \int_0^1 (\xi - \widetilde{\xi}^*)^2 \, \widetilde{\mathcal{P}}^*(\eta) \, d\eta \tag{A.6}$$

where $\widetilde{\mathcal{P}}^*(\eta)$ is the integrated FDF. Following the same procedure as before, (A.6) can be expanded:

$$\widetilde{\xi''^2}^*_2 = \int_0^1 (\xi^2 - 2\xi\widetilde{\xi}^* + \widetilde{\xi}^{*2})\,\widetilde{\mathcal{P}}^*(\eta)\,d\eta = \int_0^1 \xi^2\,\widetilde{\mathcal{P}}^*(\eta)\,d\eta - 2\widetilde{\xi}^* \int_0^1 \xi\,\widetilde{\mathcal{P}}^*(\eta)\,d\eta +$$
$$\widetilde{\xi}^2 \int_0^1 \widetilde{\mathcal{P}}^*(\eta)\,d\eta = \int_0^1 \xi^2\,\widetilde{\mathcal{P}}^*(\eta)\,d\eta - 2\widetilde{\xi}^{*2} + \widetilde{\xi}^{*2} \Rightarrow \widetilde{\xi''^2}^* = \int_0^1 \xi^2\,\widetilde{\mathcal{P}}^*(\eta)\,d\eta - \widetilde{\xi}^{*2} \tag{A.7}$$

The integrated FDF, mixture fraction and square of mixture fraction are defined as

$$\widetilde{\mathcal{P}}^*(\eta) = \frac{\int_V \overline{\rho}\widetilde{\mathcal{P}}(\eta)\,dV'}{\int_V \overline{\rho}\,dV'} \tag{A.8}$$

$$\widetilde{\xi}^* = \frac{\int_V \overline{\rho}\widetilde{\xi}\,dV'}{\int_V \overline{\rho}\,dV'} \tag{A.9}$$

$$\widetilde{\xi}^{2*} = \frac{\int_V \overline{\rho}\widetilde{\xi}^{\,2}\,dV'}{\int_V \overline{\rho}\,dV'} \tag{A.10}$$

Using (2.52), (A.4), (A.8) and (A.10), (A.7) will become:

$$\widetilde{\xi''^2}^*_2 = \int_0^1 \xi^2 \left[\frac{\int_V \overline{\rho}\widetilde{\mathcal{P}}(\eta)\,dV'}{\int_V \overline{\rho}\,dV'}\right] d\eta - \left(\frac{\int_V \overline{\rho}\widetilde{\xi}\,dV'}{\int_V \overline{\rho}\,dV'}\right)^2 = \frac{1}{\int_V \overline{\rho}\,dV'} \int_V \overline{\rho}\left[\int_0^1 \xi^2\,\widetilde{\mathcal{P}}(\eta)\,d\eta\right] dV' -$$
$$\left(\frac{\int_V \overline{\rho}\widetilde{\xi}\,dV'}{\int_V \overline{\rho}\,dV'}\right)^2 = \frac{1}{\int_V \overline{\rho}\,dV'} \int_V \overline{\rho}(\widetilde{\xi''^2} + \widetilde{\xi}^2)\,dV' - \left(\frac{\int_V \overline{\rho}\widetilde{\xi}\,dV'}{\int_V \overline{\rho}\,dV'}\right)^2 = \widetilde{\xi}^{\,2*} + \widetilde{\xi''^2}^* - \widetilde{\xi}^{*2} \tag{A.11}$$

Appendix B

Upwind and TVD discretisation schemes for the convection term in the CMC equation

The equation that is discussed in this section is the one dimensional inviscid flow equation for a scalar f:

$$\frac{\partial f}{\partial t} + u\frac{\partial f}{\partial x} = 0 \tag{B.1}$$

where u is the velocity (assumed here to be positive) in the x direction. The x direction is discretised and the variable f is considered to have the shape shown in Fig. B.1.

The first order accuracy upwind scheme used in this thesis, will be:

$$\frac{\partial f_i}{\partial t} = -\frac{u_i}{\Delta x}(f_i - f_{i-1}) \tag{B.2}$$

For a uniform grid of spacing Δx, the TVD scheme considered here would [112, 113] be:

$$\begin{aligned}\frac{\partial f_i}{\partial t} = &-\frac{1}{\Delta x}\left[1 + \frac{1}{2}\Psi(r^+_{1-\frac{1}{2}}) - \frac{1}{2}\frac{\Psi(r^+_{1-\frac{3}{2}})}{r^+_{1-\frac{3}{2}}}\right] u^+_{1-\frac{1}{2}}(f_i - f_{i-1}) \\ &-\frac{1}{\Delta x}\left[1 + \frac{1}{2}\Psi(r^-_{1+\frac{1}{2}}) - \frac{1}{2}\frac{\Psi(r^-_{1+\frac{3}{2}})}{r^-_{1+\frac{3}{2}}}\right] u^-_{1+\frac{1}{2}}(f_{i+1} - f_i)\end{aligned} \tag{B.3}$$

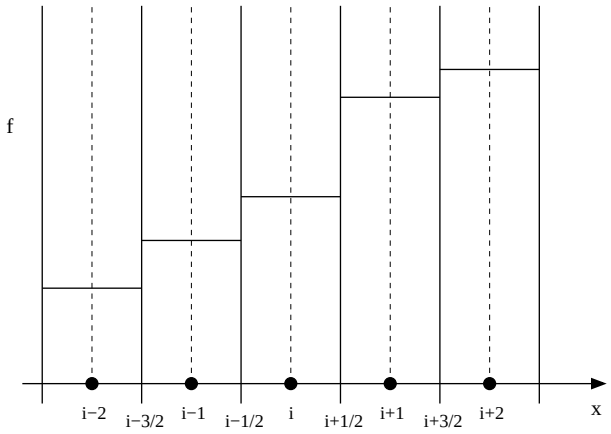

Figure B.1: Discretisation of x direction and profile of scalar f.

where

$$r^{+}_{1-\frac{1}{2}} = \frac{f_{i+1} - f_i}{f_i - f_{i-1}} \tag{B.4}$$

$$r^{+}_{1-\frac{3}{2}} = \frac{f_i - f_{i-1}}{f_{i-1} - f_{i-2}} \tag{B.5}$$

$$r^{-}_{1+\frac{1}{2}} = \frac{f_{i-1} - f_{i-2}}{f_i - f_{i-1}} \tag{B.6}$$

$$r^{-}_{1+\frac{3}{2}} = \frac{f_{i+1} - f_i}{f_{i+2} - f_{i+1}} \tag{B.7}$$

$$\tag{B.8}$$

and Ψ is Van Leer's limiter:

$$\Psi(r) = \frac{r + |r|}{1 + r} \qquad . \tag{B.9}$$

Appendix C

Derivation of the transport equation for the sub-grid scale variance

The transport equation for $\widetilde{\xi^2}$ is:

$$\frac{\partial \overline{\rho}\widetilde{\xi^2}}{\partial t} + \frac{\partial \overline{\rho}\widetilde{u}_i\widetilde{\xi^2}}{\partial x_i} = \frac{\partial}{\partial x_i}\left(\overline{\rho}(D + D_t)\frac{\partial \widetilde{\xi^2}}{\partial x_i}\right) - 2\overline{\rho}\widetilde{N} \tag{C.1}$$

where

$$\widetilde{N} = D\widetilde{\left(\frac{\partial \xi}{\partial x_i}\right)^2} \tag{C.2}$$

The transport equation for the resolved mixture fraction $\widetilde{\xi}$ is:

$$\frac{\partial \overline{\rho}\widetilde{\xi}}{\partial t} + \frac{\partial \overline{\rho}\widetilde{u}_i\widetilde{\xi}}{\partial x_i} = \frac{\partial}{\partial x_i}\left(\overline{\rho}(D + D_t)\frac{\partial \widetilde{\xi}}{\partial x_i}\right) \tag{C.3}$$

Multiply Eq. (C.3) by $\widetilde{\xi}$:

$$\widetilde{\xi}\frac{\partial \overline{\rho}\widetilde{\xi}}{\partial t} + \widetilde{\xi}\frac{\partial \overline{\rho}\widetilde{u}_i\widetilde{\xi}}{\partial x_i} = \widetilde{\xi}\frac{\partial}{\partial x_i}\left(\overline{\rho}(D + D_t)\frac{\partial \widetilde{\xi}}{\partial x_i}\right) \tag{C.4}$$

If $\widetilde{\sigma} = \widetilde{\xi^2}$ then:

$$\widetilde{\xi}\frac{\partial\overline{\rho}\widetilde{\xi}}{\partial t} = \frac{1}{2}\frac{\partial\overline{\rho}\widetilde{\sigma}}{\partial t} \tag{C.5}$$

$$\widetilde{\xi}\frac{\partial\overline{\rho}\widetilde{u}_i\widetilde{\xi}}{\partial x_i} = \frac{1}{2}\frac{\partial\overline{\rho}\widetilde{u}_i\widetilde{\sigma}}{\partial x_i} \tag{C.6}$$

$$\widetilde{\xi}\frac{\partial}{\partial x_i}\left(\overline{\rho}(D+D_t)\frac{\partial\widetilde{\xi}}{\partial x_i}\right) = \frac{1}{2}\frac{\partial}{\partial x_i}\left(\overline{\rho}(D+D_t)\frac{\partial\widetilde{\sigma}}{\partial x_i}\right) - \overline{\rho}(D+D_t)\left(\frac{\partial\widetilde{\xi}}{\partial x_i}\right)^2 \tag{C.7}$$

Eq. (C.4) will become:

$$\frac{\partial\overline{\rho}\widetilde{\sigma}}{\partial t} + \frac{\partial\overline{\rho}\widetilde{u}_i\widetilde{\sigma}}{\partial x_i} = \frac{\partial}{\partial x_i}\left(\overline{\rho}(D+D_t)\frac{\partial\widetilde{\sigma}}{\partial x_i}\right) - 2\overline{\rho}(D+D_t)\left(\frac{\partial\widetilde{\xi}}{\partial x_i}\right)^2 \tag{C.8}$$

Subtracting Eq. (C.8) from (C.1):

$$\begin{aligned}\frac{\partial\overline{\rho}\widetilde{\xi^2}}{\partial t} - \frac{\partial\overline{\rho}\widetilde{\sigma}}{\partial t} + \frac{\partial\overline{\rho}\widetilde{u}_i\widetilde{\xi^2}}{\partial x_i} - \frac{\partial\overline{\rho}\widetilde{u}_i\widetilde{\sigma}}{\partial x_i} &= \frac{\partial}{\partial x_i}\left(\overline{\rho}(D+D_t)\frac{\partial\widetilde{\xi^2}}{\partial x_i}\right)\\ -\frac{\partial}{\partial x_i}\left(\overline{\rho}(D+D_t)\frac{\partial\widetilde{\sigma}}{\partial x_i}\right) - 2\overline{\rho}\widetilde{N} &+ 2\overline{\rho}(D+D_t)\left(\frac{\partial\widetilde{\xi}}{\partial x_i}\right)^2\end{aligned} \tag{C.9}$$

By introducing the sub-grid scale variance $\widetilde{\xi''^2} = \widetilde{\xi^2} - \widetilde{\sigma}$, Eq. (C.9) becomes:

$$\frac{\partial\overline{\rho}\widetilde{\xi''^2}}{\partial t} + \frac{\partial\overline{\rho}\widetilde{u}_i\widetilde{\xi''^2}}{\partial x_i} = \frac{\partial}{\partial x_i}\left(\overline{\rho}(D+D_t)\frac{\partial\widetilde{\xi''^2}}{\partial x_i}\right) - 2\overline{\rho}\widetilde{N} + 2\overline{\rho}(D+D_t)\left(\frac{\partial\widetilde{\xi}}{\partial x_i}\right)^2 \tag{C.10}$$

Bibliography

[1] A. Triantafyllidis, E. Mastorakos, and R. L. G. M. Eggels. Large eddy simulations of forced ignition of a non-premixed bluff-body methane flame with conditional moment closure. *Combustion and Flame*, doi: 10.1016/j.combustflame.2009.05.005, 2009.

[2] A. Triantafyllidis and E. Mastorakos. Implementation issues of the conditional moment closure model in large eddy simulations. *Flow, Turbulence and Combustion*, doi: 10.1007/s10494-009-9226-y, 2009.

[3] A. Triantafyllidis, E. Mastorakos, and R. L. G. M. Eggels. LES/CMC of forced ignition of a bluff-body stabilised non-premixed methane flame. *Direct and Large Eddy Simulations 7*, Trieste, Italy, September 2008.

[4] I. Stankovic, A. Triantafyllidis, and B. Merci. Analysis of non-premixed auto-ignition of heated hydrogen/air mixtures with different detailed mechanisms. *Mathematics in Chemical Kinetics and Engineering*, Gent, Belgium, February 2009.

[5] I. Stankovic, A. Triantafyllidis, E. Mastorakos, and B. Merci. Simulations of hydrogen auto-ignition in a turbulent co-flow of heated air with LES and CMC approach. *Submitted to Flow, Turbulence and Combustion.*

[6] S. Ayache, J. Dawson, A. Triantafyllidis, R. Balachadran, and E. Mas-

torakos. Experiments and large-eddy simulations of acoustically-forced bluff-body flows. *Submitted to International Journal of Heat and Fluid FLow*.

[7] E. Fernández-Tarrazo, A. L. Sánchez, A. Linãn, and F. A. Williams. A simple one-step chemistry model for partially premixed hydrocarbon combustion. *Combustion and Flame*, 147:32–38, 2006.

[8] M. D. Smooke and V. Giovangigli. Reduced kinetic mechanisms and asymptotic approximations for methane-air flames. In M. D. Smooke, editor, *Lecture Notes in Physics*. Springer-Verlag, 1991.

[9] G. P. Smith, D. M. Golden, M. Frenklach, N. W Moriarty, B. Eiteneer, M. Goldenberg, C. T Bowman, R. K. Hanson, S. Song, W. C. Gardiner Jr., V. V. Lissianski, and Z. Qin. Gri-mech 3.0 web-site http://www.me.berkeley.edu/gri_mech/.

[10] S. F. Ahmed, I. A. Bahena Ledezma, and E. Mastorakos. Spark ignition in a turbulent shearless fuel-air mixing layer: Average flame growth rates. *Submitted to AIAA Journal*, 2009.

[11] S. F. Ahmed, R. Balachandran, T. Marchione, and E. Mastorakos. Spark ignition of turbulent nonpremixed bluff-body flames. *Combustion and Flame*, 151:366–385, 2007.

[12] S. F. Ahmed. *Spark Ignition of Turbulent Non-Premixed Flames*. PhD thesis, University of Cambridge, 2006.

[13] E. Mastorakos. Ignition of turbulent non-premixed flames. *Progress in Energy and Combustion Science*, 35:57–97, 2009.

[14] I. Glassman. *Combustion*. Academic Press, 3rd edition, 1996.

[15] P. D. Ronney. Laser versus conventional ignition of flames. *Optical Engineering*, 33:510–521, 1994.

[16] J. E. Orrin, I. M. Vince, and F. J. Weinberg. A study of plasma jet ignition mechanisms. *Proceedings of the Combustion institute*, 18:1755–1765, 1981.

[17] E. Murase, S. Ono, K. Hanada, and A. K. Oppenheim. Initiation of combustion in lean mixtures by flame jets. *Combustion Science and Technology*, 113:167–177, 1996.

[18] E. S. Richardson and E. Mastorakos. Numerical investigation of forced ignition in laminar counterflow non-premixed methane-air flames. *Combustion Science and Technology*, 179:21–37, 2007.

[19] M. T. E. Smith, A. D. Birch, D. R. Brown, and M. Fairweather. Studies of ignition and flame propagation in turbulent jets of natural gas, propane and a gas with a high hydrogen content. *Proceedings of the Combustion Institute*, 21:1403–1408, 1986.

[20] A. D. Birch, D. R. Brown, M. G. Dodson, and J. R. Thomas. Studies of flammability in turbulent flows using Raman spectroscopy. *Proceedings of the Combustion institute*, 17:307–314, 1978.

[21] A. D. Birch, D. R. Brown, and M. G. Dodson. Ignition probabilities in turbulent mixing flows. *Proceedings of the Combustion institute*, 18:1775–1780, 1981.

[22] S. F. Ahmed and E. Mastorakos. Spark ignition of turbulent jet flames. *Combustion and Flame*, 146:215–231, 2006.

[23] S. F. Ahmed, R. Balachadran, and E. Mastorakos. Measurements of ignition probability in turbulent non-premixed counterflow flames. *Proceedings of the Combustion Institute*, 31:1507–1513, 2007.

[24] M. Chen, M. Herrmann, and N. Peters. Flamelet modelling of lifted turbulent methane/air and propane/air jet diffusion flames. *Proceedings of the Combustion institute*, 28:167–174, 2000.

[25] G. Lacaze, E. Richardson, and T. Poinsot. Large Eddy Simulation of spark ignition in a turbulent methane jet. *Submitted to Combustion and Flame*, 2009.

[26] V. Subramanian, P. Domingo, and L. Vervisch. Large eddy simulations of forced ignition of an annular bluff-body burner. *DNS and LES of ignition*, Czestochowa, Poland, November 2008.

[27] M. Boileau, G. Staffelbach, B. Cuenot, T. Poinsot, and C. Bérat. LES of an ignition sequence in a gas turbine engine. *Combustion and Flame*, 154:2–22, 2008.

[28] S.B. Pope. *Turbulent Flows*. Cambridge University Press, 2000.

[29] H. Pitsch. Large-eddy simulation of turbulent combustion. *Annual Review of Fluid Mechanics*, 38:453–482, 2006.

[30] U. Piomelli. Large-eddy simulation: achievements and challenges. *Progress in Aerospace Sciences*, 35:335–362, 1999.

[31] T. Poinsot and D. Veynante. *Theoretical and Numerical Combustion*. Edwards, 2001.

[32] S. B. Pope. Ten questions concerning the large-eddy simulation of turbulent flows. *New Journal of Physics*, 6:35, 2004.

[33] N. Peters. *Turbulent Combustion*. Cambridge University Press, 2000.

[34] R. W. Bilger. Turbulent flows with nonpremixed reactants. In P.A. Libby and F.A. Williams, editors, *Turbulent Reacting Flows*. Springer-Verlag, 1980.

[35] S. R. Turns. *An Introduction to Combustion*. McGraw Hill, 2nd edition, 2000.

[36] N. Branley and W. P. Jones. Large eddy simulation of a turbulent non-premixed flame. *Combustion and Flame*, 127:1914–1934, 2001.

[37] N. Peters. Laminar diffusion flamelet models in non-premixed turbulent combustion. *Progress in Energy and Combustion Science*, 10:319–339, 1984.

[38] A. W. Cook, J. J. Riley, and G. Kosály. A laminar flamelet approach to subgrid-scale chemistry in turbulent flows. *Combustion and Flame*, 109:332–341, 1997.

[39] A. Kempf, A. Sadiki, and J. Janicka. Prediction of finite chemistry effects using large eddy simulation. *Proccedings of the Combustion Institute*, 29:1979–1985, 2002.

[40] A. Kempf, R. P. Lindstedt, and J. Janicka. Large-eddy simulation of a bluff-body stabilized nonpremixed flame. *Combustion and Flame*, 144:170–189, 2006.

[41] H. Pitsch and H. Steiner. Large-eddy simulation of a turbulent piloted methane/air diffusion flame (Sandia flame D). *Physics of Fluids*, 12:2541–2554, 2000.

[42] C. D. Pierce and P. Moin. Progress-variable approach for large eddy simulation of non-premixed turbulent combustion. *Journal of Fluid Mechanics*, 504:73–97, 2004.

[43] M. Ihme and H. Pitsch. Prediction of extinction and reignition in nonpremixed turbulent flames using a flamelet/progress variable model 2. Application in LES of Sandia flames D and E. *Combustion and Flame*, 155:90–107, 2008.

[44] A. Y. Klimenko and R. W. Bilger. Conditional moment closure for turbulent combustion. *Progress in Energy and Combustion Science*, 25:595–687, 1999.

[45] S. Navarro-Martinez, A. Kronenburg, and F. Di Mare. Conditional moment closure for large eddy simulations. *Flow, Turbulence and Combustion*, 75:245–274, 2005.

[46] Y. M. Wright, G. De Paola, K. Boulouchos, and E. Mastorakos. Simulations of spray autoignition and flame establishment with two-dimensional CMC. *Combustion and Flame*, 143:402–419, 2005.

[47] S. H. Kim and K. Y. Huh. Numerical simulation of spray autoignition by the first-order conditional moment closure model. *Proceedings of the Combustion Institute*, 29:569–576, 2002.

[48] G. De Paola, E. Mastorakos, Y. M. Wright, and K. Boulouchos. Diesel engine simulations with multi-dimensional conditional moment closure. *Combustion Science and Technology*, 180:883–899, 2008.

[49] M. R. Roomina and R. W. Bilger. Conditional moment closure (CMC) predictions of a turbulent methane-air jet flame. *Combustion and Flame*, 125:1176–1195, 2001.

[50] M. Fairweather and R. M. Woolley. First-order conditional moment closure modeling of turbulent, nonpremixed hydrogen flames. *Combustion and Flame*, 133:393–405, 2003.

[51] M. Fairweather and R. M. Woolley. First-order conditional moment closure modeling of turbulent, nonpremixed methane flames. *Combustion and Flame*, 138:3–19, 2004.

[52] M. Fairweather and R. M. Woolley. First- and second-order elliptic conditional moment closure calculations of piloted methane diffusion flames. *Combustion and Flame*, 150:92–107, 2007.

[53] C. B. Devaud and K. N. C. Bray. Assessment of the applicability of conditional moment closure to a lifted turbulent flame: first order model. *Combustion and Flame*, 132:102–114, 2003.

[54] I. S. Kim and E. Mastorakos. Simulations of turbulent lifted jet flames with two-dimensional conditional moment closure. *Proceedings of the Combustion Institute*, 30:911–918, 2005.

[55] S. H. Kim, K. Y. Huh, and L. Tao. Application of the elliptic conditional moment closure model to a two-dimensional nonpremixed methanol bluff-body flame. *Combustion and Flame*, 120:75–90, 2000.

[56] I. S. Kim and E. Mastorakos. Simulations of turbulent non-premixed counterflow flames with first-order conditional moment closure. *Flow, Turbulence and Combustion*, 76:133–162, 2006.

[57] Yunardi, R. M. Woolley, and M. Fairweather. Conditional moment closure prediction of soot formation in turbulent, nonpremixed ethylene flames. *Combustion and Flame*, 152:360–376, 2008.

[58] R. M. Woolley, M. Fairweather, and Yunardi. Conditional moment closure modelling of soot formation in turbulent, non-premixed methane and propane flames. *Fuel*, 88:393–407, 2009.

[59] S. H. Kim and H. Pitsch. Conditional filtering method for large-eddy simulation of turbulent nonpremixed combustion. *Physics of Fluids*, 17:105103, 2005.

[60] S. Navarro-Martinez and A. Kronenburg. LES-CMC simulations of a turbulent bluff-body flame. *Proceedings of the Combustion Institute*, 31:1721–1728, 2007.

[61] S. Navarro-Martinez and A. Kronenburg. LES-CMC simulations of a lifted methane flame. *Proceedings of the Combustion Institute*, 32:1509–1516, 2009.

[62] H. Pitsch. Improved pollutant predictions in large-eddy simulations of turbulent non-premixed combustion by considering scalar dissipation rate fluctuations. *Proceedings of the Combustion institute*, 29:1971–1978, 2002.

[63] S. H. Kim and H. Pitsch. Mixing characteristics and structure of a turbulent jet diffusion flame stabilized on a bluff-body. *Physics of Fluids*, 18:075103, 2006.

[64] S. B. Pope. PDF methods for turbulent reacting flows. *Progress in Energy and Combustion Science*, 11:119–192, 1985.

[65] J. Xu and S. B. Pope. PDF calculations of turbulent nonpremixed flames with local extinction. *Combustion and Flame*, 123:281–307, 2000.

[66] V. Saxena and S. B. Pope. PDF calculations of major and minor species in a turbulent piloted jet flame. *Proceedings of the Combustion Institute*, 27:1081–1086, 1998.

[67] J. Y. Chen, W. Kollmann, and R. W. Dibble. PDF modelling of turbulent methane-air nonpremixed jet flames. *Combustion Science and Technology*, 64:315–346, 1989.

[68] T. Hůlek and R. P. Lindstedt. Computations of steady-state and transient premixed turbulent flames usind pdf methods. *Combustion and Flame*, 104:481–504, 1996.

[69] W. P. Jones and M. Kakhi. PDF modelling of finite-rate chemistry effects in turbulent nonpremixed jet flames. *Combustion and Flame*, 115:210–229, 1998.

[70] R. R. Cao, S. B. Pope, and A. R. Masri. Turbulent lifted flames in a vitiated coflow investigated using joint PDF calculations. *Combustion and Flame*, 142:438–453, 2005.

[71] Y. Z. Zhang, E. H. Kung, and D. C. Haworth. A PDF method for multidimensional modeling of HCCI engine combustion: effects of turbulence/chemistry interactions on ignition timing and emissions. *Proceedings of the Combustion Institute*, 30:2763–2771, 2005.

[72] D. Geyer, A. Dreizler, J. Janicka, A. D. Permana, and J. Y. Chen. Finite-rate chemistry effects in turbulent opposed flows: comparison of Raman/Rayleigh measurements and Monte Carlo PDF simulations. *Proceedings of the Combustion Institute*, 30:711–718, 2005.

[73] F. Gao and E. E. O'Brien. A large-eddy simulation scheme for turbulent reacting flows. *Physics of Fluids*, A 5 (6):1282–1284, 1993.

[74] R. J. Colucci, F. A. Jaberi, P. Givi, and S. B. Pope. Filtered density function for large eddy simulation of turbulent reacting flows. *Physics of Fluids*, 10:499–515, 1998.

[75] M. R. H. Sheikhi, T. G. Drozda, P. Givi, and S. B. Pope. Velocity-scalar filtered density function for large eddy simulation of turbulent flows. *Physics of Fluids*, 15 (8):2321–2337, 2003.

[76] M. Muradoglu, K. Liu, and S. B. Pope. PDF modeling of a bluff-body stabilized turbulent flame. *Combustion and Flame*, 132:115–137, 2003.

[77] W. P. Jones and S. Navarro-Martinez. Large eddy simulation of autoignition with a subgrid probability density function method. *Combustion and Flame*, 150:170–187, 2007.

[78] W. P. Jones, S. Navarro-Martinez, and O. Röhl. Large eddy simulation of hydrogen auto-ignition with a probability density function. *Proceedings of the Combustion Institute*, 31:1765–1771, 2007.

[79] L. Y. M. Gicquel, G. Staffelbach, B. Cuenot, and T. Poinsot. Large eddy simulations of turbulent reacting flows in real burners: The status and the challenges. *Journal of Physics: Conference Series*, 125:012029, 2008.

[80] G. Boudier, L. Y. M. Gicquel, T. Poinsot, Bissières, and C. Bérat. Comparison of LES, RANS and experiments in an aeronautical gas turbine combustion chamber. *Proceedings of the Combustion Institute*, 31:3075–3082, 2007.

[81] F. Di Mare, W. P. Jones, and K. R. Menzies. Large eddy simulation of a model gas turbine combustor. *Combustion and Flame*, 137:278–294, 2004.

[82] P. Moin and S. V. Apte. Large-eddy simulation of realistic gas turbine combustors. *AIAA Journal*, 44 (4):698–708, 2006.

[83] G. Lacaze, B. Cuenot, T. Poinsot, and M. Oschwald. Large eddy simulation of laser ignition and compressible reacting flow in a rocket-like configuration. *Combustion and Flame*, 156:1166–1180, 2009.

[84] M. Germano, U. Piomelli, P. Moin, and W.H. Cabot. A dynamic subgrid-scale eddy viscosity model. *Physics of Fluids*, 3:1760–1765, 1991.

[85] H. Pitsch and H. Steiner. Scalar mixing and dissipation rate in large-eddy simulations of non-premixed turbulent combustion. *Proceedings of the Combustion Institute*, 28:41–49, 2000.

[86] A Kempf, H. Forkel, J.-Y. Chen, A. Sadiki, and J. Janicka. Large-eddy simulation of counterflow configuration with and without combustion. *Proceedings of the Combustion Institute*, 28:35–40, 2000.

[87] C. D. Pierce and P. Moin. A dynamic model for subgrid-scale variance and dissipation rate of a conserved scalar. *Physics of Fluids*, 10:3041–3044, 1998.

[88] M. Dianat, Z. Yang, and J.J. McGuirk. Large eddy simulation of scalar mixing in a coaxial confined jet. *Flow, Turbulence and Combustion*, 77:205–227, 2006.

[89] A. W. Cook and J. J. Riley. A subgrid model for equilibrium chemistry in turbulent flows. *Physics of Fluids*, 6:2868–2870, 1994.

[90] C. Pera, J. Réveillon, L. Vervisch, and P. Domingo. Modeling subgrid scale mixture fraction variance in LES of evaporating spray. *Combustion and Flame*, 146:635–648, 2006.

[91] S.S. Girimaji and Y. Zhou. Analysis and modeling of subgrid scalar mixing using numerical data. *Physics of Fluids*, 8:1224–1236, 1996.

[92] C. Jiménez, F. Ducros, B. Cuenot, and B. Bédat. Subgrid scale variance and dissipation of a scalar field in large eddy simulations. *Physics of Fluids*, 13:1748–1754, 2001.

[93] E. E. O'Brien. The probability density function (PDF) approach to reacting turbulent flows. In P.A. Libby and F.A Williams, editors, *Turbulent Reacting Flows*. Springer-Verlag, 1980.

[94] A. R. Masri, R. W. Dibble, and R. S. Barlow. The structure of turbulent nonpremixed flames of methanol over a range of mixing rates. *Combustion and Flame*, 89:167–185, 1992.

[95] M. Fairweather and R. M. Woolley. Conditional moment closure calculations of a swirl-stabilized, turbulent nonpremixed methane flame. *Combustion and Flame*, 151:397–411, 2007.

[96] S. H. Kim and K. Y. Huh. Second-order conditional moment closure modeling of turbulent piloted jet diffusion flames. *Combustion and Flame*, 138:336–352, 2004.

[97] A. Kronenburg, R. W. Bilger, and J. H. Kent. Second-order conditional moment closure for turbulent jet-diffusion flames. *Proceedings of the Combustion Institute*, 27:1097–1104, 1998.

[98] E. E. O'Brien and T.-L. Jiang. The conditional dissipation rate of an initially binary scalar in homogeneous turbulence. *Physics of Fluids*, 3:3121–3123, 1991.

[99] A. Y. Klimenko. Note of the conditional moment closure in turbulent shear flows. *Physics of Fluids*, 7:446–448, 1995.

[100] C. N. Markides and E. Mastorakos. Measurements of scalar dissipation in a turbulent plume with planar laser-induced fluorescence of acetone. *Chemical Engineering Science*, 61:2835–2842, 2006.

[101] C. N. Markides and E. Mastorakos. Measurements of the statistical distribution of the scalar dissipation rate in turbulent axisymmetric plumes. *Flow, Turbulence and Combustion*, 81:221–234, 2008.

[102] C. N. Markides and E. Mastorakos. An experimental study of hydrogen autoignition in a turbulent co-flow of heated air. *Proceedings of the Combustion Institute*, 30:883–891, 2005.

[103] R. W. Bilger. Some aspects of scalar dissipation. *Flow, Turbulence and Combustion*, 72:93–114, 2004.

[104] C. Wall, B. J. Boersma, and P. Moin. An evaluation of the assumed beta probability density function subgrid-scale model for large eddy simulation of nonpremixed, turbulent combustion with heat release. *Physics of Fluids*, 12:2522–2529, 2000.

[105] S. V. Patankar. *Numerical Heat Transfer and Fluid Flow*. Hemisphere, 1st edition, 1980.

[106] S. James, J. Zhu, and M. S. Anand. Large-eddy simulations as a design tool for gas turbine combustion systems. *AIAA Journal*, 44:674–686, 2006.

[107] S. James, J. Zhu, and M. S. Anand. Large eddy simulations of turbulent flames using the filtered density function. *Proccedings of the Combustion Institute*, 31:1737–1745, 2007.

[108] M. Klein, A. Sadiki, and J. Janicka. A digital filter based generation of inflow data for spatially developing direct numerical or large eddy simulation. *Journal of Computational Physics*, 186:652–665, 2003.

[109] S. R. Tieszen, D. W. Stamps, and T. J. O'Hern. A heuristic model of turbulent mixing applied to blowout of turbulent jet diffsuion flames. *Combustion and Flame*, 106:442–466, 1996.

[110] C. D. Richards and W. M. Pitts. Global density effects on the self-preservation behaviour of turbulent free jets. *Journal of Fluid Mechanics*, 254:417–435, 1993.

[111] C. N. Markides, G. De Paola, and E. Mastorakos. Measurements and simulations of mixing and autoignition of an n-heptane plume in a turbulent flow of heated air. *Experimental Thermal and Fluid Science*, 31:393–401, 2007.

[112] B. Van Leer. Towards the ultimate conservative difference scheme II. Monotonicity and conservation combined in a second order scheme. *Journal of Computational Physics*, 14:361–370, 1974.

[113] T. J. Chung. *Computational Fluid Dynamics*. Cambridge University Press, 2002.

[114] W. P. Jones. Turbulence modelling and numerical solution methods for variable density and combusting flows. In P.A. Libby and F.A. Williams, editors, *Turbulent Reacting Flows*. Academic Press, 1994.

[115] P. N. Brown, G. D. Byrne, and A. C. Hindmarsh. VODE, a variable-coefficient ODE solver. *SIAM Journal on Scientific and Statistical Computing*, 10:1038–1051, 1989.

[116] P. N. Brown and A. C. Hindmarsh. Reduced storage matrix methods in stiff ODE systems. *Journal of Computational and Applied Mathematics*, 31:40–91, 1989.

[117] G. D. Byrne. Pragmatic experiments with Krylov methods in the stiff ODE setting. In J Cash and I. Gladwell, editors, *Computational Ordinary Differential Equations*. Oxford University Press, 1992.

[118] G. De Paola. *Conditional Moment Closure for Autoignition in Turbulent Flows*. PhD thesis, Cambridge University, 2007.

[119] S. James and F. A. Jaberi. Large scale simulations of two-dimensional non-premixed methane jet flames. *Combustion and Flame*, 123:465–487, 2000.

[120] E. S. Richardson, Chakraborty N., and E. Mastorakos. Analysis of direct numerical simulations of ignition fronts in turbulent non-premixed flames in the context of conditional moment closure. *Proceedings of the Combustion Institute*, 31:1683–1690, 2007.

[121] C. Heeger, B. Böhm, S. F. Ahmed, R. Gordon, I. Boxx, W. Meier, A. Dreizler, and E. Mastorakos. Statistics of relative and absolute velocities of turbulent non-premixed edge flames following spark ignition. *Proceedings of the Combustion Institute*, 32:2957–2964, 2009.

[122] H. Hesse, N. Chakraborty, and E. Mastorakos. The effects of the Lewis number of the fuel on the displacement speed of edge flames in igniting turbulent mixing layers. *Proceedings of the Combustion Institute*, 32:1399–1407, 2009.

[123] J. C. Pan, W. J. Schmoll, and D. R. Ballal. Turbulent combustion properties behind a confined conical stabilizer. *Journal of Engineering for Gas Turbines and Power*, 114:33–38, 1992.

[124] B. B. Dally, A. R. Masri, R. S. Barlow, and G. J. Fiechtner. Instantaneous and mean compositional structure of bluff-body stabilized nonpremixed flames. *Combustion and Flame*, 114:119–148, 1998.

[125] A. M. K. P. Taylor and J. H. Whitelaw. Velocity characteristics in the turbulent near wakes of confined axisymmetric bluff-bodies. *Journal of Fluid Mechanics*, 139:391–416, 1984.

[126] T. Marchione, S. F. Ahmed, and E. Mastorakos. Ignition of turbulent swirling n-heptane spray flames using single and multiple sparks. *Combustion and Flame*, 156:166–180, 2009.

[127] B. Merci, E. Dick, J. Vierendeels, D. Roekaerts, and T. W. J. Peeters. Application of a new cubic turbulence model to piloted and bluff-body diffusion flames. *Combustion and Flame*, 126:1533–1556, 2001.

[128] V. Raman and H. Pitsch. Large-eddy simulation of a bluff-body-stabilized non-premixed flame using a recursive filter-refinement procedure. *Combustion and Flame*, 142:329–347, 2005.

[129] R. Balachandran, B.O. Ayoola, C. F. Kaminski, A. P. Dowling, and E. Mastorakos. Experimental investigation of the nonlinear response of turbulent premixed flames to imposed inlet velocity oscillations. *Combustion and Flame*, 143:37–55, 2005.

[130] C. A. Armitage, R. Balachandran, E. Mastorakos, and R. S. Cant. Investigation of the nonlinear response of turbulent premixed flames to imposed inlet velocity oscillations. *Combustion and Flame*, 146:419–436, 2006.

[131] T. S. Cheng, J. A. Wehrmeyer, and R. W. Pitz. Conditional analysis of lifted hydrogen jet diffusion flame experimental data and comparison to laminar flame solutions. *Combustion and Flame*, 150:340–354, 2007.

[132] M. Mortensen and R. W. Bilger. Derivation of the conditional moment closure equations for spray combustion. *Combustion and Flame*, 156:62–72, 2009.

[133] P. Schroll. *Modelling of two-phase reactive flows with Conditional Moment Closure*. PhD thesis, Cambridge University, in preparation.